AN HIGH SPEED INTEGRATED OPTICAL FABRY-PEROT MODULATOR

by

JIA YI LIANG

THESIS submitted for the degree of DOCTOR OF PHILOSOPHY of the UNIVERSITY OF LONDON

Supervised by Prof. M. G. F. WILSON

APRIL 1992

Dept. of Electronic and Electrical Eng.
University College London
Torrington Place
London WC1E 7JE
U. K.

Abstract

This thesis describes a novel approach to high speed optical modulation in lithium niobate using an optically resonant Fabry-Perot cavity.

In this work, single mode, low optical loss, out-diffusion-free waveguides were realised by a modified titanium indiffusion into a lithium niobate substrate. The coplanar asymmetric travelling-wave electrodes were investigated and fabricated by a new technique called the "etched-lift-off" method. Multi-layer highly reflective dielectric coatings were deposited onto the waveguide ends to form an optical cavity. The behavior of the optical waveguide Fabry-Perot cavity was analysed. The sensitivity to temperature variation of the modulator was investigated as well, and this indicated the possibility of using the cavity as a temperature sensor. The theoretical simulation of the Fabry-Perot modulation at high frequency was also calculated. Finally, the integrated optical Fabry-Perot modulator was fabricated and a modulation bandwidth of at least one GHz was achieved.

TO MY FAMILY

ACKNOWLEDGEMENT

I wish to give my great gratitude to my supervisor Prof. M. G. F. Wilson for his encouragement, kindness, help and guidance to complete this project.

The initial support, idea and advice from Dr, M. M. Stallard were essential to this work.

I would like to express many thanks to the British Council and the Chinese Government for a three years long Technical Co-operation Program and financial support to this subject.

I also want to thank Mr. F. Stride for his assistance and training in Clean Room.

Finally, I would like to express my warmest thanks to my friends and colleagues Dr. D. Selviah, Mr. D. Wickramasinghe, Mr. D. John and Mr. C. Watson who give me a lot of help, advice and encouragement.

TABLE OF CONTENT

LIST OF THE SYMBOLS

Waveguide Parameters

X, Y, Z	crystal axis
n	refractive index
n_e, n_o	extraordinary, ordinary index
C, C(Y,Z)	Ti concentration
D_y, D_z	diffusion coefficient
D_0^y,D_0^z	diffusion constant
E_0^y, E_0^z	activation energy
k	Boltzman's constant
T	diffusion temperature
t	diffusion time
d_y,d_z	diffusion depth
W	width of waveguide
Δn_y, Δn_z	refractive index change
$A_{e,o}(C_o, \lambda)$	diffusion proportional coefficient
L	optical wavelength
τ	Ti thickness

Electrode Parameters

r_{ij}	electro-optic coefficient
ε_r	dielectric constant
K(k)	complete elliptic integral of the first kind
C	capacitance of the electrodes
c	light speed
Z	impedance
G	gap of electrodes

W	width of electrodes
V	driving voltage
Γ	overlap integral of electric and optical fields
E	electric field
L_E	length of electrodes
f	modulation frequency
ρ	resistivity
σ	conductivity
d	skin depth
τ	thickness of electrodes
R	reflection coefficient

Optical & Electrical Parameters

E_i	electric field
H_i	magnetic field
k	wave vector
θ_i	incidence angle
μ_i	characteristic matrix
$n_{h,l}$	high-, low-refractive index
$n_{s,o}$	substrate, air refractive index
Δg	high reflectance zone
A, B	dispersion coefficient
τ	coating thickness
λ	optical wavelength
r_i	reflectivity
t_i	transmission coefficient
α	absorption coefficient
$s_{1,2}$	scattering coefficient
δ_i	phase shift in the cavity
T	intensity transmission coefficient

D	modulation depth
$\Delta\delta$	phase halfwidth
$E_{01,02}$	mode profile of waveguide
a_0	amplitude transmission coefficient
β	propagation constant
θ_w	wedge angle
W_0	mode size mismatch coefficient
$X_{01,02}$	width of waveguide mode
Φ	phase shift
p, q, r	dispersion coefficient of lithium niobate
T	temperature
L	waveguide length
ΔT_π	halfwave temperature

Modulation Parameters

n_o	optical index
n_m	microwave index
L_E	length of electrodes
L_C	length of cavity
ω	angular frequency
$V_{O,E}$	optical, microwave velocity
$\Delta^{-,+}$	velocity mismatch coefficient
t	time
$\Phi_{for,\ back}$	forward, backward phase shift
P	phase shift factor
A_i	transit phase shift
τ	transit time
I	optical intensity
E	transit electric field
k	contrast value

CHAPTER 1 INTRODUCTION

As the data rates of fibre optic communication system increase up to the GHz range, integrated optic devices (or guided wave devices) will play more and more important roles, especially in the 1.3 - 1.6 μm range. Integrated optic components which basically employ single-mode guided wave techniques are expected to contribute to rugged, cost-effective, and batch-fabricated components such as modulators, switches, multiplexers, tunable filters, frequency shifters, polarisation controllers, signal routing, and timing devices [1].

Such functions can be realised by electro-optic waveguide components. At present, the performance of $LiNbO_3$ devices is superior to comparable semiconductor electro-optic components. The research efforts in electro-optic $LiNbO_3$ waveguide components have resulted in a high state of development with regard to technology, device performance, and fibre coupling. This may be characterised by Mach-Zehnder intensity modulators with up to 36 GHz modulation bandwidth and about 100 mW driving power [2], [3], [4], [21], 8 by 8 switch arrays [7], multi-channel wave multiplexers [8], [9], and 0.5 dB insertion loss of fibre-coupled 1.3 μm $LiNbO_3$ channel waveguides [10].

Besides the applications in tele-communications, integrated optics also has application in optical signal processing and optical sensing. At present, research on integrated optic signal processing is taking place, and the signal processors employ electro-optic, acousto-optic and fibre-optic components to perform such functions as spectral analysis of radio-frequency signals, correlation and matched filtering, code and waveform synthesis, signal delay and storage, analog-to-digital and digital-to-analog conversion [11] and optic error detecting circuit [15]. Waveguides on an

integrated optic chip have been used for sensing temperature, humidity [12], electric field [13], wavefront angle, and optical disc reflectivity [14]. In most cases , the guided-wave approach is distinguished by the ability to perform a particular function at very high analog or digital data rates, and so far, many efforts have been made to provide some perspective on competing technologies and to indicate some area where future research might prove fruitful [11].

Among all the integrated optic components, the optical modulator is the most basic device for fibre optic communication and signal processing. Currently, the Mach-Zehnder modulator plays the dominant part. It is a two-arm interferometric device consisting of two 3 dB Y-branches, two pull-push phase modulators and a travelling-wave electrode structure as shown in Fig. 1.1 [2], [3], [4]. So far, high speed modulator of 36 GHz bandwidth has been fabricated [21], however, as the limitation of bandwidth-length product on $LiNbO_3$ substrate, the wider the bandwidth, the more the driving power. As the frequency goes higher, the requirement for the driving power increases and it is, therefore, more difficult to obtain very high frequency modulation.

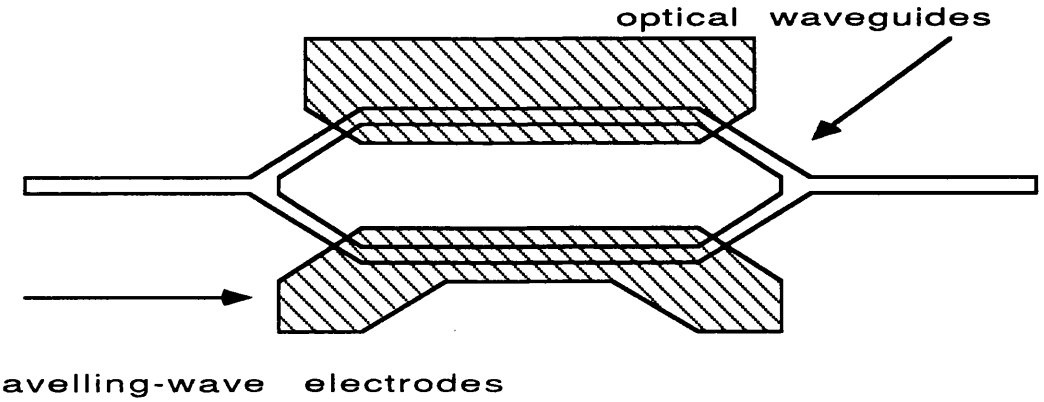

Fig. 1.1 The diagram of Mach-Zehnder integrated optical modulator

So far, much research has been done to increase the modulation

bandwidth without raising the driving power significantly, including the use of periodic and non-periodic phase reversal electrode structure [16], [17], and changing the substrate structure to match the optical and microwave velocity [18].

Another approach of optical modulation considered in this thesis allows the development of low drive power. This optically resonant modulator consists of a single straight optical waveguide, two high reflective dielectric mirrors at the ends of the waveguide to form the optical cavity and travelling electrodes as shown in Fig. 1.2, is called an integrated optical Fabry-Perot modulator. The modulator on Ti: $LiNbO_3$ waveguide has been fabricated with the driving voltage as low as 1.7 V for 84% modulation[19]. While, M. Whitehead & G. Parry [22], [23] made low-voltage Fabry-Perot modulators on multiple quantum well materials with very high on-off ratio, which is another successful demonstration of Fabry-Perot modulator.

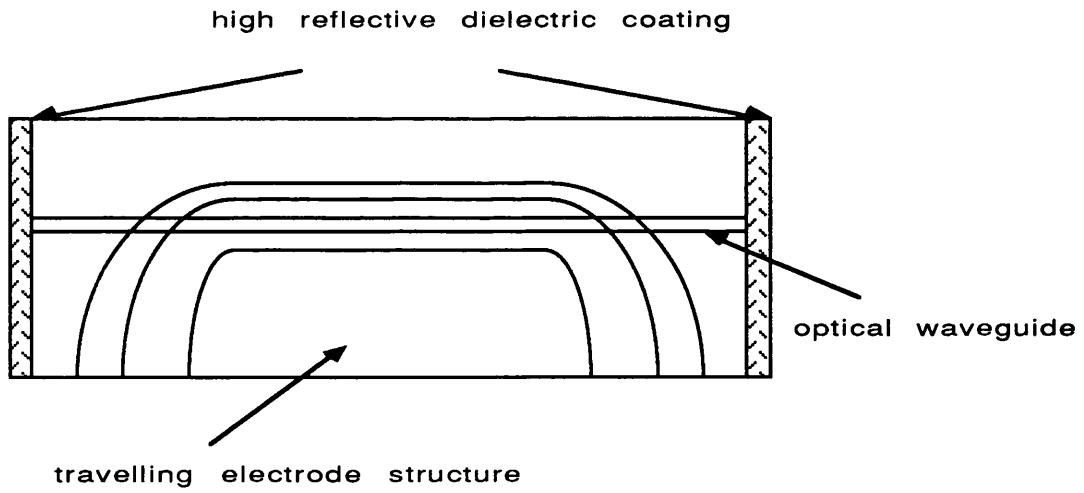

Fig. 1.2. Digram for integrated optical Fabry-Perot modulator

By comparison with the Mach-Zehnder modulator, the Fabry-Perot

modulator has a simpler structure, smaller dimensions, low driving power and possibly less optical losses. The characteristics of Fabry-Perot modulation are decided by the whole parameters of the modulator, namely, the length of the optical cavity, the length of the electrodes, the reflectivity of the mirrors at the ends of the optical waveguide, the optical loss properties of the waveguide and the position of the electrodes in optical cavity. For the Fabry-Perot modulator, the DC characteristic of the output is a Airy function, unlike Mach-Zehnder modulator which has a simple cosine-like function. In Mach-Zehnder modulation, the bandwidth of modulation is limited by the bandwidth-length product, that is, decided by the length of the electrodes, and it influenced slightly by the electrical conducting loss in the electrodes, while the driving power, or driving voltage, is decided by the length of the electrodes, the wavelength, the electrical conducting loss in the electrodes and the overlap coefficient of electrical and optical fields, which represents the dimension structure of the optical waveguide and the electrodes of the modulator on the $LiNbO_3$ substrate.

Besides being used as a modulator, the Fabry-Perot device has application in other areas. It can be used as a temperature sensor to monitor temperature change; as a scanning Fabry-Perot interferometer to analyse the spectral properties of the optical source; as an optical parametric oscillator [20]; and to measure the optically induced refractive index change in Ti: $LiNbO_3$ waveguide [5].

The work presented in this thesis is concerned with the conception, design and fabrication of an integrated optical Fabry-Perot modulator.

Chapter 2 gives a brief outlook on the basic theory and fabrication of optical waveguide in lithium niobate substrate and includes the principle of indiffusion, dependence of index on Ti concentration and

wavelength, influence on waveguide characteristics by the diffusion parameters and the function of the crystal stoichiometry, optical losses in waveguides, outdiffusion of Ti: $LiNbO_3$ waveguides and the fabrication procedures.

Chapter 3 is concerned with the analysis of the electrodes structures that apply the modulating microwave signal in integrated optical modulators. Different types of electrode structures, such as lumped and travelling-wave, as well as symmetric and asymmetric structure, are discussed and conformal mapping method is used to derive the characteristics of the transmission line formed on the substrate. The electrical travelling-wave losses and the way of the depositing are investigated as well.

Chapter 4 investigates the characteristics of high reflective dielectric coatings for the Fabry-Perot optical resonator. It gives a brief analysis of the basic principle of dielectric coating, designs for an optical system for the thickness monitoring, a select on suitable materials and coating structures for different cavities, fabrications and measurements the high reflective coating on lithium niobate and glass slide substrates at the wavelength of 1.15 μm.

Chapter 5 describes the DC characteristics of Fabry-Perot optical modulation. It contributes a brief theoretical review of the Fabry-Perot optical etalon, analyses the maximum available output, minimum available output, maximum available modulation depth and the halfwidth of the cavity relating to the reflectivity of the coating mirrors for both lossless and lossy etalon materials. It also covers the guiding properties of the Fabry-Perot waveguide resonator influenced by the wedge angles, and develops a special technique for the waveguide etalon polishing to minimise the wedge angles.

Chapter 6 considers the thermal properties of the optical waveguide resonator (temperature influence on Fabry-Perot modulation). It investigate the refractive index variation and cavity length shift of the waveguide resonator on lithium niobate substrate versus temperature change by a reflecting mode method and the possible application as a sensitive temperature sensor.

Chapter 7 gives a short discussion on multiple transmission properties of high speed Fabry-Perot modulation. It analyses modulation bandwidth affected by both the double transit effect of the travelling-wave electrodes and the multiple modulated transmission which is not kept in phase each other at high frequency.

Chapter 8 involves the experimental work. The consideration and fabrication of the device, as well as the measurement set-up are described. A high speed response photo-detecting circuit is developed and the experimental results are described and discussed.

REFERENCE

[1]. E. Vogar and A. Neyer, " Integrated-Optic Device on $LiNbO_3$ for Optical Communication ", J. Lightwave Tech. Vol. LT-5, No. 9, pp. 1229- 238, Sep. 1987.

[2]. T. Sueta and M. Izutsu, " High Speed Guided-Wave Optical Modulators", J. Opt. Commun., Vol. 3, pp. 52 - 58, 1982.

[3]. C. M. Gee, G. D. Thurmond and H. W. Yen, " 17-GHz Bandwidth

Electro-optic Modulator ", Appl. Phys. Lett., Vol. 43, pp. 998 - 1000, 1983.

[4]. R. A. Decker, " Travelling-Wave Electrooptic Modulator with Maximum Bandwidth-Length Product ", Appl. Phys. Lett., Vol. 45, pp. 1168 -1170, 1984.

[5]. R. Volk and W. Sohler, " A High Sensitive Excite and Probe Technique to Measure Optically Induced Refractive Index Change in Ti: $LiNbO_3$ Waveguide Resonators ", Topical Meeting on: Integrated and Guided-Wave Optics, pp. 140 - 143, Santa FE, March, 1988.

[6]. R. C. Alferness, L. L. Buhl, M. D. Divino, S. K. Korotky and L. W. Stulz, " Low-Loss Broad Ti: $LiNbO_3$ Waveguide Phase Modulators for Coherent System ", Electron. Lett., Vol. 22, pp. 309 - 310, 1986.

[7]. P. Granesstrand, B. Stoltz, L. Thylen, K. Bergvall, W. Doldissen, H. Heidrch and D. Hoffmann, " Strictly Nonblocking 8 by 8 Integrated Optical Switch Matrix ", Electron. Lett., Vol. 22, pp. 309 - 310, 1986.

[8]. R. C. Alferness and R. V. Schmidt, " Tunable Optical Waveguide Directional Coupler Filter ", Appl. Phys. Lett., Vol. 33, pp. 161 - 163, 1978.

[9]. A. Neyer, " Integrated-Optical Multichannel Wavelength Multiplexer for Monomode System ", Electron. Lett., Vol. 20, pp. 161 - 163, 1978.

[10]. K. Komatsu, M. Kondo and Y. Ohta, " Titanium/Magnesium Double Diffusion Method for Efficient Fibre- $LiNbO_3$ Waveguide Coupling ", Topical Meet, Integrated and Guided Wave Optics,

Atlanta, GA, pap. PP 2-1, 1986.

[11]. H. F. Taylor, " Application of Guide-Wave Optics in Signal Processing and Sensing ", Proc. IEEE. Vol. 75, No. 11, pp. 1524 - 1535, Nov. 1987.

[12] M. Izutsu, A. Enokihara and T. Sueta, " Integrated Optic Temperature and Humidity Sensors ", IEEE J. Lightwave Tech. Vol. LT-4 N0. 7, pp. 833 - 836, July, 1986.

[13]. C. H. Bulmer, " Integrated Optical Sensors in Lithium Niobate ", Optics News, pp. 20-23, Feb. 1988.

[14]. T. Suhara and H. Nishihara, " Integrated Optics Components and Devices Using Periodic Structure ", IEEE J. Quantum Electron. Vol. QE-22. N0. 6, pp. 845 -867,1986.

[15]. H. Haga, M. Ohta, M. Isutsu and T. Sueta, " Integrated Optic Error Detecting Circuit Using Ti: $LiNbO_3$ Interferometric Light Modulators ", IEEE J. Lightwave Tech. Vol. LT-4, No. 7, pp. 799 - 803, July, 1986.

[16]. D. Erasme and M. G. F. Wilson, "Analysis and Optimization of Integrated-optic Travelling Wave Modulators Using Periodic and Non-periodic Phase Reversals", Optical and Quantum Electronics, 18, pp. 203 -211, 1986.

[17]. R. Alferness, S. Korotky and E. A. J. Marcatili, " Velocity Matching Techniques for Integrated Optic Travelling Wave Switch/Modulators", J. Quantum Electron. Vol. QE-20, No. 3, pp. 301, March, 1984.

[18]. K. Atsuki and E. Yamashita, " Transmission Line Aspect of the Design of Broad-band Electro-optic Travelling Wave Modulator ", J. Lightwave Tech. Vol. LT-5, No. 3, pp. 316, March, 1987.

[19]. A. Bruland and W. Sohler, " Reflection Mode Integeated Optical Fabry-Perot Modulator ", 4th ECIO, Glasgow, 1987.

[20]. R. Volk and W. Sohler, " Single Frequency Pumped Double Resonant Integrated Optical Parameter Oscillator of Very High Efficiency ", Topical Meeting on: Integrated and Guided-Wave Optics, pp. 176 - 179, Santa FE, March, 1988.

[21] R. G. Walker, " High-Speed III-V Semiconductor Intensity Modulators", IEEE, J. Quantum Electronics, Vol. 27, No. 3, pp 654-667, March, 1991.

[22] M. Whitehead, A. River, G. Parry, J. S. Roberts, C. Button" Low-Voltage Multiple Quantum Well Reflection Modulator With On: Off Ratio >100:1", Electronics Lett. Vol. 25, pp 884-885, May 1989.

[23] M. Whitehead & G. Parry, " High-Contrsat Reflection Modulation At normal incidence In Asymmertric Multiple Quantum Well Fabry-Perot Structure", Electroncs Lett. Vol. 25, pp 566-568, 1989.

CHAPTER 2 PRINCIPLE AND FABRICATION OF OPTICAL WAVEGUIDES ON LITHIUM NIOBATE SUBSTRATE

2.1 Introduction

Optical waveguides play a crucial role in integrated optics, as low losses (less than 1 dB/cm) [1] and good confinement properties matching with optical fibre profile by optical waveguide [2] are essential for integrated optical devices like modulators, couplers, switches, filters and so on in tele-communication systems. A common technique for making integrated optical devices is based on the formation of a waveguide on a lithium niobate substrate with Ti-indiffusion or proton exchange. Lithium niobate is available in large, transparent, single crystal with excellent electro-optical and acousto-optical properties. Among the available lithium niobate technologies, we pay more attention to the Ti-indiffusion method, as the optical waveguides fabricating by proton exchange suffer high optical losses, degrade on electro-optical coefficient, only support extraordinary modes and may have index profile instability despite the simple fabricating technique, high resistance of optical damage [11],[31],[32].

2.2 The Principle of Indiffusion

The study of titanium indiffusion into lithium niobate substrate has received a great deal of attention, and much effort has been spent in understanding the mechanics, since it was first used in 1974 [7], because a titanium (Ti) indiffused waveguide yields a good light confinement, with a relatively large increase of both ordinary and extraordinary refractive index ($\Delta n_e < 0.04$; $\Delta n_o < 0.02$). Moreover, Ti indiffusion allows the fabrication of optical waveguides supporting both TE and TM modes

[6].

The process by which a lithium niobate crystal is doped with titanium to form an optical waveguide is a combination of chemistry and classical diffusion. According to the present understanding, the titanium incorporation occurs in three identifiable stages [12].

The first stage takes place during the period when the substrate is being heated from the room temperature to the chosen diffusion temperature (around 1000 ^{0}C). At about 500 ^{0}C, the deposited titanium film begins to oxidise. The oxidising reaction is completed by the time when the diffusion temperature is reached, leaving a polycrystalline TiO_2 compound on the surface in place of the Titanium coating.

The second stage is characterised by the formation of a complex source compound at the surface, without significant penetration of titanium into the substrate. Material scientists believe this source compound to be $(Li_{0.25}Nb_{0.75}O_2)_{1-x}(TiO_2)_x$, with x = 0.59 [13]. It is formed by the movement of mobile Li species into the TiO_2 layer, and the subsequent counter diffusion of Nb from the lithium niobate substrate into the volume of the TiO_2 layer and of Ti from the TiO_2 layer into a similar volume in lithium niobate crystal.

The final stage of the doping process is essentially the classical diffusion of the limited supply of titanium from the source compound into the crystal volume. As such, the extent of Ti diffusion depends on the diffusion coefficient and on the time and temperature of the heating treatment. The last two parameters are accurately and easily controlled and provide a convenient method of waveguide adjustment.

So far, the modal characteristics of the waveguide are most strongly influenced by the third stage of titanium incorporation because of the

substantially larger crystal volume that it affects. Therefore, any model of the waveguide characteristics begins with a model of the classical diffusion process for a laterally distributed source, assuming that suitable means have been taken to ensure the stability of the Li_2O content of the crystal. So far, many experiments to measure the diffusion profile and rates for planar and channel diffusion of Ti into lithium niobate have been carried out [14], [15], [16], [17], and all are described well by classical diffusion theory [18]. In the case of diffusion for the waveguide formation, the diffusion time should be long enough , compared to that to deplete the source compound.

The theoretical approach of indiffusion of titanium on lithium niobate substrate, in the assumption of no external perturbation, can be described by Fick's equation [11]. As the problem here has only to be solved in the Y, Z plane (as shown in Fig. 1).

$$\frac{\partial C}{\partial t} = D_y \frac{\partial^2 C}{\partial^2 Y} + D_z \frac{\partial^2 C}{\partial^2 Z} \qquad (2-1)$$

where C is the Ti concentration in Y, Z plane: C(Y, Z), D_y and D_z are the diffusion coefficients along the crystal axes Y and Z, respectively, and are supposed in dependent of temperature. D_y and D_z follow an Arrhenius law:

$$D_{y,z} = D_0^{y,z} \exp\left(-\frac{E_0^{y,z}}{kT}\right) \qquad (2-2)$$

where

D_0^y, D_0^z	diffusion constant in the Y and Z directions
E_0^y, E_0^z	activation energy in the Y and Z directions

k	Boltzmann's constant
T	diffusion temperature (^{0}K)

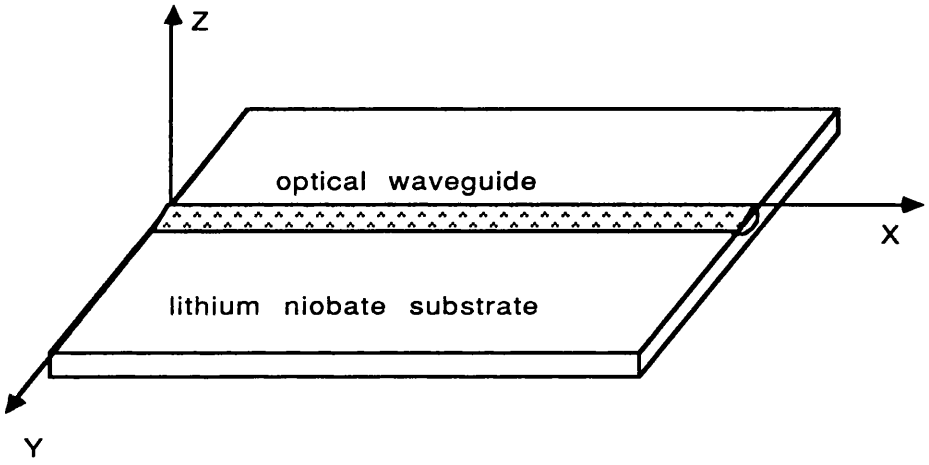

Fig. 2.1 Schematic diagram of indiffused waveguide on lithium niobate

Channel waveguide are fabricated by photolithographically defining a strip of width w from the deposited Ti. In this case, the theoretical concentration profile is separable in lateral and vertical coordinates, Y and Z, and can be written as:

$$C(Y,Z) = C_0 f(Y)\, g(Z) \qquad (2-3)$$

with

$$g(Z) = \exp\left(-\frac{Y}{d_z}\right)^2 \qquad (2-4)$$

$$f(Y) = \frac{1}{2\,\mathrm{erf}\left(\frac{W}{2d_y}\right)} \left\{ \mathrm{erf}\left[\frac{1}{d_y}\left(x+\frac{W}{2}\right)\right] + \mathrm{erf}\left[\frac{1}{d_y}\left(x-\frac{W}{2}\right)\right] \right\} \qquad (2-5)$$

$$C_0 = \frac{2\tau}{\sqrt{\pi}\, d_z} \operatorname{erf}\left(\frac{W}{2d_y}\right) \qquad (2-6)$$

where" erf" is the error function, τ is the thickness of Ti film.
d_y and d_z are the diffusion depth along Y and Z coordinates as :

$$d_{y,z} = \sqrt{4D_{y,z}t} \qquad (2-7)$$

where t is the diffusion time.

2.3 Dependence of Index on Ti Concentration and Wavelength

The index change produced by the doping of the lithium niobate crystal with Ti is decided by the Ti concentration in the crystal anisotropically, as the anisotropic property of lithium niobate. It can be expressed as: [17]

$$\Delta n_{e,o}(Y,Z) = A_{e,o}(C_o, \lambda)[C(Y,Z)]^{\alpha(e,o)} \qquad (2-8)$$

while $\Delta n_{e,o}(Y, Z)$ is the extraordinary or ordinary refractive index change, $A_{e,o}(C_o, \lambda)$ is the proportionality coefficient which depends not only on the optical wavelength but also on the diffusion condition characterised by C_o, and $\alpha(e,o)$ is the constant which is decided by the coordinate of the crystal.

So far, a lot of experimental work, on the measurement of index change vs Ti concentration in the crystal, has been done by several other groups [20], [21], [23]. It has been observed that the index change for the extraordinary axis is in direct proportion to the Ti concentration (α =1),

while the index change for ordinary axis is a non-linear function (α is around 0.5) [17]. As the diffusion condition influence on index change is small enough to ignore, the index change depending on optical wavelength (i.e. dispersion) that can be approximated by :

$$A(\lambda) = 0.552 + \frac{0.065}{\lambda^2_{(\mu m)}} \qquad (2-9)$$

of which the dispersion (Equ. 2-9) is quite large compared with the bulk dispersion of the crystal (Equ. 2-10 & 2-11) [19], [21];

$$n_o(\lambda) = 2.195 + \frac{0.037}{\lambda^2_{(\mu m)}} \qquad (2-10)$$

$$n_e(\lambda) = 2.122 + \frac{0.032}{\lambda^2_{(\mu m)}} \qquad (2-11)$$

With the knowledge of how the index change depends on Ti concentration, the index distribution can be constructed from the Ti concentration profile, we can write :

$$\Delta n(Y, Z) = \Delta n_o f(Y) g(Z) \qquad (2-12)$$

Having enforced the conservation of the number of Ti atoms, the peak index change Δn_0 is given by :

$$\Delta n_0 = \frac{2\tau A(\lambda)}{\sqrt{\pi}\, d_z} \operatorname{erf}\left(\frac{W}{2d_y}\right) \qquad (2-13)$$

We can give a example of the index change versus the Ti concentration for both extraordinary and ordinary axis at a wavelength of 0.63 μm [21], as shown in Fig. 2.2. We find that the index changes are exactly the same for a Ti concentration of 0.75% for both extraordinary and ordinary modes, while the index change in the ordinary axis is larger than that in the extraordinary axis for a Ti concentration is less than 0.75%; the index change in the ordinary axis is smaller than that in the extraordinary axis for a Ti concentration is greater than 0.75%.

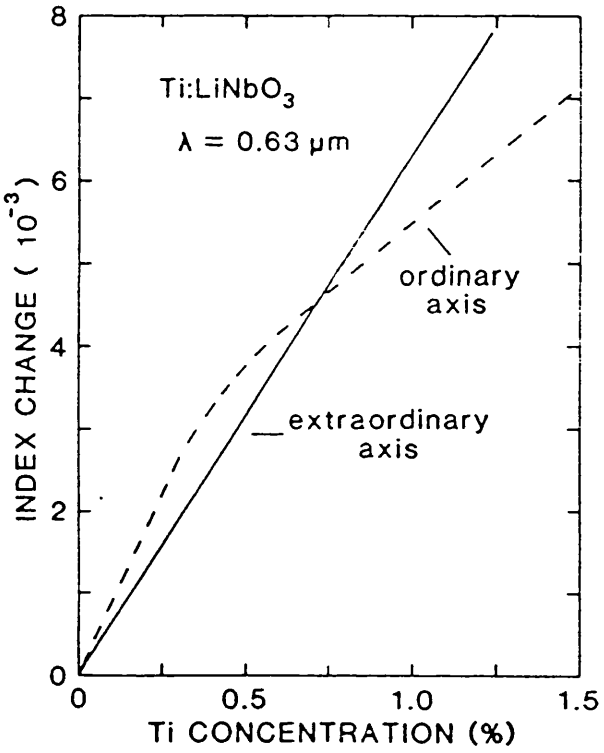

Fig. 2.2 Index change vs Ti concentration (from ref. 19)

2.3 Influence on Waveguide Characteristics by the Diffusion Parameters and the Function of the Crystal Stoichiometry

The characteristics of the optical waveguide are mainly decided by

the diffusion coefficients both in extraordinary and ordinary axis, the diffusion time and diffusion environment (wet or dry oxygen, the flowing rate of the gas). Moreover, the diffusion coefficients (d_y, d_z) play a more important role in the fabrication, by which the index change distribution profile is mainly decided, because the diffusion coefficients depend on the diffusion temperature T and the crystal stoichiometry which decide the diffusion constants D_o^y, D_o^z, while the activation energies E_0^y, E_0^z, are independent of the crystal stoichiometry [6].

So far, much experimental and summary work has been done [6], [17], [22], [23], [24], [25], [26], however, the relation between the waveguide characteristics and the diffusion conditions have not been established and the results are different from laboratory to laboratory [26], which is believed caused by the composition difference of the stoichiometry and the fabrication environment. Experiments have been carried out to quantify the compositional dependence of the diffusion constant and have shown it to vary by over a factor of 4 over the range 48 to 50 mole % Li_2O composition [25]. Fortunately, for the crystal having a congruent composition (48.6 mole % Li_2O), the diffusion coefficient and the activation energy, for all crystal orientations at 1050 ^{0}C, is almost the same ($D_0 = 1.1\times10^{-12}$ cm^2/s, E = 2.2 eV) [25], [27].

Diffusion time is the most easily controllable parameter for fabricating waveguides. In order to get good waveguides, a deeply indiffused waveguide is preferred, as it gives low optical transmission losses and good optical mode profile to match the mode of optical fibre [28], [29]. High diffusion temperature is chosen to get deep indiffusion waveguide [6].

Diffusion environment has a great influence on the diffusion coefficient. Much investigation to create deep waveguides [28] has been

done as a function of crystal orientation and diffusion ambient for a temperature range from 1050 to 1100 ^{0}C. The diffusion parameters for waveguides diffused in a water vapor environment are always larger than ones diffused in a dry ambient. Differences in the diffusion coefficients for the extraordinary mode as high as 90%, 66% and 84% are measured for X-, Y-, and Z-cut crystals, respectively. Smaller but noticeable difference are detected for the ordinary mode on diffusion coefficients. Similar enhancing effects of the water vapour are also obtained for the surface-index change. Severe rough surface finish and surface contouring, revealing a etchedlike appearance, are observed on Z-cut substrates diffused in wet atmosphere. In general, substrates diffused in dry oxygen produced relatively smoother surfaces

.

2.4 Out-Diffusion of the Ti: $LiNbO_3$ Waveguides

Out-diffusion on lithium niobate crystals can be used to produce planar waveguide on extraordinary mode by out-diffusing lithium oxide (Li_2O) from the crystal surface using thermal treatments for several hours at high temperature (1000 - 1100 ^{0}C) in a vacuum or oxidising ambient. However, it causes disaster to the channel waveguides fabricated by titanium indiffusion, since it forms a planar waveguide for the extraordinary mode which dissipated the optical power from the channel waveguides causing extra optical losses and degrading the electro-optic performance.

The basic principle of out-diffusion is based on the fact that lithium niobate can crystallise in the slightly non-stoichiometric form $(Li_2O)_y(Nb_2O_5)_{1-y}$. Although the ordinary index n_0 is not affected as Li_2O is removed from crystal surface, the extraordinary index n_e increases approximately linearly as y decreases in the $0.48 < y < 0.50$ range. So, because of the high mobility of lithium ions, a decrease of y may be easily achieved by out-diffusion of Li_2O from the surface. Thus, out-diffusion

gives rise to an extraordinary index gradient, with the maximum at the surface and a gradual in depth decrease approaching the bulk index [30].

The refractive index profile depends on the parameters of the diffusion and vaporisation process at the out-diffusion temperature. However, the extraordinary index profile in the out-diffused layer assumes, in general, a form very close to the complementary error function [30]:

$$\Delta n_e = \Delta n_e(0)\ \mathrm{erfc}\{\ \frac{x}{\sqrt{4Dt}}\ \} \qquad (2-14)$$

where D is the diffusion coefficient ($D = 1.5\times10^{-9}$ cm^2/s, and 4.2×10^{-9} cm^2/s for diffusion parallel, and perpendicular to the optic c-axis at 1100 ^{0}C, respectively), t is the diffusion time, x is the depth, and $\Delta n_e(0)$ is the index change at the surface ($\Delta n_e(0) = 10^{-3}$ to 10^{-2}) [6].

In order to get rid of out-diffusion on Ti: $LiNbO_3$ waveguides, a lot of investigation has been done on suppression of out-diffusion of Li_2O. A very effective and simple method of suppressing out-diffusion appears to be Ti indiffusion in the presence of water vapor (pure O_2 bubbling through a fixed volume of pure water at 80 - 90 ^{0}C during diffusion), but it increases the in-plane scattering levels [49]. However, it was observed that there was no complete suppression of out-diffusion in samples annealed in wet oxygen atmosphere, both for Y- and Z-cut substrates. Alternatively, the indiffusion at a high temperature (1050 ^{0}C) in dry oxygen for long diffusing time (over 10 hours) is preferred, as it was found that smaller diffusion coefficient and surface index change for samples diffused in dry oxygen compared to wet, as it is believed that the absence of out-diffusion modes in the dry case is due to the much deeper out-diffusion guides (150 - 200 micro) than the Ti-indiffused channel

guides (around 5 micro) [28]. Under this condition, in fact, reduced surface roughness, decreased uncertainty in the refractive index profile, and increased optical damage resistance have been observed. In order to achieve low losses, out-diffusion free optical waveguides, Neyer and Pohlman [23] fabricated reproducible waveguides by placing the sample in a closed platinum crucible in which it makes the diffusion parameters, such as temperature uniform tolerance and gas flow, are easy to control, as well as chemical cleanness, since the sample is in small area. These waveguide are also made out-diffusion free as the small platinum box can stop the Li_2O reaching the quartz tube and create a Li_2O rich atmosphere around the substrate, of which it is believed the Li_2O will react with quartz chemically, but platinum does not react with Li_2O. In this project, we use lithium niobate powder to create the Li_2O rich area because of the high expense of platinum material, and we obtained very good low losses, out-diffusion free waveguide on Y-cut lithium niobate which will be discussed later.

2.5 Light-Induced Refractive Index Change (or Optical Damage) in Ti: $LiNbO_3$ Waveguides

Changing of the refractive index of $LiNbO_3$ crystals during exposure to light have been discovered by Ashkin et al [33]. By nonuniform illumination, charge carriers are excited and transferred to different sites. By the means, electrical space charge field are set up modulating the index of refraction via the the electro-optical effect.

On the one hand, these photorefractive effects are of considerable interest for the storage of volume phase holograms [34]; on the other hand, however, the light-induced index changes are feared as "optical damage" effects. They degrade the quality of integrated optical components as modulators, switches or spectrum analysers based on Ti: $LiNbO_3$ waveguides, or even destroy them. Unfortunately, the Ti:

indiffused optical waveguides are more sensitive to optical damage effects than the bulk material [7].

Optical damage effects are caused by transition metal impurities which occur in different valence states in $LiNbO_3$. Fe ions play a special role in this existing as Fe^{2+} and Fe^{3+} centres in the crystal [36], as Fe concentration of several ppm are always found even in undoped (normally pure) crystals. Furthermore, Fe ions very effectively influence the light-induced charge transport and the effect of Fe ions is more than one order of magnitude larger than that other impurities, such as Cu, Mn, Ni or Cr [37].

So far, much work has been done to investigate the photorefractive effect on Ti: $LiNbO_3$ waveguides, and it has been found that this effect severely limits the optical power input into the waveguides at shorter wavelength (e.g., $\lambda \leq 0.8$ micro) to several microwatts, only. At $\lambda \geq 1.3$ micro, however, no significant degradation of electro-optical devices is predicted for input power levels up to 5 mW [39]. Recently, Zhoug et al showed the lithium niobate doped with approximately 5% or more magnesium oxide (MgO) exhibits a remarkablely reduced photorefractive response compared with undoped lithium niobate.

2.6. Optical Losses in the Waveguides

The fabrication of low losses optical waveguide is essential for integrated circuits before it can been used to practice the many proposed applications [19], [41]. The losses in the waveguides can be generally attributable to three different mechanisms: scattering, absorption and radiation. Scattering loss usually predominates in glass or dielectric waveguides, while absorption loss is most important in semiconductors. Radiation losses become significant when waveguides are bent through a

curve [1].

There are two types of scattering loss in optical waveguides: volume scattering and surface scattering. Volume scattering is caused by imperfections, such as voids, contaminant atoms and crystalline defects, in the volume of the waveguide, as well as fluctuation of the waveguide, refractive index fluctuation caused by compositional variation and dimensional fluctuation associated with variation in the height and/or width of the waveguide. While surface scattering loss is generated by roughness of the surface, it can be quite significant even for relatively smooth surfaces, particularly in the case of high order modes [41].

Absorption losses in amorphous and in crystalline ferroelectric materials, such as $LiTaO_3$ and $LiNbO_3$, are generally negligibly small compared to scattering loss, unless contaminant atoms are present. However, in semiconductor waveguides, significant losses occur because of both interband (or band edge absorption) and free carrier absorption. Interband absorption can be explained as: photons with energy greater than the bandgap energy are strongly absorbed in semiconductors by giving up their energy to raise electrons from the valence band to the conduction band. This effect is generally very strong, resulting in absorption coefficients that are larger than 104 cm^{-1} in direct bandgap semiconductors [42]. To avoid interband absorption, one must use a wavelength that is significantly longer than the absorption edge wavelength of the waveguide material. While free carrier absorption, sometimes called intraband absorption, is that which occurs when a photon gives up its energy to an electron already in the conduction band, or to a hole in the valence band, thus raising it to higher energy. Usually free carrier absorption is taken to include absorption in which electrons are raised out of shallow donor states near the conduction band edge, or holes are excited into the valence band from shallow acceptor states near the valence band edge.

Radiation losses is stated as that optical energy which can be lost from waveguided modes by radiating, in which case the energy is emitted into the media surrounding the waveguide and is no longer guided. Radiation losses can occur from planar waveguides as well from channel waveguides. There are two sorts of radiation losses, namely, radiation loss from planar or straight channel waveguides and the loss from curved channel waveguides.

Radiation loss from either planar or straight channel waveguides is the attenuation caused by surface-roughness-induced radiation from planar waveguides or by dimension fluctuation from straight channel waveguides. It is generally negligible for well confined modes, which are far from cutoff, compared to scattering and absorption losses.

Because of distortions of the optical field that occurs when guided waves travel through a bend in a channel waveguide, radiation loss can be greatly increased. In fact, the minimum allowable radius of curvature of a waveguide is usually limited by radiation losses rather than fabrication tolerance. Since waveguide bends are a necessary part of all but simplest OIC's, the radiation losses from a curved waveguide must be considered in circuit design.

So far, great deal of work has been done on the fabrication of low loss and low scattering waveguides. The absorption loss of straight channel waveguides is reduced as low as 0.3 dB/cm at 633 nm and about 0.1 dB/cm at 1300 nm [43], of which predominant loss mechanism is attributed to scattering loss. In-planar scattering which directly determines the signal-to-noise ratio and dynamic range in optical signal processing device, such as integrated optical spectrum anayliser is investigated in planer waveguides as a function of the diffusion time

and temperature [44], [45]. It has been found that as diffusion time and temperature are increases, in-planar scattering firstly decreases but then eventually increased. the eventual increase in in-planar scattering is, apparently, because of growth of subsurface defects of the waveguides. For the temperature range of 980 ^{o}C to 1050 ^{o}C, the lowest in-planar scattering can be achieved for diffusion time around 10 hours [45].

To increase the packing density of integrated optical circuits, it is necessary to allow for small-radius bends which initiate two kinds of losses: one is mode mismatch losses which occur at the transition between straight and bent waveguides, as well as at the transitions between both bent waveguides, the other is bending losses, which increase strongly with decreasing bend radius if the radius is below a critical value [9]. A significant reduction in bend losses in Ti: $LiNbO_3$ waveguides by means of a double-indiffusion method was reported [9], [10]. The method to influence the refractive-index profile of Ti: $LiNbO_3$ waveguides is offered a second diffusion with a material of low index, such as MgO. The advantage of MgO when applying it to Ti: $LiNbO_3$ waveguides is the fact that the diffusion constant of MgO is about a order of magnitude larger the that of Ti in $LiNbO_3$. This allows a second diffusion at low temperatures so that the influence of the already Ti-diffused waveguide is negligible. the basic idea of improving Ti: $LiNbO_3$ waveguide bends is to increase the slope of the refractive index profile at outer side of the curved waveguide. In term of phase velocities, this effect can be described by an increased velocity at the outer side of the bend which even exceeds the phase velocity in the $LiNbO_3$ substrate [10]. The reduction in MgO: Ti: $LiNbO_3$ waveguides bend loss, in the bend radius around 10mm, is by a factor as large as eight (if total bend excess loss of 1 dB is allowable), on the condition of putting about 20 nm thick and 15 micro wide MgO film which is carried out for 1.5 h at 900 ^{o}C with a flow of dry synthetic air at a rate of 1 lit./min. [46].

2.7 The Fabrication Procedure

The fabrication of optical waveguides on $LiNbO_3$ substrate is based on the standard processing technique similar to semiconductor industries that the basic steps consist of photolithography, metal film deposit and indiffusion the metal atoms into $LiNbO_3$ substrate at a high temperature .

In order to fabricate high quality optical waveguides on lithium niobate substrate, an important feature of titanium-in-diffusion waveguide fabrication, in addition to being convenient and reproducible, is the independent control of all the fabricating procedure and waveguide parameters: waveguide width, diffusion depth and the waveguide-substrate index difference. The waveguide width is controlled by the width of the mask photolithographically. Photoresist is spun on the oriented, polished and cleaned lithium niobate substrate. The desired waveguide width and path are delineated by opening window in the photoresist using ultraviolet exposure through a mask. The titanium thickness provides control over the index change; Titanium, carefully controlled thickness, is deposited over the entire crystal surface by the evaporation (either electron-beam or resistively heater induced) or radio-frequency (RF) sputtering. The titanium to form the channel waveguides is obtained by dissolving the photoresist to 'lift-off' the undesired metal. Alternatively, etching technique (especially plasma etching) may be used to transfer the waveguide pattern into the titanium strip. The waveguide depth is controlled by the time and temperature of the diffusion as shown in Fig. 2.3.

The work on fabricating optical waveguides, on lithium niobate substrate, is done in the Clean Room, which is Class 1000, at Dept. of Electronic and Electrical Eng. in University College, London. The

fabricating procedure is as following:

The first step is cleaning: put Trichloroethylene into two clean Petri dishes and put the samples in to get rid of wax and grease, and cleaning twice, wash it in Acetone twice to eliminate Trich, then clean it in Propan 2-01 twice. Put it in cold 50%H_2O_2/50%H_2SO_4 for 20 min. then put in Nitric Acid for another 5 min., wash it in D.I. water and dry with filtered Nitrogen. Bake it for 20 min. in 85 ^{0}C oven.

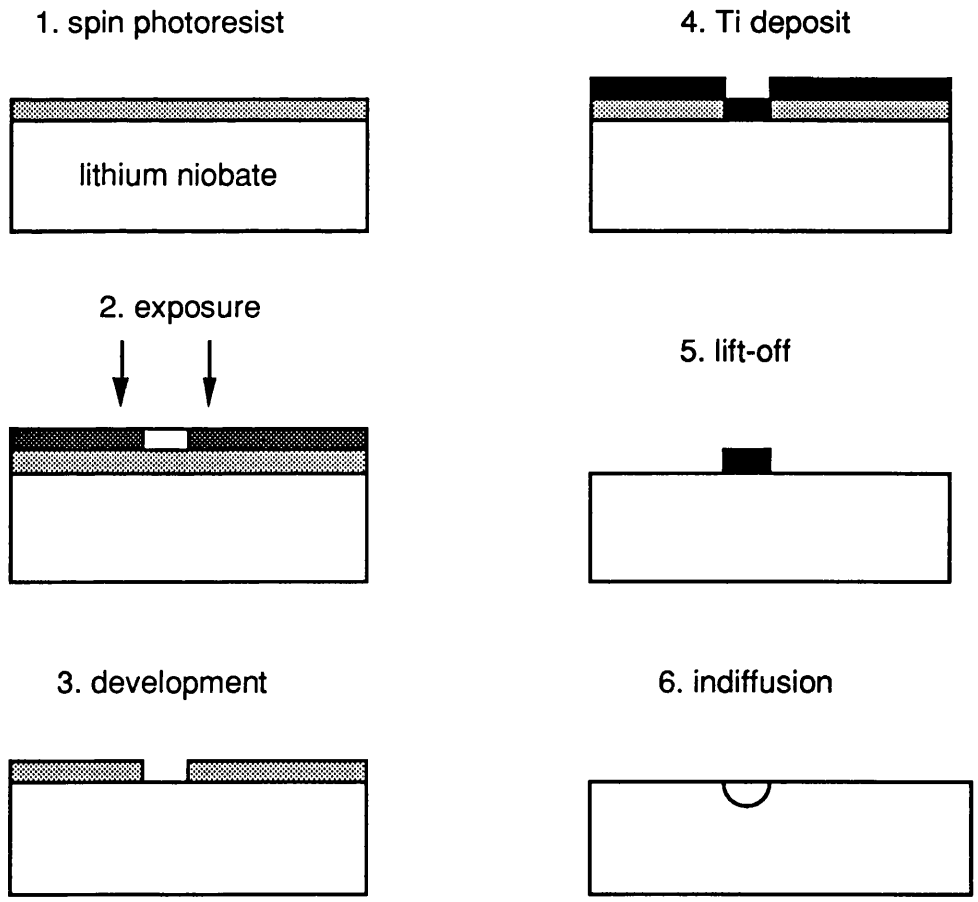

Fig. 2.3 The procedure for Ti: lithium niobate waveguide Fabrication

The second step is photolithography: drop some photoresist (AZ 4110 or S 1400 which are the very suitable photoresists for lift-off) from filtered syringe on the crystal, spin it for 20 sec. at speed of 4000 rev./min. and bake it for 20 min. in 85 ^{0}C oven. Expose at the mask aligner with UV light for 8 sec. and put in Chorobenze for 15 min., then develop it in Dev. 351 mixed with D.I. water of 1:3 for 1 min. 30 sec. and wash in D.I. and dry it, so we can have the waveguide pattern on lithium niobate substrate.

The third step is titanium depositing: load the crystal into the Evaporator 12E with a class slide holder, pump down the vacuum to 10^{-7} Torr., evaporate the titanium at rate of 0.1 nm/sec at a current of 45 amp. As titanium reacts with tungsten which is easily broken, we must pay great attention on the operation. Finally, we obtain the titanium film of 30-150 nm for the waveguide of different wavelength and "lift-off" the unwanted titanium.

The last step is diffusion: the diffusion is carried out on the quarts crystal furnace, with the temperatures ranging from 1000 to 1050 ^{0}C for the samples. The diffusion time are 6 to 17 hours for different waveguides, which is depends how deeply diffused the waveguides are.

2.8 The Experimental Results

To get the high quality waveguides, the different diffusion environment has been tried, both wet and dry oxygen with different flow rates. The loss and out-diffusion properties have been improved quite a lot. The characteristics of the waveguides for different fabrication parameters are given as table 1. From this table, we find that the deeper the indiffusion, the less the optical losses, for 2.9 μm deep diffusion, we get -18dB total insert losses; for 5.5 μm diffusion, we get -7dB losses; and for 6.4 μm diffusion, we only get about -3.5dB losses. We also notice that

the deeper of the indiffusion, the less the outdiffusion between the shallow and deep indiffused waveguides; The difference on the waveguide characteristics is not significantly noticeable for optical grade and acoustic grade crystals; The flowing rate of oxygen plays a crucial role on the out-diffusion control as it may change the Li_2O environment during the diffusion; Diffusion temperature, which made the deep diffusion much easier, together with the diffusion time can be used to control the diffusion processing for good waveguides; the titanium width and thickness are the designing parameters for a desired mode profile and guiding properties for different wavelength, and normally, the longer the wavelength, the wider and thicker the titanium strip.

For the Fabry-Perot Integrated optical modulator, we require not only low optical losses, but also out-diffusion free optical waveguides which forms a planar waveguide overlapping the channel waveguides. Since the Fabry-Perot cavity is very sensitive to the optical losses inside the cavity, it degrades the performance severely. Moreover, we deploy the TE mode of the waveguide for Fabry-Perot modulator as the waveguide is placed between the electrodes. Nevertheless, we need to form the waveguides on Y-cut or X-cut lithium niobate in order to fulfill the maximum electro-optical coefficient of r_{33}.

To make low optical, out-diffusion free waveguide on Y-cut lithium niobate substrate, we designed a special diffusion set-up which is shown in Fig. 2.4. In this set-up, we use powder lithium niobate to create a Li_2O rich atmosphere round the specimen, forming a 'closed box' by several pieces of lithium niobate blocks to depress the out-diffusion of the waveguide substrate inside the box. We achieved very good low optical losses (the total insertion losses of 3.5 to 6 dB), out-diffusion free single mode optical waveguide at the wavelength of 1.15 μm at the diffusion temperature of 1050 ^{o}C for 10 hours with oxygen flowing rate of 0.1

lit./min which made the finance chemical clean without carrying the Li_2O away significantly

2.9 Conclusion

In this chapter, we have discussed and summarised the basic principle of indiffusion, refractive index change dependence on titanium concentration and operation wavelength, optical waveguide losses, characteristics influenced by the function of crystal stoichiometry, light-induced refractive index change or optical damage, out-diffusion and its depression on Ti: indiffused optical waveguide on lithium niobate substrate. We also investigated the influences of each parameter like diffusion temperature, diffusion time, diffusion atmosphere (the rate of flowing dry or wet oxygen), width and thickness of the titanium strips. The diffusion parameters were optimised to good guiding performance and a special diffusion set-up was established to achieve the low optical losses, out-diffusion waveguides for Y-cut lithium niobate substrate at the wavelength of 1.15 μm, which will be essential to the Fabry-Perot cavity.

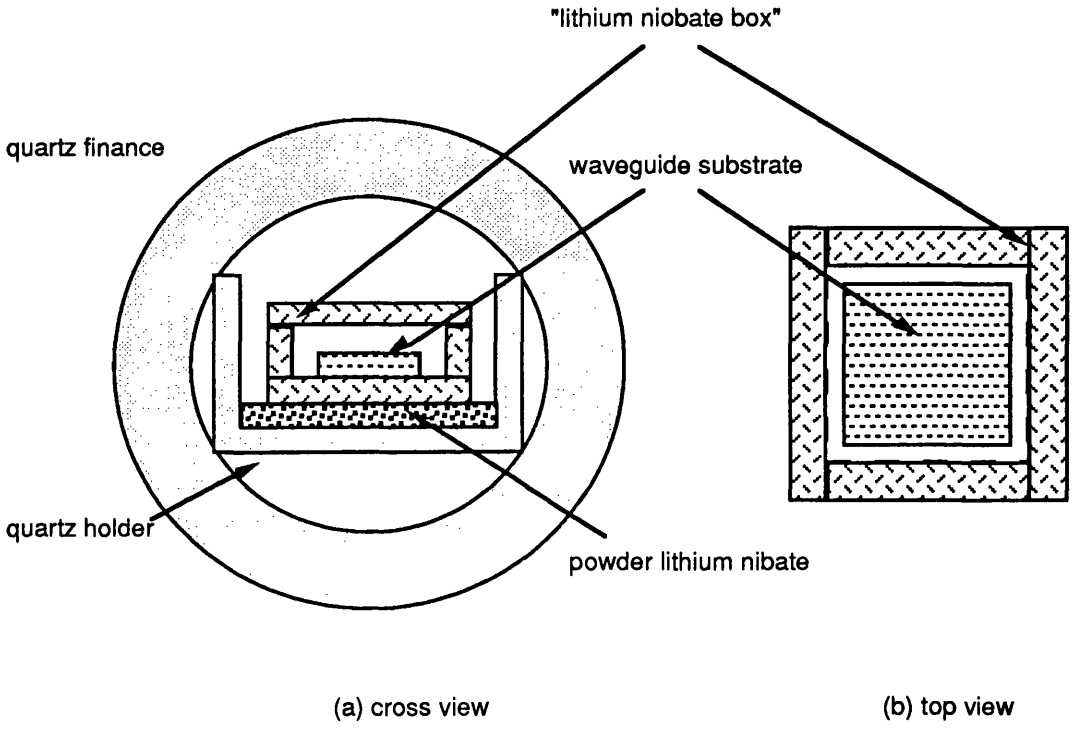

Fig. 2.4 The special diffusion set-up for lithium niobate waveguide fabrication

TABLE 1

The properties of optical waveguide fabrication at 1.15μm for Z-cut

samples / properties	No. 1,2,3	No. 4,5,6	No. 7,8	No. 1,2,3	No. 4,5,6
length of waveguide	2.0 cm	2.2 cm	1.8 cm	2.0 cm	2.2 cm
Ti thickness	70 nm	90 nm	75 nm	70 nm	90 nm
diffusion time	8 hrs	10 hrs	17 hrs	8 hrs	10 hrs
strip width	6 micro	6 micro	6 micro	3 micro	3 micro
diff. condition	wet	dry	dry	wet	dry
oxygen rate	1 lit/min	2 lit/min	0.2 l/m	1 lit/min	2 lit/min
diff. temp.	1000 C	1045 C	1040 C	1000 C	1045 C
crystal quality	acoustic	optical	acoustic	acoustic	optical
out-diffusion for extra. mode	severe	slight	slight	severe	slight
calculated depth sigma+	2.9 micro	5.5 micro	6.4 micro	2.9 micro	5.5 micro
calculated surface sigma	3.4 micro	4.9 micro	6.0 micro	3.4 micro	4.9 micro
calculated B value*	0.048	0.265	0.251	0.0	0.121
number of mode	1	2	1	nearly cut-off	1
total insert losses for TE	-18 dB	-7 dB	-3.5 dB		−9 dB
total insert losses for TM		-6.5 dB			−8 dB

2.9 REFERENCE

[1]. Robert G. Hunsperger, 'Integrated Optics: Theory and Technology', 2nd ED, Speringer-Verlag, 1983.

[2]. E. Voges and A. Neyer, 'Integrated-Optic Device on $LiNbO_3$ for Communication', J. Lightwave Tech. Vol. LT-5, No. 9, PP 1229 - 1238, 1987.

[3]. H. Inoue, K. Hiruma, K. Ishida, T. Asai and H. Matsumura, 'Low Loss GaAs Optical Waveguides', IEEE J. Lightwave Tech., Vol. LT-3, No. 6, PP 1270 -1275,1985.

[4]. P. W. A. McIlroy, P. M. Rodgers, J. S. Singh, P. C. Spurdens and I. D. Henning, 'Low-Loss Single-Mode InP/InGaAsP Waveguides Grown by MOVPE', Electronics Lett., Vol. 23, No. 13, pp 701-703, 1987.

[5]. Y. J. Chen, E. S. Elman, S. W. Brown and G. J. Sonek, 'Multiple Quantum Well GaAs/AlGaAs Waveguides for Integrated Optics', ECIO 87, Proc. of 4th Europ. Con. on I.O., pp 86-89, 1987.

[6]. M. N. Armenise, 'Fabrication Techniques of Lithium Niobate Waveguides', IEE Proc. Vol.135, Pt. J. No. 2, 1988.

[7]. Schmidt, R.V. and Kaminom, I.P., 'Metal-Diffused Optical Waveguide in Lithium Niobate', Appl. Phys. lett., 25, pp 458-460, 1974.

[8]. Noda, J. and Iwasaki, H., 'Impurity Diffusion into $LiNbO_3$ and

$LiTaO_3$', Proc. 2nd Meeting on Ferroelectronic Materials and Their Applications, pp 149-154, 1979.

[9]. J. Noda, M. Fukuma and S. Saito, 'Effect of Mg Diffusion on Ti-diffused $LiNbO_3$ Waveguides', J. Appl. Phys., 49, pp 3150-3154, 1978.

[10]. K. Komatsu, M. Kondo and Y. Ohta, 'Titanium/Magnesium Double Diffusion Method for Efficient Fibre- $LiNbO_3$ Waveguide Coupling', Electron Lett. 22, pp 881-882, 1986.

[11]. R. Chen and W. S. C. Chang, 'Anomalos Attenuation and Depolarization Scattering In y-Cut $LiNbO_3$ Proton Exchange Waveguides', IEEE J. Quantum Elec. Vol. QE-22, No. 6, pp 880-881, 1986.

[12]. M. N. Armenise, C. Canili and M. DeSario, 'Characterization of $(Ti_{0.65}Nb_{0.35})O_2$ Compound as Source for Ti Diffusion During Ti: $LiNbO_3$ Optical Waveguides Fabrication', J. Appl. Phys., 54(1), pp 62-71, 1983.

[13]. C. E. Rice and R. J. Holmes, J. Appl. Phys. 1986.

[14]. M. Minakata, S. Saito and M. Shibata, 'Two-Dimensional Distribution of Refractive-Index Changes In Ti-Diffused $LiNbO_3$ Strip Waveguides', J. Appl. Phys. 50(5), pp 3063-3067, 1979.

[15]. G. J. Griffiths and R. J. Esaile, 'Analysis of Titanium Diffused Planar Optical Waveguides in Lithium Niobate', IEEE Quantum Elec., Vol. QE-20, No. 2, pp 149-159, 1984.

[16]. W. K. Burns, P. H. Klein, E. J. West and L. E. Plew, 'Ti Diffusion in

Ti: $LiNbO_3$ Planar and Channel Optical Waveguides', J. Appl. Phys., 50(10), pp 6175-6182, 1979.

[17]. S. Fouchet, A. Carenco, C. Daguet, R. Guglielmi and L. Riviere, 'Wavelength Dispersion of Ti Induced Refractive Index Change in $LiNbO_3$ as a Function of Diffusion Parameters', J. Lightwave Tech., Vol. LT-5, No. 5, pp 700-708, 1987.

[18]. J. Crank, 'The Mathematics of Diffusion', 2nd ED., Oxford Univ. Press, 1975.

[19]. Lynn D. Hutcheson, ED, 'Integrated Optical Circuits and Components: Design and Applications', 1st ED, Marcel Dekker, Inc.,1987.

[20]. H. Naitoh, M. Nunosiita and T. Makayama,'Mode Control of Ti-diffused $LiNbO_3$ Slab Optical waveguide' Appl. Opt., 16:2546, 1977.

[21]. M. Minakata, S. Saito, and S. Miyazawa, 'Precise Determination of Refractive-index Changes In Ti-Indiffused $LiNbO_3$ Optical Waveguides', J. Appl. Phys., 49(9), pp 4677-4682,1978.

[21]. The Catalogue of Lithium Niobate for Optical Waveguide Substrates, Crystal Technology Inc.

[22]. R. J. Holmes and D. M. Smyth, 'Titanium Diffusion into $LiNbO_3$ as a Function of Stoichiometry', J. Appl. Phys. 55(10), pp 3531-3535,1984.

[23]. K. Sugii, M. Fukuma and H. Iwasaki, 'A Study on Titanium Diffusion into $LiNbO_3$ Waveguides by Electron Probe Analysis and

X-Ray Diffraction Methods', J. Material Sci.,13, pp 523-533, 1978.

[24]. E. A. Leone, A. J. Signorelli, S. Sriram and P. Vohralik, 'Characterization of Ti In-Diffused Waveguides Using Secondary Ion Mass Spectometry (SIMS) and Electron Microprobe Analysis (EMPA)', SPIE Vol. 704, pp94-101, 1986.

[25]. W. E. Lee, 'The Application of Transmission Electron Microscopy to the Study of Microstructure in $LiNbO_3$ Optical Waveguides', SPIE Vol. 704, pp 102-114, 1986.

[26]. C. H. Bulmer and W. K. Burns, 'Polarization Characteristics of $LiNbO_3$ Channel Waveguide Directional Couplers', J. Lightwave Tech. Vol. LT-1, No. 1, pp 227-236, 1983.

[27]. J. Ctyroky, M. Hofman, J. Janta and J. Schrofel, '3-D Analysis of $LiNbO_3$: Ti Channel Waveguides and Directional Couplers',IEEE J. Quantum Electronics, QE-20, pp 149-159, 1984.

[28]. O. Eknoyan, A. S. Greenblatt, W. K. Burns and C. H. Bulmer, 'Characterization of Ti: $LiNbO_3$ Deep Waveguides Diffused in Dry and Wet Oxygen Ambient', Appl. Opt., Vol. 25, No. 5, pp 737-739, 1986.

[29]. N. Naitoh, M. Nunoshita and T. Nakayama, 'Mode Control of Ti-diffused $LiNbO_3$ Slab Optical waveguide', Appl. Opt. Vol.16, No. 9, pp 2546 -2549, 1977.

[30]. J. R. Carruthers and I. P. Kaminow, 'Optical Waveguiding Layer in $LiNbO_3$ and $LiTaO_3$', Appl. Phys. Let., No.22, pp 326-328, 1973.

[31]. R. M. De La Rue, A Loni, A. Lambert, J. F. Duffy, S. M. Al-Shukri,

Y. L. Kopylov and J. M. Winfield, 'Proton-Exchange in Lithium Niobate and Lithium Tantalate', ECIO 87, Proc. of 4th Europ. Con. on I.O., pp 48-53, 1987.

[32]. J. J. Veselka and G. A. Bogert, 'Low-Insert-Loss Channel Waveguides in $LiNbO_3$ Fabricated by Proton Exchange', Electronics Lett., Vol. 23, No.6, pp 265-266, 1987.

[33] A. Ashkin, G. D. Boyd, J. M. Dziedzic, R. G. Smith, A. A. Ballman, J. J. Levinstein and K. Nassau, Appl. Phys. Lett. 9, pp-72,1966.

[34] J. Jackel, A. M. Glass, G. E. Peterson, C. E. Rice, D. H. Olson and J. J. Veselka, 'Damage-Resistant $LiNbO_3$ Waveguides', J. Appl. Phys., 55 (1), pp269-270, 1983.

[35] L. McCaughan and E. J. Murphy, 'Influence of Temperature and Initial Titanium Dimension on Fibre-Ti: $LiNbO_3$ Waveguide Insert Loss at l = 1.3 μm', IEEE J. Quantum Electronics, Vol. QE-19, No. 2, pp 131-135,1983.

[36] A. Kurz, E. Kratzig, W. Keune, H. Engelman, B. Dischler and A. Rauber, Appl. Phys. Lett., 12, p-355,1977.

[37]. E. Kratzig and H. Kurz, Ferroelectronics, 13, pp-295, 1976.

[38] A. M. Glass, I. P. Kaminow, A. A. Ballman, and D. H. Olson, 'Absorption Loss and Photorefractive Index Change in Ti: $LiNbO_3$ Crystal and Waveguides', Appl. Opt. 11-9 pp276, 1980.

[39] G. T. Harvey, G. Astfalk, A. Y Feldblum and B. Kassahum, 'The Photorefractive Effect in Titanium Indiffused Lithium Niobate

Optical Directional Coupler at 1.3 μm', IEEE J. Quantum Electronics, QE-22, pp 939-946,1986

[40] G. Zhong, J. Jian, Z. Wu, 'Measurement of Optically Induced Refractive Index Damage of Lithium Niobate Doped with Different Concentration of MgO', The Proceeding of the 11th Internationall Quantum Electronics Conference, IEEE Catalog No. 80CH, 1516-0, pp 631, New York, 1980.

[41] T. Tamir, ED, 'Integrated Optics', 2nd ED, Springer-Verlag,1979.

[42] M. Ali Omar, 'Elementary Solid State Physics: Principle and applications', 1st ED, Addison-Wesley Publication Company, 1975.

[43] V. Gerick, P. Hertel, E. Kratzig, J. P. Nisius and R. Sommerfeldt, 'Light-Induced Index Change in $LiNbO_3$: Ti Waveguides', Appl. Phys. B44, pp155-162, 1987.

[44] J. Singh and R. De La Rue, 'An Experimental Study of In-Plane Light Scattering in Titanium Diffused Y-cut $LiNbO_3$ Optical Waveguides', J. Lightwave Tech., Vol. LT-3, N0. 1 pp 67-76, 1985.

[45] M. N. Arwenise, M. De Sario, C. Canali, P. Franzosi, J. Singh, R. N. Hutchins and R. M. De La Rue, ' In-plane Scattering in titanium-Diffused $LiNbO_3$ Optical Waveguides', Appl. Phys. Lett., 45(4), pp326-328, 1984.

[46] B. Schuppert, 'Reduction of Bend Losses In Ti: $LiNbO_3$ Waveguides through MgO Double Diffusion', Elec. Lett., Vol. 23, No. 15, pp 797-798, 1987.

CHAPTER 3 ELECTRODE STRUCTURE DESIGN FOR INTEGRATED OPTICAL MODULATOR

3.1 Introduction

As the data rates for fibre optic communication increase up to the GHz range, the integrated optical modulators are becoming more and more attractive than the directly modulated semiconductor laser diodes of which the modulation speeds are limited to the resonance frequency and the modulation efficiency is inversely proportional to the square of the modulation frequency, more important, the frequency effect make the high rate long distance fibre communication impossible [1]. By comparison, the external modulators have dominant advantages over semiconductor laser diodes even though they cause more optical losses and need more electrical power to drive than semiconductor laser diodes

[illegible] discussed in ref [2].

In integrated optical modulators, there are three parameters which dominate the modulation characteristics, namely optical property, electrical property and the velocity mismatch between the optical signal and electrical signal which means that the velocities of the two signal travelling along the substrate are different, and each of them would be affected by several other factors.

In this chapter, we are going to investigate the properties of the travelling-wave electrode structure for integrated electro-optic modulators, taking into account of the velocity mismatch that may cancel the phase shift of the modulation as well as choose the optimum design of the electrode structure in order to get the maximum available modulation performance of the modulators.

3.2 The Choice of the Electrode Structure Configuration

The purpose of the electrodes in modulators is to apply a electrical modulating signal field to a optical waveguide crystal which has a relatively strong electro-optic coefficient, such as $LiNbO_3$ ($r_{33} = 30.8\times10^{-12}$ m/v, $n_e r_{33} = 328\times10^{-12}$ m/v) and GaAs ($r_{41} = 1.6\times10^{-12}$ m/v, $n_o r_{41} = 59\times10^{-12}$ m/v). Actually, the function of the electrodes is the extension of the microwave transmission line which modulates the optical signal in the waveguide, the main point for designing electrodes is to concentrate the electrical field in the optical guiding area as much as possible.

There are two kind of electrode structures available for integrated optical modulators; one is the the lumped electrode structure of which the length of the electrodes is small compared to the wavelength of the modulation signal, and the other is the microwave travelling-wave structure which makes the broad bandwidth modulation available as the electrical signal is "chasing" the optical wave. First, let's take a look at the lumped electrode structure.

The lumped electrode structure (shown as Fig. 3.1) can be treated electrically as a static capacitor with a local charging resistor, and its bandwidth is limited by the time constant related to the individual elements of the structure, strictly speaking, it is limited by the RC time constant. Moreover, it is very difficult to match a lumped electrode structure to the driving RF signal because of the impedance difference. By conclusion, the lumped electrode structure is not suitable for high rates, broad bandwidth integrated optical modulators.

By comparison, the travelling wave structure (shown in Fig. 3.2) causes quite satisfactory results in modulation bandwidth. As the aim of the travelling wave structure is to make the electrodes appear as the

continuation of the RF generator and the feeding coaxial line, it is easy for the electrodes to be matched with them since the input impedance of travelling wave electrodes depends on the physical dimension of the electrode structure. So, this means that the modulation bandwidth of the travelling wave electrodes is only limited by the velocity mismatch arising between the optical and electrical signals.

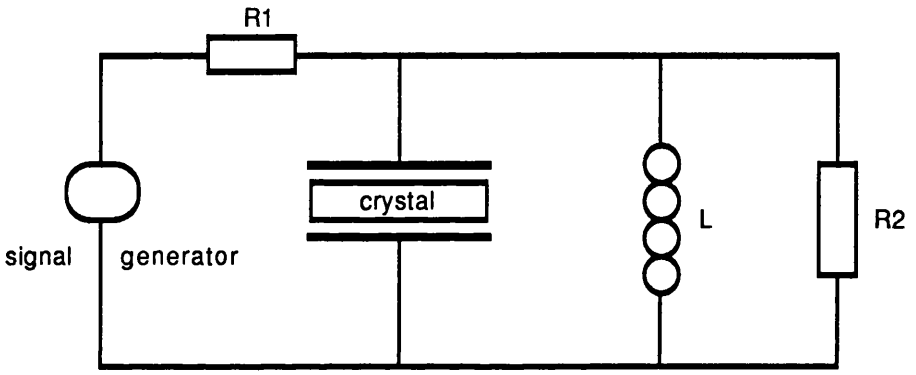

Fig. 3.1 The lumped electrode structure

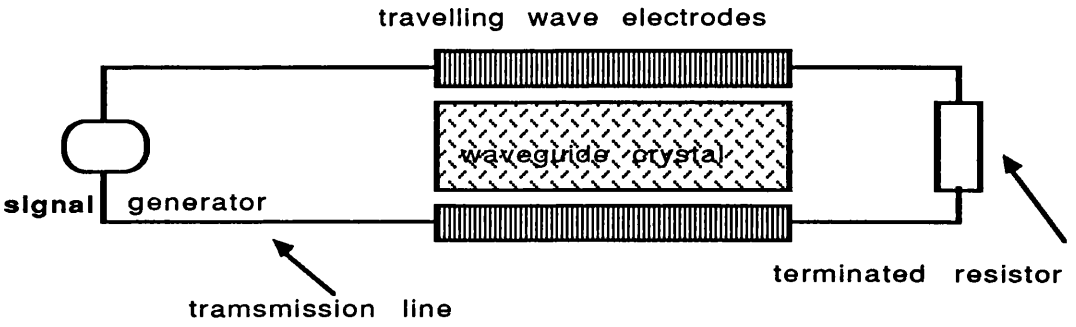

Fig. 3.2 The travelling-wave electrode structure

Having established that the most suitable electrode structure is the travelling-wave electrodes, we still need to choose the configuration

which allows a wide modulation bandwidth and a good frequency response characteristics. Also, we have two type of travelling-wave coplanar electrode structures to use for buried optical waveguide devices, namely symmetric coplanar structure which consists of two narrow parallel electrodes shown in Fig. 3.3 (a), and asymmetric coplanar structure which is composed of a narrow strip electrode (width w and separation s) and a half-plane ground electrode that the edge is parallel to the strip one (shown in Fig. 3.3 (b)) [5].

For the symmetric electrode structure, unfortunately, the modulation bandwidth is narrower than that of asymmetric structure and the modulation frequency response is not smooth, despite the characteristic impedance of the electrodes 50 ohm and matched to feeding transmission line, and the poor performance is believed to be caused by large discontinuity of the input and output circuits. Since the electrodes are used to function as the extension of the transmission line in the microwave travelling wave operation, the symmetric electrode structure is not suitable for broad bandwidth modulation [5].

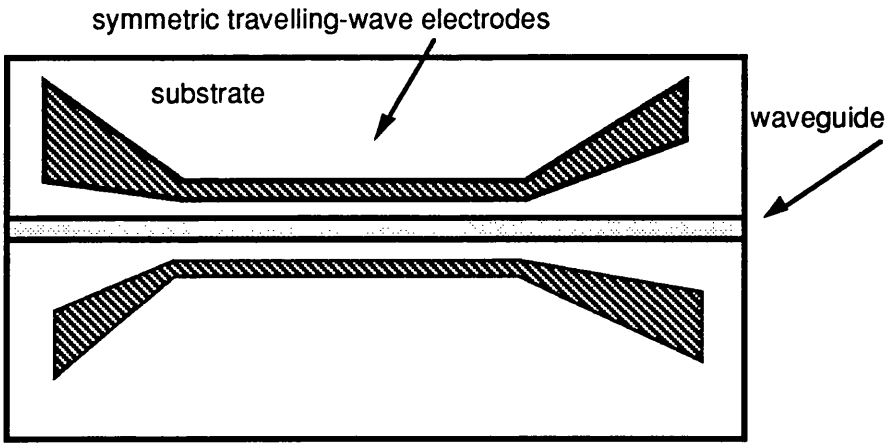

Fig. 3.3 (a) symmetric travelling-wave electrode structure

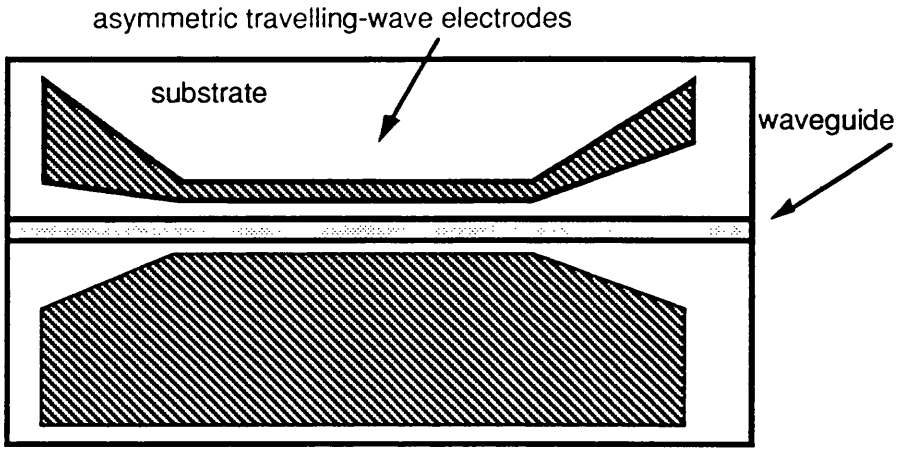

Fig. 3.3 (b) asymmetric travelling-wave electrode structure

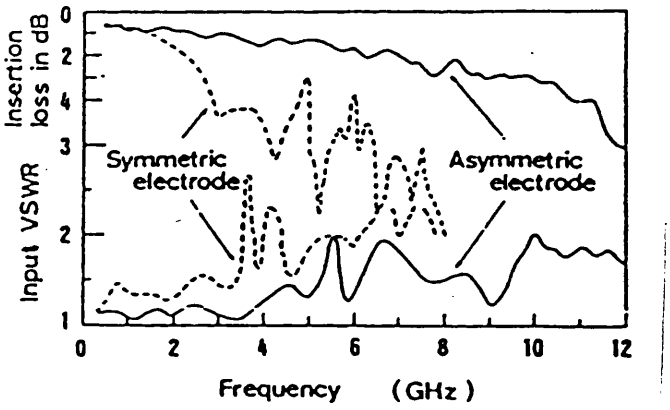

Fig. 3.4 Measured insertion loss and input VSWR for the travelling wave modulator using symmetric and asymmetric electrodes (ref. 5)

Fortunately, the asymmetric electrode structure has rather good results and gets rid of the spurs on frequency response which is caused in the symmetric electrode structure. Also, the insertion losses and VSWR (voltage standing-wave ratio) gets improved compared with the

symmetric one. In Fig. 3.4, it shows the insertion losses and the input VSWR vs the modulation frequency as the electrode length and separation are almost the same in both cases. Therefore, the asymmetric coplanar travelling-wave electrode structure is suitable for high rate, broad bandwidth integrated optical modulators.

3.3 Analysis Of Asymmetric Coplanar Travelling Wave Electrode Structure

In order to design a good coplanar electrode structure for the modulators, the main elements are the static capacitance which leads to the characteristic impedance, the electrical field distribution overlapping with the guiding optical wave and the electrical losses which may occur in the electrodes. In order to ease the design of the electrode structure, we use the Schwarz-Christoffl transformation [6] which transform the shape of the electrode structure from the Z (x, y) plane into the W (u, v) plane so that we can the results that the the geometry and boundary condition of the device are transformed from two coplanar parallel lines in Z (x, y) into a simple two plate capacitor configuration in the W (u, v) plane. The advantage of this method is that we can calculate the parameters of the electrodes directly and easily.

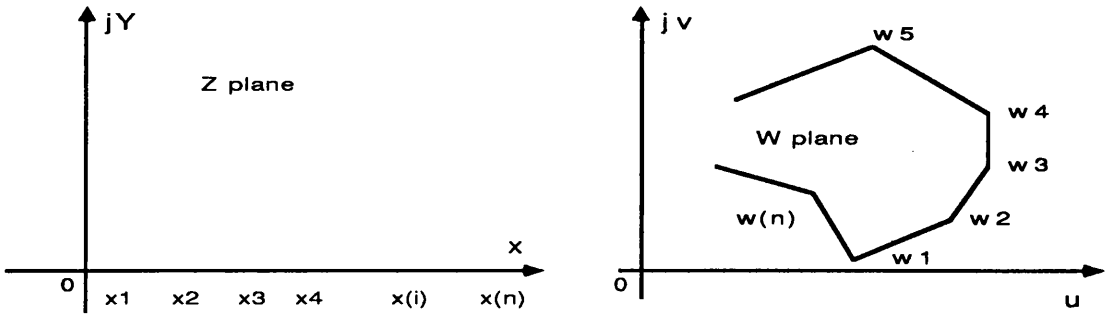

Fig. 3.5. The Schwarz-Christoffel transformatiom from up half plane in Z plane into the interior of a polygen in W plane

The Schwarz-Christoffl transformation is a conformal transformation which will map the real axis in Z plane into a general ploygen in the W plane with the upper half plane mapping into the region interior to the ploygon as illustrated in Fig. 3.5.

From Collin's derivation [6], we get the capacitance of the electrodes as;

$$C = \varepsilon_0 \varepsilon_{r,\,eff.} \frac{K(k')}{K(k)} \qquad (3-1)$$

$$K = \left(1 + \frac{W}{G}\right)^{-\frac{1}{2}} \qquad K' = \sqrt{1 - K^2}$$

$$\varepsilon_{r,\,eff} = \frac{1}{2}\left[1 + \sqrt{\varepsilon_{r,\,x} \times \varepsilon_{r,\,y}}\right]$$

where the $\varepsilon_{r,\,x}$ and $\varepsilon_{r,\,y}$ are the dielectric constants along the x, y axis. K(k) given in above equation is called the complete elliptic integral of the first kind.

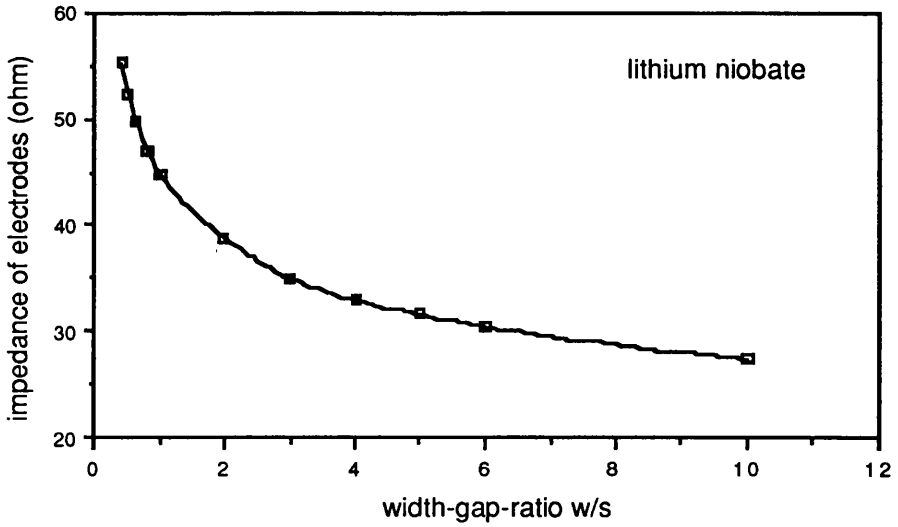

Fig. 3.6 (a) impedance of the electrode on lithium niobate vs w/s

The characteristic impedance of the electrodes is

$$Z_C = \frac{1}{cn_mC} \qquad (3-2)$$

where c is the light speed in vacuum and n_m is the index "seen" by microwave which is 4.2 for $LiNbO_3$ [3]. The curves of the characteristic impedance for asymmetric coplanar electrodes vs the the width-to-gap ratio of the electrodes for lithium niobate is plotted in Fig. 3.6, so we can design the electrodes which have the characteristic impedance expected by choosing proper ratio of width to gap. We notice that the width-to-gap ratio is 0.62 for 50 Ω impedance on lithium niobate substrate.

3.4 The Electro-Optic Control of The Optical Wave

As we want to concentrate the electric field as much in the optical guiding area as possible, the distribution of the field around the optical waveguide is very important for getting the optimum overlap between the electric filed and optical field to get the maximum available modulation efficiency [7], [8], [9].

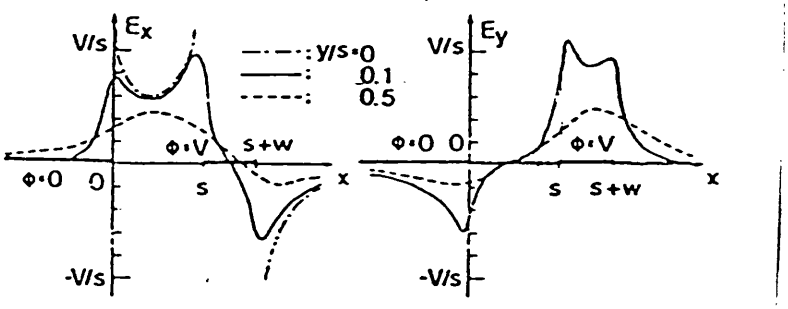

Fig. 3.7 The electric field distribution between the electrodes both for X- and Y-direction (ref. 5)

From Izutsu and Sueta's results [5], the distribution of the electric field both x and y directions is shown in Fig. 3.7, and it also indicates that when width of the conducting electrode varies slightly compared to the separation gap of the electrodes, the electric field components both E_x in the middle of the electrodes and E_y underneath the electrodes are almost unchanged.

From Fig. 3.7, we find that for TE mode, the electric field near the edges of the electrodes is rather strong and the gradient of the field is quite large along the gap, however, the field is respectively flat in the middle of the gap. Therefore, it is better to put the optical waveguide in the middle of the electrodes avoiding the peak gradient of the electric field that means the gap of the electrodes is a little bit wider than the width of the optical waveguide. Also, this makes it easy to deposit the electrodes upon the waveguide as it is very difficult to align the same width of the gap along the waveguide without covering the waveguide with the electrodes which would cause extra optical loss in the waveguide. But this decreases the overlap integral between the electric and optical fields which will influence the electrical driving power as the driving voltage can be get from following equation [3].

$$\Delta n(V) = -\frac{n^3 r V \Gamma}{2G} \qquad (3-3)$$

where $\Delta n(V)$ is the induced index change, n is the optical index of the waveguide, r the relatively electro-optic coefficient of the crystal and Γ the overlap integral between the electric field and optical mode in the waveguide which is defined as

$$\Gamma = \int\int E|E|^2 \, dA \qquad (3-4)$$

where E' is the normalised optical field and E the normalised electric field, the total phase shift through the interaction length of the electrodes L_E is then

$$\Delta\beta L_E = -\frac{\pi n^3 V L_E \Gamma}{G\lambda} \qquad (3-5)$$

where λ is the optical wavelength of the light travelling in the waveguide and β is the wave vector. The exact phase shift required to achieve the complete intensity modulation depends on the type of the modulators, in Mach-Zehnder modulator, the phase shift required in each arm is $\pi/2$ and the total phase shift is π, while for Fabry-Perot modulator is only $\pi/2$, so we obtain the results as following

$$|\Delta\beta L_E| = \frac{1}{2}m\pi \quad (\ m=1 \text{ for FP},\ m=2 \text{ for MZ}\ ) \qquad (3-6)$$

So, the voltage-length product required for complete modulation is thus

$$V L_E = \frac{m\lambda G}{r n^3 \Gamma} \qquad (3-7)$$

The goal of the modulator design is to get broad modulation bandwidth and low driving voltage, and we will show latey that the maximum available bandwidth also scale nearly $1/L_E$. Therefore, for a given electro-optic material and wavelength, we want to minimise VL_E product by reducing the geometric parameter G/W, (W is the width of the mode profile of the waveguide) but it conflicts with the requirement of the uniform electric field and fabrication tolerance. So the only way we

can do is to trade off each parameter according to the driving power or modulation bandwidth requirement of the modulator.

3.5 Velocity Mismatch and Modulation Bandwidth In The Modulators

The velocity mismatch between the optical signal and electrical signal is caused by the different index "seen" by each signal ($n_0 = 2.2$, $n_m = 4.2$ for $LiNbO_3$). Because of the different index, they travel at different velocity in the substrate. Therefore, some of the phase shift would be cancelled by the velocity mismatch at very high frequency and the modulation efficiency gets degraded. This configuration corresponds to a travelling wave modulator in the case that the phase velocity of the electromagnetic wave ($V_{elec.} = C_0 / \varepsilon_{r,\,eff.}^{1/2}$) is not matched to that of the optical wave ($V_{opt.} = C_0 / n_{eff.}$) in the optical waveguide modulators because $n_{eff.} < \varepsilon_{r,\,eff.}^{1/2}$ for $LiNbO_3$.

The electrodes here assumed to be designed as matched transmission lines with a characteristic impedance of Z_0 (normally 50 ohm) and also to be terminated by a resistor of Z_0 in order to realise the largest transmission. The modulation bandwidth is limited by the transit time difference between the electromagnetic wave and optical wave. If the cut-off frequency is defined as 3-dB bandwidth frequency at which the modulation efficiency is $1/\sqrt{2}$ relative to f = 0. The relation between the cut-off frequency and the length of the electrodes is very complicated, however, in the case of electric lossless condition, the relation can be approximately simplified as [7], [10]

$$L_E f_{max} = \frac{1.39 C_0}{\pi \left| n_{eff.} + (\varepsilon_{r,\,eff.})^{1/2} \right|} \quad (\text{GHz*mm}) \qquad (3-8)$$

For $LiNbO_3$ substrate, the typical value of the length-bandwidth product will be 65 GHz mm. In order to get large bandwidth, we can shorten the length of the electrodes, however, it will increases the electrical driving power on scale of $1/L_E$ from above equation. Furthermore, the methods to increase the length-bandwidth product have been widely investigated. Erasme and Wilson [11], Alferness [12], and Nazarathy [13] used the periodic and non-periodic phase reversal electrodes to increase the length-bandwidth product to get the broad bandwidth modulation before the microwave discontinuity becomes significant; Haga [23] increased the modulation bandwidth by etching a groove between the optical waveguide arms and also reduce the electrical driving power by reducing the separation of the two waveguides; Furthermore, Atsuki [24] proposed the a two layer travelling wave electro-optical modulator structure to maximise the modulation bandwidth up to 450 GHz×mm.

3.6 The Electrical Losses in the Electrodes

The electrical losses in the electrodes are also very important for the integrated optical modulator as they increase the electrical driving power, reduce the modulation efficiency and effect on the available modulation bandwidth. Theoretically, there are three major mechanisms which contribute to the electrical losses in the electrodes, namely conducting loss, dielectric loss and mismatch losses at the connection, such as the mismatch of the coaxial feeding line to the electrodes, as well as the electrodes to the termination resistor [19],[20],[21],[22].

First, Let's consider the conducting loss in the electrodes due to the finite conductivity of the material from which the electrodes were fabricated and this leads a finite resistance to the electrodes. We assume that the attenuation affects the modulation power along the electrodes in

manner of exp (-αl), and the loss is only caused by conducting electrode as the ground electrode is considered as an "infinite half-plane" for the asymmetric electrodes structure. Obviously, the electrical losses clearly have a degrading effect on the performance of the modulation. In order to minimise the conducting loss in the electrodes, we need to select the materials which have low resistivity such as Gold (conductivity $\sigma=4.25\times10^{-7}$ mho/meter) and Aluminum (conductivity $\sigma=3.50\times10^{-7}$ mho/meter).

As the frequency of the signal travelling through the electrodes increases, the current is restricted to flow in the region closing to the conductor surface layer by electromagnetic induction inside the conductor. The tendency for the current to flow only near the surface or "skin" of the conductor is called as "skin effect". The penetration depth of the current into the conductor is known as the skin depth and itself is a frequency-dependent effect. The skin depth is defined as the thickness of the layer within which the current density drops off to the value of 1/e of the initial value. As the frequency of the signal increases, the confinement of the current within the conductor become much more narrow; and at very high frequency, it gets confined within a very small fraction of the thickness of the conductor itself. Therefore, the skin depth at different frequency needs to be taken into account when considering losses which occur in the electrodes.

The skin depth d is given by as following;

$$d = \sqrt{\frac{\rho}{\pi \mu f}} \quad \text{(meter)} \qquad (3-9)$$

where ρ is the resistivity of the conductor, u is the permeability, f is the frequency of the modulation signal.

When the skin depth is greater than half thickness of the electrodes, we make the approximation that the skin depth is equal to the half thickness of the electrodes, for the purpose of calculating the loss which arrives in the conducting electrode. At very high frequency, however, this approximation becomes unrealistic since the skin depth decreases to a much small fraction of the electrode thickness. In that case, we need to calculate the actual value of the skin depth in the electrode through which the current can be considered to be flowing.

We can calculate the actual conducting loss coefficient for the electrodes by considering the average power losses in the electrodes per unit length and the total power flowing. the value for the attenuation coefficient α is given as following;

$$\alpha = \frac{\text{average power dissipated}}{\text{average flowing power}} = \frac{W_d}{W_t} \qquad (3-10)$$

the value of W_t is easily achieved from $W_t = V_o^2/2Z$ where V_o is the peak voltage of the modulation signal and Z is the impedance of the electrodes. We can get the approximation of the loss coefficient for the asymmetric coplanar strip line with the thickness of τ as below [20];

$$\alpha = \begin{cases} \dfrac{\rho}{2Zwd} & \text{for } d < 0.5\,\tau \\ \dfrac{\rho}{Zw\tau} & \text{for } d > 0.5\,\tau \end{cases} \qquad (3-11)$$

From above results, we can see that we should use as wide a conducting electrode as possible if we want to minimise the loss coefficient of the electrodes. However, the condition for matching the

electrodes to the 50Ω impedance feeding line requires a with-to-gap ratio of 0.62 on lithium niobate substrate. Moreover, in order to apply the electrical field across the optical waveguide in an efficient manner, we want the electrodes to be closed as much together as possible. Therefore, if we want to maximise the given electro-optic effect for the given applied voltage, we will have a large conducting loss if we operate the electrodes as the matching condition between the feeding line and the electrodes as well as the terminating resistor.

From previous conclusion, we knew that the effect of the slight mismatching of the the electrodes to the source had little influence on the field strength and distribution between the electrodes. Therefore, as we want to maximise the electro-optic effect for a given applied voltage, we will have a large conducting loss if we operate the electrodes at the matching condition. As the effect of the mismatch between the electrodes and the driving source had little influence on the field strength and the distribution between the electrodes. Therefore, we can improve the modulator performance by increasing the width of the conducting electrode if the loss introduced by the mismatch is small enough not to degrade the characteristic of the electrodes.

When the width of the conducting electrode got increased for a fixed electrodes gap, we have the width-to-gap ratio changed from 0.62, and also other parameters arising from Schwartz-Christoffel transformation changed. Using these new parameters, we can gain the new impedance of the electrodes, so we find that the loss introduced by the mismatch as following;

$$\text{Mismatch Loss} = -10\log_{10}(1 - R^2)$$

$$R = \frac{Z_E - Z_C}{Z_E + Z_C} \qquad (3-12)$$

where R is called the reflection coefficient of the travelling wave wave signal, Z_E is the impedance of the electrodes and Z_C is the impedance of the driving source. The total losses of electrodes, the mismatch loss and conducting loss versus the impedance of the electrodes is plotted in Fig. 3.8. By this relationship, It can be seen that if we reduce the impedance to by increasing the width of the conducting electrodes, the conducting loss of the electrodes is reduced with only little extra mismatching loss introduced to the electrodes. Therefore, the total electrodes losses can be reduced by increasing the width of the conducting electrode. Furthermore, we can use the impedance transmission tapers to reduce the mismatch losses (or reflection) between the driving source and the electrodes as well as the termination resistor even further.

In addition to conducting loss and mismatch loss, there is also a contribution from a dielectric loss. However, from Pucel et al [20] and Wheeler et al's [21] results, the dielectric loss is very small in comparison to the conducting loss and mismatching match, so the dielectric loss have been regarded as negligible, especially for lithium niobate.

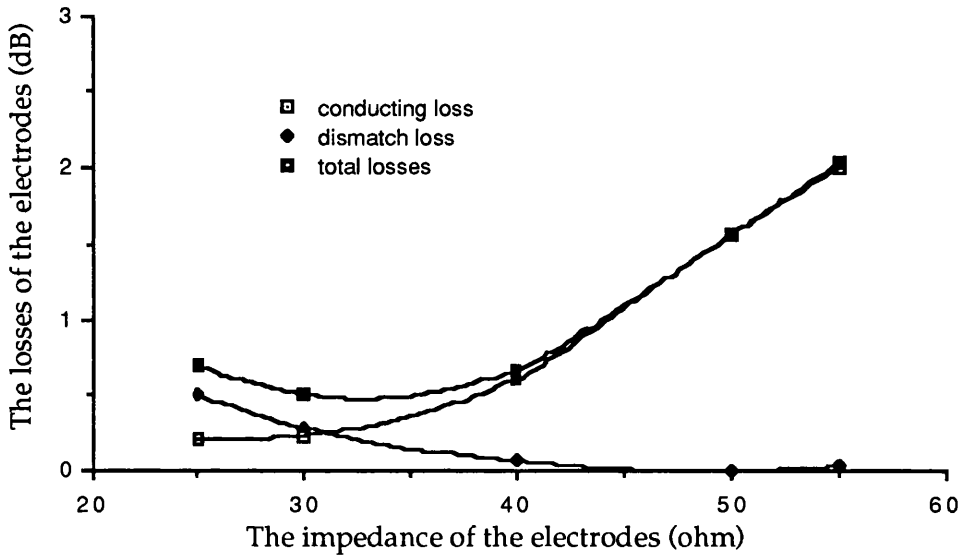

Fig. 3.8 The losses of the electrodes vs the electrode impedance

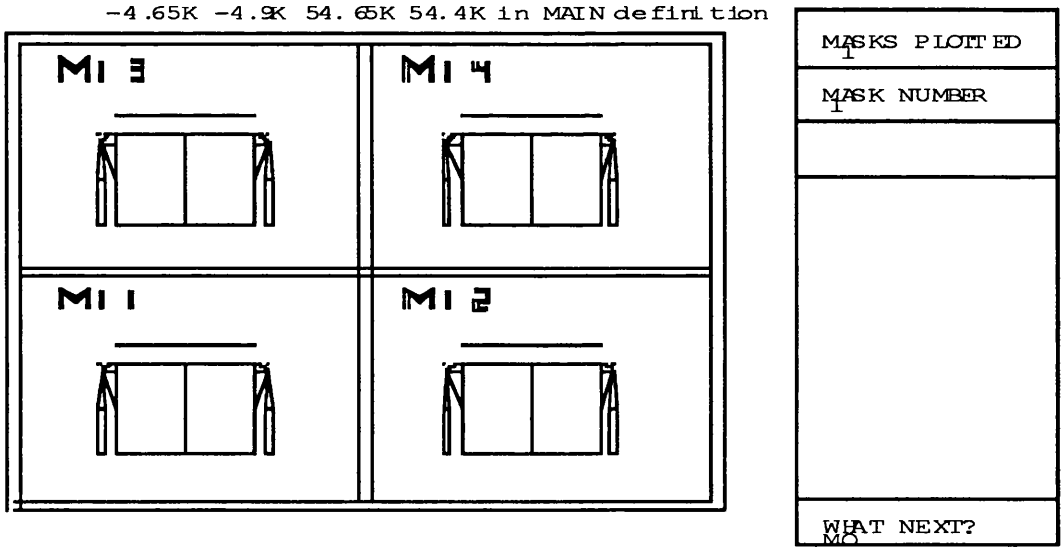

Fig.3.9 (a) The travelling-wave electrode structure of 10 mm long conducting electrode and 8 μm gap

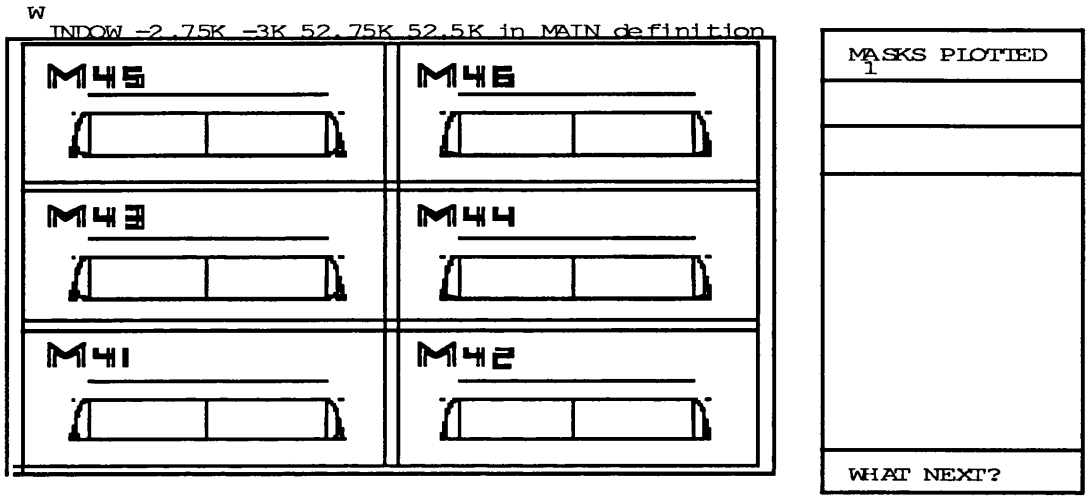

Fig. 3.9 (d) travelling wave electrode structure for 16 mm long

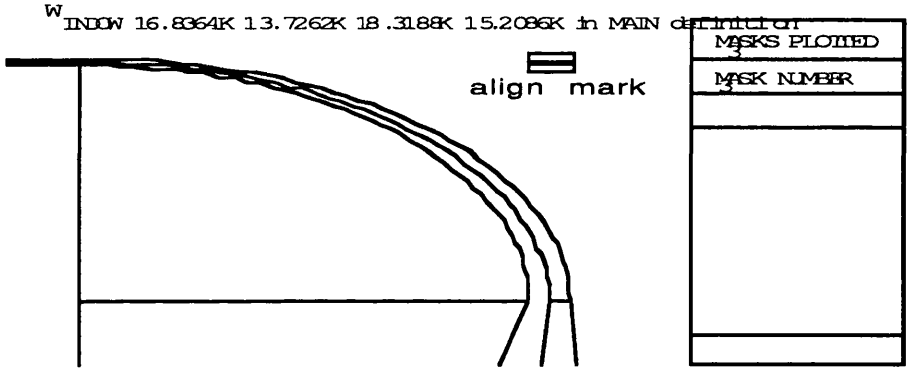

Fig. 3.9 (e) The taper of the travelling electrode structure to change the direction and reduce the losses of the electrodes

3.7 Electrodes Design and Structure

In designing the electrode structure masks, we use the computer language called GAELIC which is a written language providing a simple way of defining two dimensional geometrical shapes to make the masks form the expected patters on the substrate by photolithography. For high speed integrated optical modulators, we use the travelling-wave electrodes to get broad bandwidth modulation. For different dimensions

of the waveguide and alignment, we design 18 electrodes with different interaction length, width of the conducting electrode and gap-width-ratio shown in Fig. 3.10 (a), (b). The parameters are displayed in table 2. In order to get good connection between the electrodes and the microwave transmission line, we introduce the trans-impedance tapers at the ends of the electrodes which changes the impedance gradually shown in Fig. 3.10 (a), (b) and the turning taper shown in Fig. 3.10 (c).

3.8 Fabrication of The Electrodes on $LiNbO_3$ Substrate

The fabrication of the travelling-wave electrodes for the integrated optical modulator has been done in the Clean Room just like the fabrication of optical waveguides. In practice, there are two standard methods to fabricate the electrodes, one is called lift-off method, the other is called etching method. For the lift-off method, it gives a very good definition of the pattern shape, but it is quit difficult to make good alignment between the waveguide and electrodes after spinning a layer of photoreist on the lithium niobate substrate, especially for deeply indiffused waveguides, as the waveguide pattern can not be seen clearly through a microscope; while the etching method can make the alignment much easier as the photolithography is after the depositing of a thin layer of Cr-Au coating which is very sensitive to the small variation of the refractive index, however, the lateral etching of the pattern definition makes the width and the ratio of the width to gap of the electrodes very difficult to control.

In order to obtain the good performance of the modulators, we prefer the deep diffused, low loss optical waveguides. As the index difference between the guiding area and the substrate at the surface is very small, it makes the alignment along the waveguide impossible by lift-off method since we almost cannot see the image of the waveguide

through microscope after putting the photoresist on it. Therefore, a new method of electrodes fabrication is presented which is called " Etched-Lift-Off" method as it is the mixture of both etching method and lift-off method. The procedure is as following; First, deposit a 20 nm thin layer of Cr on the $LiNbO_3$ substrate to make the image of the waveguide clear to make the good alignment; Then use the standard lift-off method to describe the electrodes pattern by deposit further 20 nm Cr thin film plus hundreds nm Au, then remove the unwanted parts of Cr-Au coverage; Finally, etch off the unwanted Cr thin film, and we can obtain the desired electrodes, of which the whole procedure is shown in Fig. 3.11. Sometimes, we increase the thickness of the electrode up to 2 - 3 μm by electrical plating further Gold.

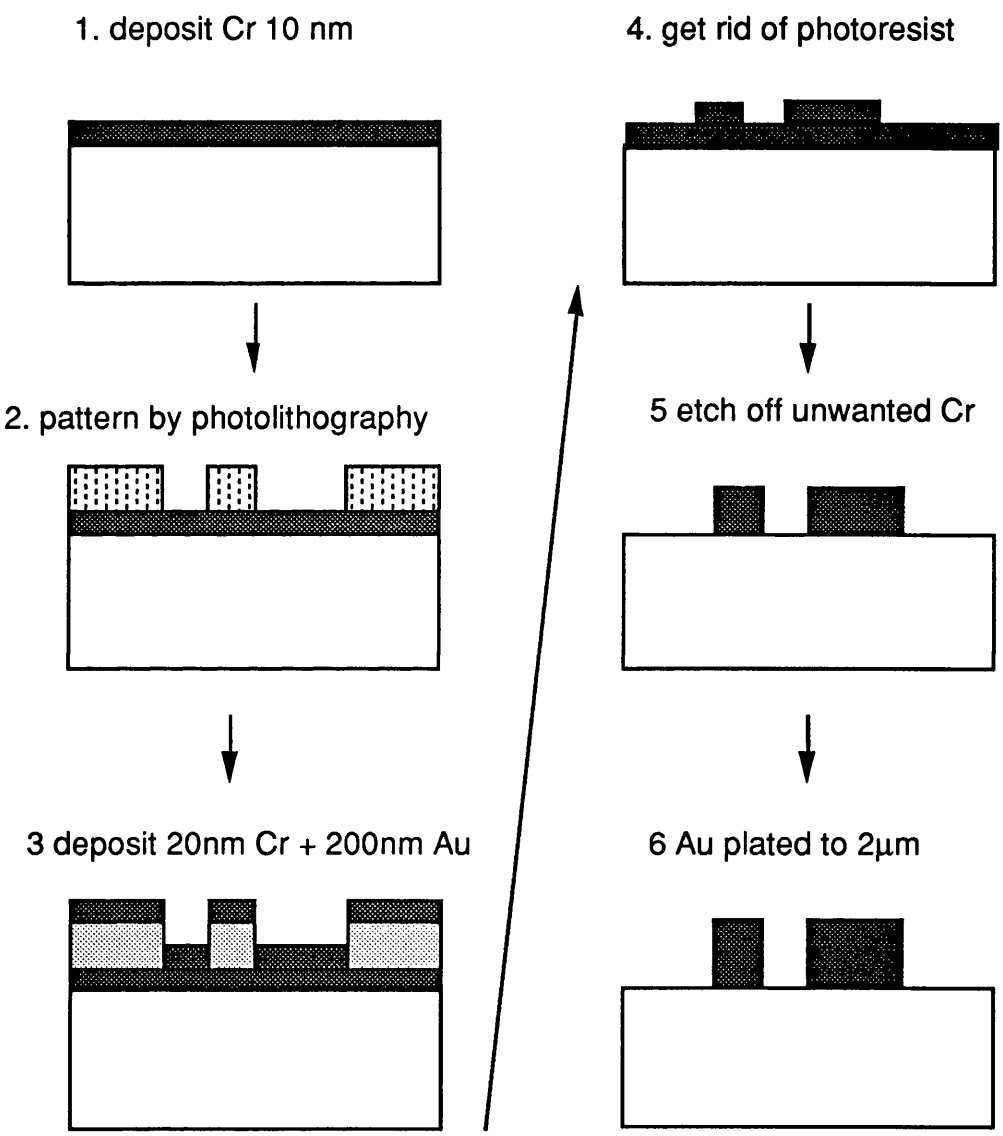

Fig. 3.10 Procedure for electrodes fabrication by the new etching-lift-off method

TABLE 2

dimension parameters of travelling-wave electrode structure

	Length	Gap	Width	W/G	Imped.	Dimens.
M 11	10 mm	8 micro	8 micro	1	44.9 ohm	15*11mm
M 12	10 mm	8 micro	16 micro	2	38.9 ohm	15*11mm
M 13	10 mm	8 micro	40 micro	5	31.6 0hm	15*11mm
M 14	10 mm	8 micro	64 micro	8	28.7 ohm	15*11mm
M 21	10 mm	10 micro	10 micro	1	44.9 ohm	15*11mm
M 22	10 mm	10 micro	20 micro	2	38.9 ohm	15*11mm
M 23	10 mm	10 micro	50 micro	5	31.6 ohm	15*11mm
M 24	10 mm	10 micro	80 micro	8	28.7 ohm	15*11mm
M 31	10 mm	15 micro	15 micro	1	44.9 ohm	15*11mm
M 32	10 mm	15 micro	30 micro	2	38.9 ohm	15*11mm
M 33	10 mm	15 micro	75 micro	5	31.6 ohm	15*11mm
M 34	10 mm	15 micro	120 micro	8	28.7 ohm	15*11mm
M 41	16 mm	8 micro	8 micro	1	44.9 ohm	20*6 mm
M 42	16 mm	8 micro	40 micro	5	31.6 ohm	20*6 mm
M 43	16 mm	10 micro	10 micro	1	44.9 ohm	20*6 mm
M 44	16 mm	10 micro	50 micro	5	31.6 ohm	20*6 mm
M 45	16 mm	15 micro	15 micro	1	44.9 ohm	20*6 mm
M 46	16 mm	15 micro	75 micro	5	31.6 ohm	20*6 mm

3.9 Reference

[1]. T. Kimura, " Coherent optical fibre transmission ", J. Lightwave Tech., Vol. LT-5, No. 4, pp-414, April, 1987.

[2]. C. M. Gee, G. D. Thurmond and H. W. Yen, " Travelling-wave electro-optic modulator ", Applied Optics, Vol. 22, No. 13, pp-2034, April, 1983.

[3]. R. Alferness, " Waveguide electro-optic modulator ", IEEE Trans. on Microwave Theory and Tech., Vol. MIT-30, No. 8, pp-1121, August, 1982.

[4]. C. H. Chen and T. Findakly, " Integrated optic modulators - a review and an assessment ", SPIE Vol. 139, Guided wave optical system and devices, 1978

[5]. M. Izutsu and T. Sueta, " Broad-band guided-wave light intensity modulator ", Electronics and Communication in Japan, Vol. 60-c, No. 4, pp-107, 1981.

[6]. R. E. Collin, " Field Theory of Guided Wave ", Chapter 4, McGraw-Hill; New York, 1960.

[7]. F. Auracher and R. Kell, " Design consideration and performance of Mach-Zehnder waveguide modulators ", Wave Electronics, 4, pp-107, 1981.

[8]. D. Marcuse, " Optimal electrodes design for integrated optical modulators ", IEEE, J. Quantum Electronics, Vol. QE-18, No. 3, pp-

393, March, 1982.

[9]. O. G. Ramer, " Integrated optic electro-optic modulator electrodes analysis ", IEEE, J. Quantum Electronics, Vol. QE-18, No. 3, pp-386, March, 1982.

[10]. R. E. Becker, " Travelling-wave electro-optic modulator with maximum bandwidth-length product ", Applied Physic. Lett., Vol. 45, No. 11, pp-1168, Dec. 1984.

[11]. E. Eraseme ans M. G. F. Wilson, " Analysis and optimation of integrated-optic travelling wave modulators using periodic and non-periodic phase reversals ", Optical and Quantum Electronics, 18, pp-203, 1986.

[12]. R. Alferness, S. Korotky and E. A. J. Marcatili, "Velocity-matching technique for integrated optic travelling wave switch/modulators ", IEEE J. Quantum Electronics, Vol. QE-20, No. 3, PP-301, March, 1984.

[13]. M. Nazarathy and D. W. Dolfi, " Velocity-mismatch compensation in travelling wave modulators using pseudorandom switched electrode patterns ", J. Optical Soc. Aman. Vol. 4, No. 6, pp-1071, June 1987.

[14]. I. P. Kaminow and E. H. Turner, " Electro-optic light modulators ", Proceeding of the IEEE, Vol. 54, No. 10, pp-1374, October, 1966.

[15]. I. P. Kaminow, L. W. Stulz and E. H. Turner, " Efficient strip waveguide modulator ", Applied Physics Letters, Vol. 27, No. 10, pp-555, November 1975.

[16]. M. Papuchon, Y. Combemale, X. Mathieu, D. B. Ostrowsky, L. Reiber, A. M. Roy, B. Sejourne and M. Werner, " Electrically switched optical directional coupler: Cobra ", Applied Physics Letters, Vol. 27, No. 5, pp-289, September, 1975.

[17]. H. W. Yen C. M. Gee and H. Blauvell, "High-speed optical modulation techniques", SPIE Optical Technology for Microwave Applications, Vol.545, pp-2,195.

[18]. K. Kubota, J. Noda and O. Mikami, " Travelling wave optical modulator using a directional coupler $LiNbO_3$ waveguide ", IEEE J. Qutantum Electronics, Vol. QE-16, No. 7, pp-754, July 1980.

[19] J. P. Becker and D. Jager, "Electrcal properties of coplanar transmission lines on lossless and lossy substrate", Electronics Letters, pp-92, Jan. 1979.

[20] R. T. Pucel, D. J. Masse and C. P. Hartwig, " Losses in Microstrip", IEEE Trans. on micriwave Theory and Technology, MIT-16, No.6, pp-342, June, 1968.

[21] H. A. Wheeler, "Transmission line properties of parallel strip separated by a dielectric sheet", IEEE Trans. on Microwave Theory and Technology, pp-172, March, 1965.

[22] R. E. Colin, Fundations for Microwave Engineering", Chapter 4, McGraw-Hill, New York, 1966.

[23] H.Haga, M. Izutsu and T. Sueta, "LiNbO travelling-wave light modulator/switch with an etched groove", IEEE Quantum Electronics, Vol. QE-22, No. 6, pp-902, June 1986.

[24] K. Atsuki and E. Yamashita, "Transmission line aspect of the design of broad band electro-optic travelling-wave modulator", J. Lightwave Technology, Vol. LT-5, No. 3, pp-316, March, 1987.

CHAPTER 4 DESIGN AND DEPOSITION OF HIGHLY REFLECTIVE COATING

4.1 Introduction

For the Fabry-Perot integrated optical modulator, the highly reflective coatings at the two ends of the device are very crucial and they play a rather important role at the performance of the modulator, e.g. the optical losses, electrical driving power and modulation bandwidth. In general, there are two sorts of high reflective optical coating available, one is a metal thin film coating, and the other is a multilayer dielectric coating. For a metal thin film, because it is single layer coating, it is easy to fabricate with large fabrication tolerance on thickness monitoring and large bandwidth of high optical reflective zone from visible until far-infrared range. Therefore, it finds a lot of applications in applied optics. However, it is difficult to have the reflectivity over 95% and the transmission is very lossy which depends on the thickness of the metal film and the operating wavelength [1], especially in visible and near-infrared range, so it is unsuitable for some high performance applications. By comparison, the multilayer dielectric coating is much more attractive than the metal film in high performance applications because it can reach extremely high reflectivity which is nearly 100%, and possibly very low losses in transmission which is only around 0.1% with extra care, although the multi-layer design is complicated to fabricate for large bandwidths, and a complex phase shift is introduced upon reflection. On the whole, a multilayer dielectric coating is very suitable for the Fabry-Perot integrated optical modulator on the ground of the low transmission loss.

4.2 The Principle of Multilayer Dielectric Coating

The basic principle of the high reflective multilayer dielectric coating is based on the optical interference theory. For the most cases, we use the simplest kind of periodic system, called the quarter-wave stack, which is composed of a number of quarter wave layers and the periodic structure of alternately high- and low-index materials, which is illustrated in Fig. 4.1.

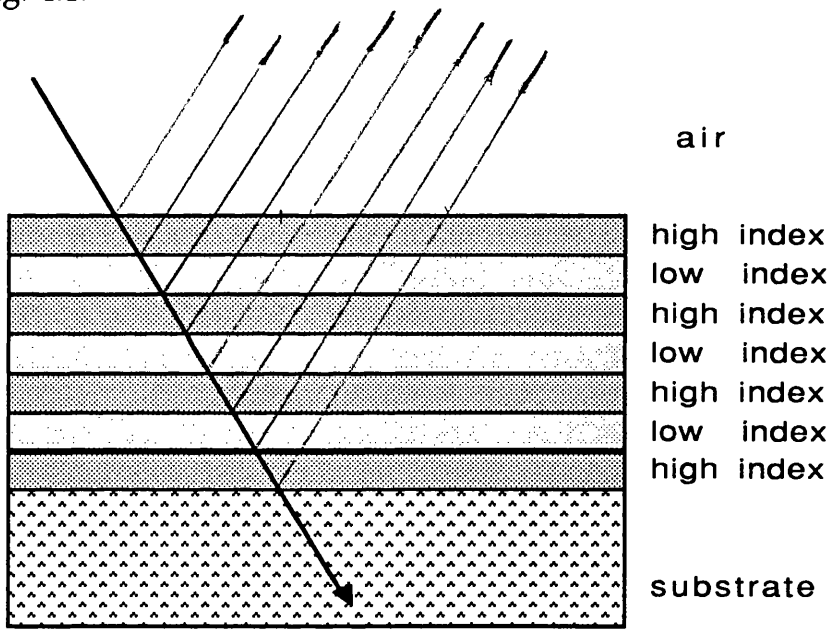

Fig. 4.1 the structure of quarter-wave stack for high reflective dielectric coating

From Maxwell equations and the boundary conditions, we can get the transformation matrix as following [2]:

$$\begin{bmatrix} E_1 \\ H_1 \end{bmatrix} = \mu_1\mu_2 \cdots \mu_n \begin{bmatrix} E_{p+1} \\ H_{p+1} \end{bmatrix} \qquad (4-1)$$

where E_1 and H_1 are the electric field and magnetic field at first layer, E_{p+1} and H_{p+1} at the last layer, μ_i is the characteristic matrix of the individual layer, which is defined as following:

$$\mu_i = \begin{bmatrix} \cos k_0 h & (j \sin k_0 h)/\gamma_i \\ \gamma_i j \sin k_0 h & \cos k_0 h \end{bmatrix} \qquad (4-2)$$

where k_0 is the wave vector, γ_i is the incidence condition coefficient, defined as :

$$\gamma_i = \sqrt{\frac{\varepsilon_0}{\mu_0}}\, n_i \cos\theta_i \quad \text{for TE mode} \qquad (4-3)$$

$$\gamma_i = \sqrt{\frac{\varepsilon_0}{\mu_0}}\, \frac{n_i}{\cos\theta_i} \quad \text{for TM mode} \qquad (4-4)$$

where n_i is the index of the ith layer and θ_i is the incidence angle of the ith layer. The characteristic matrix of the entire system is the result of the product of the individual characteristic matrix, that is,

$$\mu = \mu_1 \mu_2 \ldots \mu_n = \begin{bmatrix} m_{11} & m_{12} \\ m_{21} & m_{22} \end{bmatrix} \qquad (4-5)$$

For the simple quarter-wave stack multilayer high reflective coating, we gain the optical reflectivity as:

$$r = \frac{n_0 - \left(\frac{n_h}{n_l}\right)^{m-1} \frac{n_h^2}{n_s}}{n_0 + \left(\frac{n_h}{n_l}\right)^{m-1} \frac{n_h^2}{n_s}} \qquad \text{for odd-number layer} \qquad (4-6)$$

$$r = \frac{n_0 - \left(\frac{n_h}{n_l}\right)^{m-1} n_s}{n_0 + \left(\frac{n_h}{n_l}\right)^{m-1} n_s} \qquad \text{for even-number layer} \qquad (4-7)$$

where n_h and n_l are the high- and low-index of the coating materials, n_s and n_o are the index of the substrate and the index of environment (usually in air, $n_O = 1$), m is the number of the coating layers which is $m = 2p + 1$ for odd-number layers and $m = 2p$ for even-number layers.

From the above equations, we reach the conclusion that the greater the number of the layers, the larger are the reflectivity and the reflectance; the larger the difference of the high- and low-index in the alternative layers, the greater are the reflectivity and the reflectance of the coating for the same number of the coating layers. Moreover, the situation is quite different for odd number-layer coating and even number-layer coating. When the substrate index is high, we prefer even number-layer coating. Furthermore, the reflectivity of a few layers in even layer coating might be greater than that of significantly more layers in odd layer coating if the index of the substrate is greater than that of the high-index layers. On the another hand, we prefer odd number-layer coating when the substrate index is low, while the reflectivity of a few layers in odd number coating might be greater than that of significantly more layers in even number-layer coating when the index of the

substrate is less than that of the low-index layers. Therefore, in order to get the maximum available efficient coating, we choose the most suitable coating pattern for a given substrate material.

Besides, some other characteristics such as reflecting bandwidth (209) defined as the wavelength range at which the zone of the reflectivity drops to the 90% of the original one. For the reflecting bandwidth, according to the results given by H. A. Macleod [3], the reflecting bandwidth of the optical wavelength is decided by the difference between the low- and high-index materials in the stack, of which the greater the difference of the alternative indices, the larger the reflecting bandwidth. Therefore, we have;

$$\Delta g = \frac{2}{\pi} \sin\left(\frac{n_h - n_l}{n_h + n_l}\right) \qquad (4-8)$$

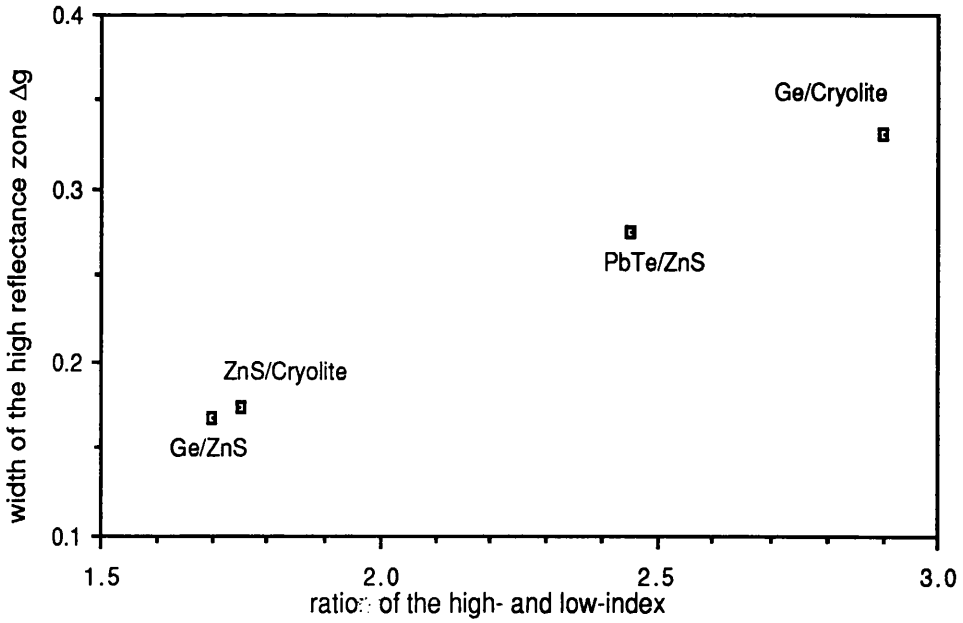

Fig. 4.2 the width of the high-reflectance zone of a quarter-wave stack plotted vs the ratio of the refractive indices

where $g = \lambda/\lambda_0$ and the width of the zone is $2\Delta g$. The above results show that the width of the zone is a function of the indices of the two alternative materials used in the construction of the multilayer. Fig. 4.2 gives the calculated Δg plot vs the ratio of the refractive indices in the coating.

4.3 Design of The High Reflective Dielectric Coating

For the high reflective dielectric coating, there are several kinds of alternative high- and low-index materials available, among them, Magnesium Fluoride (MgF_2), Silicon Dioxide (SiO_2) and Cryolite (Na_3AlF_6) are commonly used as low-index materials, while Titanium Dioxide (TiO_2) and Zinc Sulphide (ZnS) for high-index materials, at visible and near-infrared range. By comparison, we choose Cryolite and Zinc Sulphide as the low- and high-index materials due to their low price and easy operation.

As the indices of the materials are not commonly given at the wavelength at which the coating will be designed, the index at the wavelength needs to be calculated by the normal index dispersion formulate,

$$n(\lambda) = A + \frac{B}{\lambda^2} \qquad (4-9)$$

where A and B are the dispersion coefficients of the coating materials, and λ is the wavelength, so the thickness of the quarter-wave stack is,

$$\tau = \frac{\lambda}{4n(\lambda)} \qquad (4-10)$$

By calculation using above equations, we obtain the thickness of the each quarter-wave layer and the indices of the low- index material, Cryolite (Na_3AlF_6), and high-index material, Zinc Sulphide (ZnS), as well as the substrate index, at different wavelength.

For the high-index coating material Zinc Sulphide, we have the dispersion coefficients and the quarter-wave thickness for different wavelength as following;

ZnS A = 2.2188 B = 0.049

Wavelength (μm)	Index	Quarter-wave thickness (nm)
0.63	2.311	68.5
1.15	2.225	129.1
1.30	2.217	146.6
1.55	2.208	175.5

For low-index coating material Cryolite, we find;

Na_3AlF_6 A = 1.318 B = 0.0048

Wavelength (μm)	Index	Quarter-wave thickness
0.63	1.330	119.0
1.15	1.322	217.5
1.30	1.321	246.0
1.55	1.320	293.6

Therefore, the reflectivity and reflectance of the coatings, for different number of the layers on lithium niobate and glass slide substrate at the centre wavelength of 1.15 μm, can be calculated as

following;

For lithium niobate substrate

number of the layers	reflectivity	reflectance
3	0.73	0.53
5	0.89	0.80
7	0.96	0.92
9	0.98	0.97

For glass slide substrate

number of the layers	reflectivity	reflectance
3	0.81	0.66
5	0.93	0.86
7	0.98	0.95
9	0.99	0.98

4.4 Fabrication and Monitoring of The Dielectric Coating

The quality of the high reflective dielectric coating is influenced by the quality of the coating materials, the operation method and the accuracy of the thickness of each layer by monitoring. Among them, the accuracy of the thickness monitoring is the key point for high reflective dielectric coating. Using present technology, the absorption loss level for the coating can be made negligibly small, at the visible and near-infrared region, which the absorption loss of the coating less than 0.5% can be achieved with ease, 0.1% with extra care and 0.01% with available with

minute attention to detail [3]. For the monitoring techniques, there are two ways available and will be discussed as following, namely optical monitoring and quartz crystal monitoring (physical monitoring).

Let's discuss the quartz crystal monitoring first. The principle of the quartz crystal monitoring is to expose the crystal to the overprint stream and to measure the change of its resonant frequency as the film deposited on the crystal surface changes the total mass of the monitoring crystal, because any disturbance of its mechanical properties will cause a change on its resonant frequency of which the reduction of the frequency is proportional both to the square of the resonant frequency and to the mass of the film deposited. In the monitoring setup, the change of the resonant frequency can be measured by comparing it with a standard frequency. In this way, the tested frequency shift will be converted into the measurement of the thin film thickness. In a typical crystal monitoring setup, the measurement of the depositing thickness can be carried out to an accuracy of around 2% for each layer, of which it got a lot of application in metal film evaporation as well as some simple dielectric coatings.

The other method is optical monitoring which is commonly used in multilayer dielectric coatings. The optical monitoring system consists of some sort of light source illuminating the testing sample, and it has a photodiode circuit to analyses the reflected or transmitted light. From the results of analysis, the evaporation of the alternative layers is stopped as quickly as possible at the correct point (in most case, the turning point), that is, closing the shutter. The principle of the optical monitoring is based on that, if the coated film is without absorption, its reflectance and transmittance measured by the photodetecting circuit at any monitoring wavelength will vary with the thickness in a cyclic manner, similar to a sine wave and the turning point correspondes to those wavelengths for which the optical thickness of the film is an integral number of the

quarter of the wavelength. Compared with the quartz crystal monitoring, the optical monitoring on the thickness of each layer is not very accurate, however on the whole, the quality of the highly reflective coating is quite reasonably good by optical monitoring. As result, the monitoring of the the thickness for each layer is the entire effects of all the previous coating layers, therefore, it can compensate the inaccuracy in the last a few layers, also compensate the inuniformity of the index during the evaporation. In order to get the good monitoring accuracy from this method, the output of the detecting circuit should be displayed on a chart recorder, and this makes it easy to determine the turning value. With this arrangement, it is not difficult to terminate the layers to an accuracy of 5 to 10% [3].

Although the thickness monitoring techniques of the optical coating have been generally discussed, the optical monitor we designed is slightly different for evaporator 18E at Dept. of Electronic and Electrical Engineering in University College London, as the limitation of the facility in our laboratory. The monitoring system consists a DC biased AC signal generator, a LED driving circuit to modulate the optical source LED, a monitoring head which is a metal block with a LED and a photodiode only, locating the a proper position to monitoring the thickness without stopping the evaporant beam to reach the specimen which is shown in Fig. 4.4, a photodiode receiving circuit to amplify the transmitted signal, a lock-in amplifier to transfer the monitoring signal from AC to DC, a chart plotter to display the system output and determinate the turning value, and an oscilloscope which shows both input and output signals to monitoring to evaporating the coating procedure, and the diagram of the whole monitoring system is given in Fig. 4.3. The high reflective coatings are designed to operate at the wavelength of 1.15 μm, however, the the monitor source is only available for 940 nm LED with spectral bandwidth of 50 nm. By the

monitoring arrangement shown in Fig. 4.3, we arrange the monitoring sample slightly away from the central area where the device sample is, therefore, the coating thickness for the device sample at the center is slightly thicker than the monitoring sample which is a little distance away. By testing the thickness difference of monitoring sample and device sample for both high-index material Zinc Sulphide and low-index material Cryolite using Telestep, we found that the thickness of device samples at the centre is roughly 25% thicker for Cryolite single layer, and 15% thicker for Zinc Sulphide single layer than that for monitoring sample 3 cm away from the centre. Although the bandwidth of the high reflective coating for 940 nm is around 34.8% which is from 800 nm to 1138 nm of which the reflectance at 1.15 μm is out of the high reflective zone, but we still get quite good high reflective coating at 1.15 μm because of the thickness shift of the coating and the centre wavelength of the coating shifts up some average 20% from 940 nm to 1.13μm.

By testing the reflectance of the samples on which the coatings were deposited for 3-, 5-, 7-, 9-layer using monochrometer from 800 nm to 1900 nm which is shown in Fig. 4.5, it was seen that the central wavelength is around 1.23 μm although it was expected around 1.13, e.g. it means that maybe more thickness shifts have been caused during the multi-layer evaporation or the non-uniform thickness shift on different layers, the high reflectance zone is about 33.3% (from 1020 nm to 1430 nm at central wavelength of 1230 nm) almost the same as we expected. However, the peak reflectances at the wavelength of 1.15 μm for 3-, 5-, 7-, 9-layer coatings are 51%, 78%, 89% and 95%, which are almost the same as we have calculated before.

4.5 Conclusion

In this chapter, we have discussed and summarised: the basic principle of the highly reflective dielectric coating; the designing of the

coatings for the Fabry-Perot modulator; the thickness monitoring mechanisms and methods; a different fabricating method; and high reflectance zone measurement, which are essential for a optical waveguide resonator.

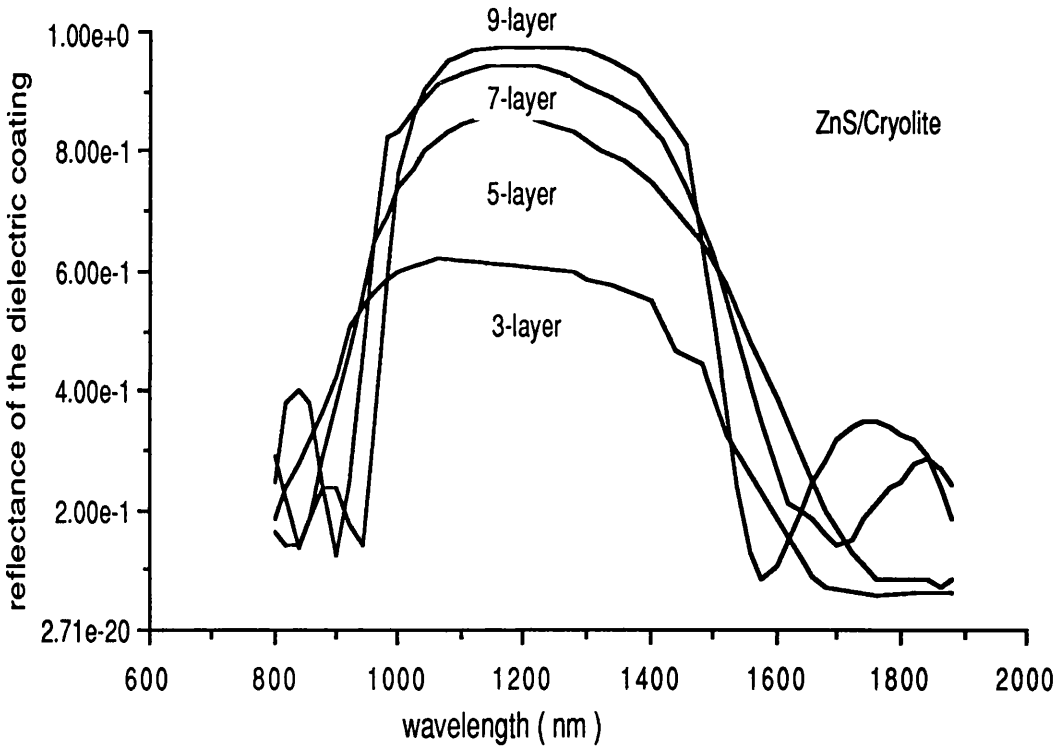

Fig. 4.5 Tested reflectance R for normal incidence
for 3-, 5-, 7-, 9-layer coatings vs wavlength

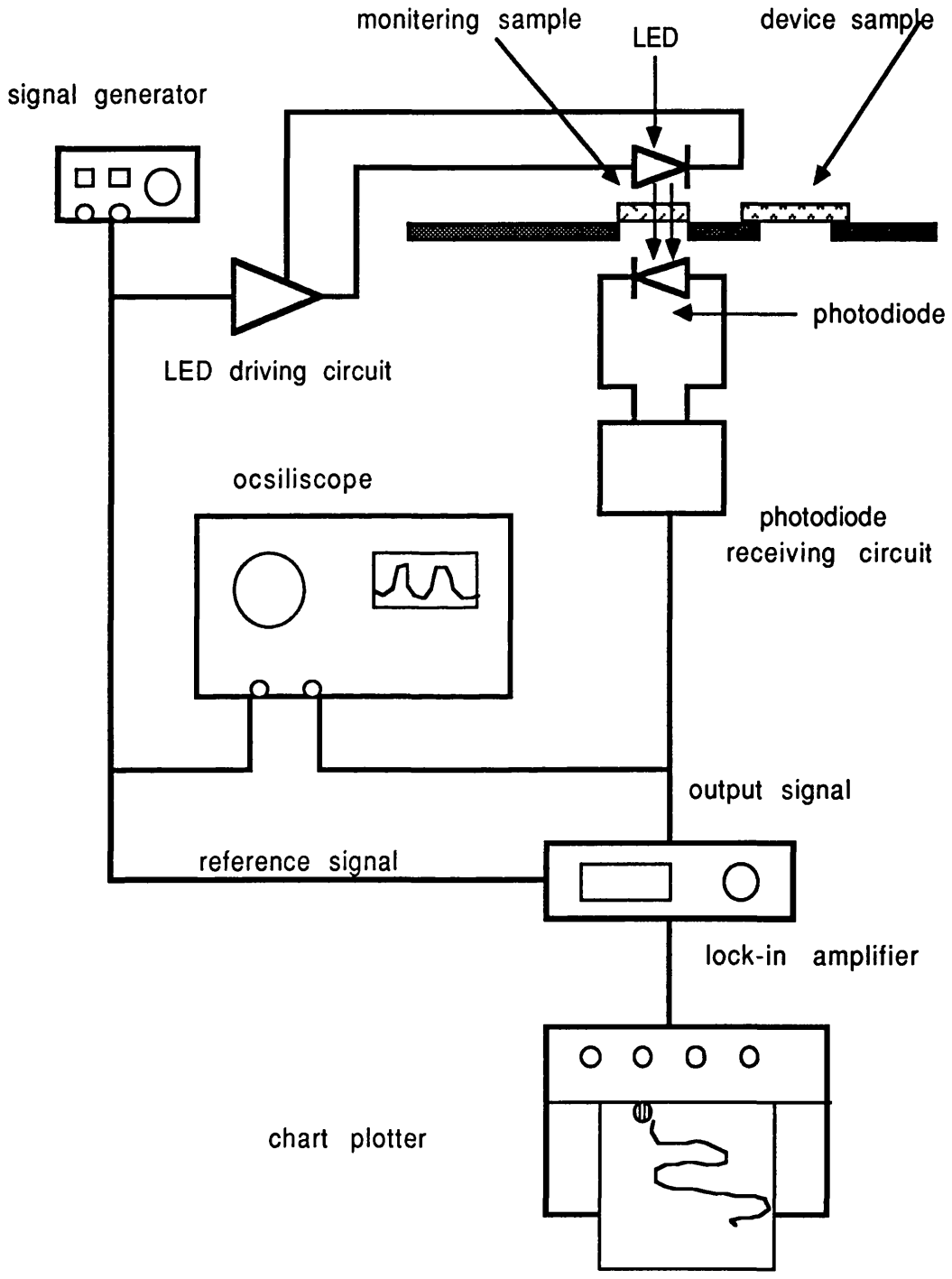

Fig. 4.3 diagram of optical monitoring system for dielectric coating

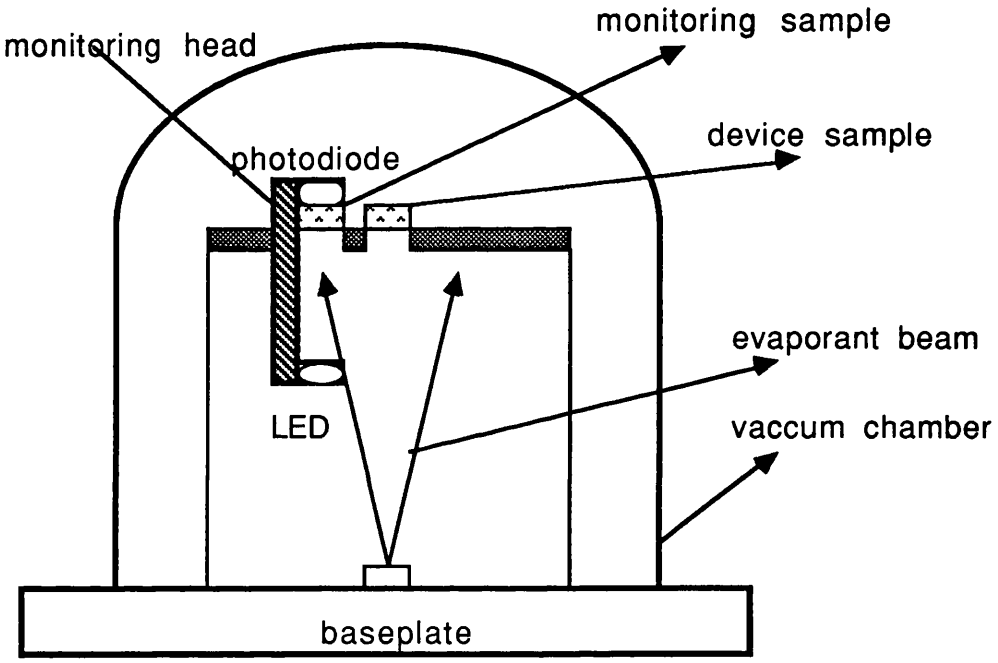

Fig. 4..4 Diagram of optical monitoring set-up in vaccum chamber

4.5 Reference

[1] M. M. Stallard, R. A. Cole, F. Morris and D. John " Thin film optical technology in integrated optic device fabrication ", Optics and Laser Tech., Vol.20, No. 4, pp-185, August, 1988.

[2] E. Hecht and A. Zajac, " Optics ", Chapter 9, Addision-Wesley Publishing Company, 1974.

[3] H. A. Macleod, " Thin-film optical filters ", Chapter 5, Adam Hilger Ltd, Bristol, 2nd ED, 1986.

CHAPTER 5 THE DC CHARACTERISTICS OF FABRY-PEROT MODULATION

5.1 Introduction

The Fabry-Perot integrated modulator is a new concept structure of modulator, which has been developed for low driving power and a simple structure. Its basic element is the optical cavity which is composed of a single mode straight waveguide and two highly reflective dielectric coatings at the ends of the waveguide. The cavity gives the DC characteristics of the modulator, which is decided by the reflectivity of the coatings, the length of the cavity and the optical losses of the waveguide. In this chapter, the DC characteristics such as maximum optical output, minimum optical output, maximum available modulation depth, and the phase shift for certain modulation, as well as total optical losses of the cavity are discussed.

5.2 The Fabry-Perot Etalon

The Fabry-Perot etalon is a type of optical resonator. It consists of a pair of plane parallel partially reflecting surfaces, separated by distance d, between which light undergoes multiple reflection. A diagram of the Fabry-Perot etalon is shown in Fig. 5.1. If we consider a ray of light incident at an angle of θ to the normal (as shown in Fig. 5.1), we can see how the transmitted of the cavity is built up.

The light, once coupled into the device will, at each encounter with either of the two reflecting surfaces, undergo partial reflection and partial transmission. Thus the output intensity is made up from an

infinite number of contributions to a partial sum. Similarly, a reverse beam is built up from contribution in the reverse direction and the power level built up within the cavity itself consists of the contribution from each pass of the light across the cavity.

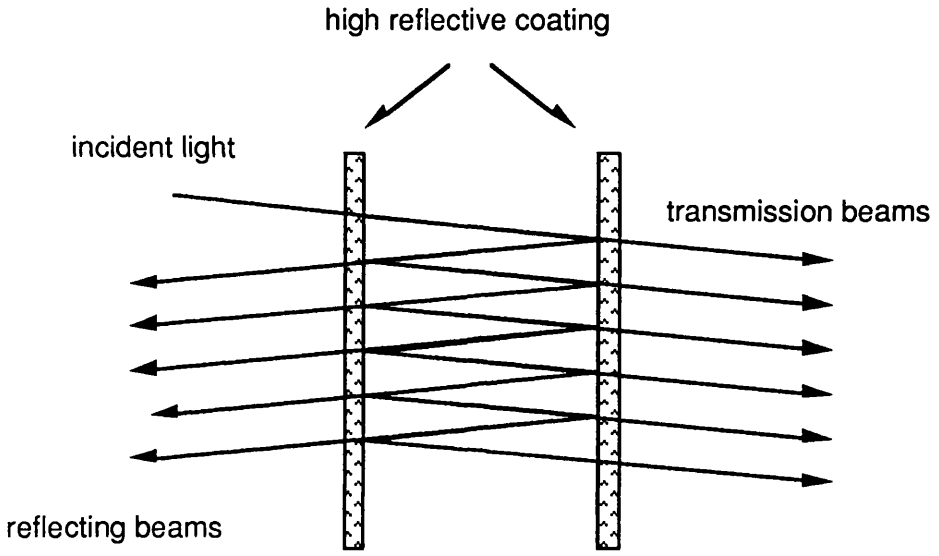

Fig. 5.1 the diagram of Fabry-Perot cavity

In the optical cavity, the loop phase shift, 2δ, between two successive partial wave due to a double transit of the cavity is given by:

$$2\delta = 4\pi nd \cos\frac{\theta}{\lambda} \qquad (5-1)$$

where n is the refractive index of the material within the cavity, λ is the vacuum wavelength of the incident light.

The r_1 and t_1 are defined as the forward reflection and transmission coefficients, r_1' and t_1' the reverse coefficients at first reflecting plane (2

means the second), E_i the complex amplitude of the incident wave. The individual components of the transmitted wave are thus:

$$E_1 = E_i t_1 t_2' \exp(-\alpha L + \delta j) \qquad (5-2)$$

$$E_2 = E_i t_1 t_2' r_1' r_2' s_1 s_2 \exp[-3\alpha L + (3\delta + \delta_1 + \delta_2) j]$$

$$E_n = E_i t_1 t_2' (r_1' r_2' s_1 s_2)^{n-1} \exp\{-(2n-1)\alpha L + [(2n-1)\delta + (n-1)(\delta_1 + \delta_2)]j\} \qquad (5-3)$$

We assume that the etalon has a absorption coefficient α, scattering coefficient s_1 ,s_2 on the surface 1 and 2, δ_1 and δ_2 are the phase shift caused by the dielectric coating layers. E_t is the total transmission amplitude of the interferometer. So:

$$E_t = E_1 + E_2 + \cdots + E_n$$
$$= \sum_n E_i t_1 t_2' (r_1' r_2' s_1 s_2)^{n-1} \exp\{-(2n-1)\alpha L + [(2n-1)\delta + (n-1)(\delta_1 + \delta_2)]j\} \qquad (5-4)$$

let

$$M = r_1' r_2' s_1 s_2 \exp[-2\alpha L + (2\delta + \delta_1 + \delta_2) j] \qquad (5-5)$$

then

$$E_t = \sum E_i t_1 t_2 M^{n-1} \exp(\delta j - \alpha L)$$

$$= \frac{E_i t_1 t_2 \exp(\delta j - \alpha L)}{1 - M} \qquad (5-6)$$

therefore

$$t = \frac{E_t}{E_i} = \frac{t_1 t_2 \exp(\delta j - \alpha L)}{1 - M} \qquad (5-7)$$

and

$$T = t\,t^* = \frac{(t_1 t_2)^2 \exp(-2\alpha L)}{(1 + M^2 - M^* - M)} \qquad (5-8)$$

substitute M into last equation:

$$T = \frac{(t_1 t_2)^2 \exp(-2\alpha l)}{[1 - r_1' r_2' s_1 s_2 \exp(-2\alpha l)]^2 + 4 r_1' r_2' s_1 s_2 \exp(-2\alpha l) \sin^2 \delta_0} \qquad (5-9)$$

where $\delta_0 = \delta + (\delta_1 + \delta_2)/2$, So, the maximum transmission coefficient T is;

$$T_{max} = \frac{(t_1 t_2)^2 \exp(-2\alpha L)}{[1 - r_1' r_2' s_1 s_2 \exp(-2\alpha L)]^2} \qquad (5-10)$$

Since $t_1 t_2 = T'$ and $r_1' r_2' = R'$ for symmetry dielectric coating cavity which $r_1' = r_2' = r$, $t_1 = t_2 = t$, also $s_1 = s_1 = s$. $T' + R' = 1 - (1 - s)^2 = 2s - s^2$, where T' and R' are the intensity transmission and reflection coefficients.

so

$$T = \frac{(2s - s^2 - r^2) \exp(-2\alpha L)}{[1 - s^2 r^2 \exp(-\alpha L)]^2} \qquad (5-11)$$

For dielectric coating, the scattering coefficient is neglecting small, so we suppose that s = 1, we get;

$$T = \frac{(1-r^2)^2 \exp(-2\alpha L)}{[1-r^2\exp(-2\alpha L)]^2 + 4r^2\exp(-2\alpha L)\sin^2\delta_0} \qquad (5\text{-}12)$$

which is an Airy-like function.

5.3 DC Properties in Lossless Cavity

For the lossless cavity which means the absorption coefficient α = 0, we have the transmission coefficient of the cavity,

$$T = \frac{(1+r^2)^2}{(1-r^2)^2 + 4r^2\sin^2\delta_0} \qquad (5\text{-}13)$$

which T is a pure Airy function, and the shape of the output is depends on the reflecting coefficient R =r^2, and is shown in Fig. 5.2. The properties of the cavity is as following:

the maximum available output:

$$T_{max} = 1 \qquad (5\text{-}14)$$

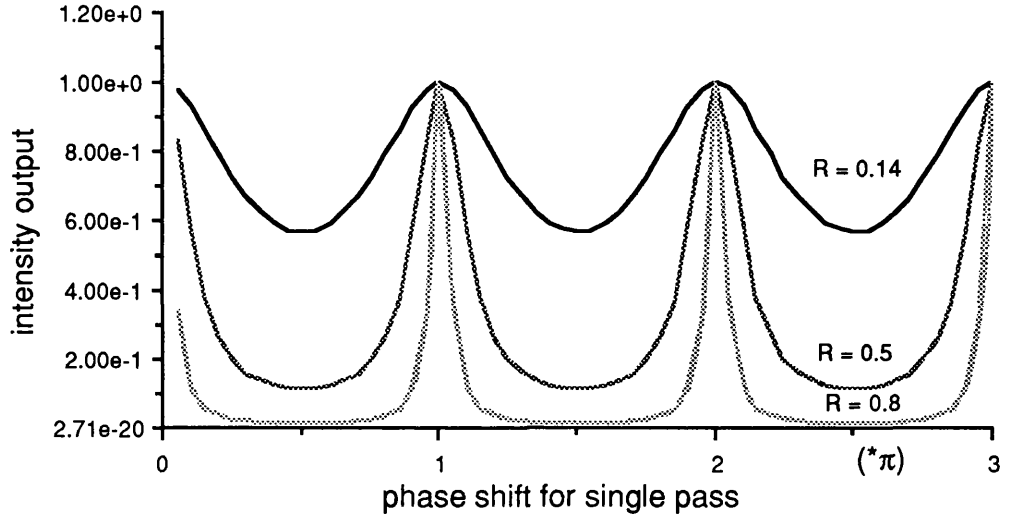

Fig. 5.2 Airy function output of Fabry-Perot cavity for different reflectance

the minimum available output:

$$T_{min} = \frac{(1-r^2)^2}{(1+r^2)^2} \qquad (5-15)$$

the maximum available modulation depth:

$$D = \frac{T_{max} - T_{min}}{T_{max}} = 1 - \frac{(1-r^2)^2}{(1+r^2)^2} \qquad (5-16)$$

the halfwidth (phase)

$$\Delta\delta_0 = 2\,\mathrm{arcsin}\left(\frac{1-r^2}{2r}\right) \qquad (5-17)$$

As above, we can conclude that for the lossless condition (T_{max} =1), as it is no optical losses in the cavity. As the reflectivity increases, the

minimum output gets decreased and maximum available modulation approaches to 1, while the halfwidth $\Delta\delta$ decreases rapidly, that means that small phase shift could cause large output change.

5.4 DC properties in the lossy cavity

For the lossy condition that means the absorption coefficient $\alpha > 0$, the situation is different as the lossy property reduces the amplitude of every transmitting beam inside the cavity, so changing the total output of the cavity. We can get the characteristics of the cavity;

the transmission coefficient of the cavity (optical losses);

$$T = \frac{(1-r^2)^2 \exp(-2\alpha L)}{[1-r^2\exp(-2\alpha L)]^2 + 4r^2\exp(-2\alpha L)\sin^2\delta_0} \qquad (5-18)$$

the maximum available output

$$T_{max} = \frac{(1-r^2)^2 \exp(-2\alpha L)}{[1-r^2\exp(-2\alpha L)]^2} \qquad (5-19)$$

We can see that the maximum available output is no longer equal to 1, it depends on the reflectivity and the absorption coefficient of the cavity. Fig. 5.3 shows the optical losses of the Fabry-Perot cavity as the reflectivity of the cavity increases for different loss coefficients, 0.1dB/cm, 0.2dB/cm, 0.5dB/cm and 1.0dB/cm for 2cm long cavity. We find that, as the reflectivity goes higher, the output losses increase tremendously and more seriously for larger loss coefficient.

For minimum available output, we have;

$$T_{min} = \frac{(1-r^2)^2 \exp(-2\alpha L)}{\{1-r^2\exp(-2\alpha L)\}^2 + 4r^2\exp(-2\alpha L)} \qquad (5-20)$$

we can get the results that the minimum available output also depends on the reflectivity and absorption coefficient.

The maximum available On-Off ratio;

$$D = \frac{T_{min}}{T_{max}} = \frac{1}{1 + \dfrac{4R\exp(-2aL)}{[1+R\exp(-2aL)]^2}} \qquad (5-21)$$

Just like maximum and minimum available outputs, the maximum available modulation depth is reflectivity and loss coefficient dependent as well. Fig. 5.4 indicates that the maximum available on-off ratio is increased as the reflectivity of the cavity increases for different loss coefficient, 0 dB/cm, 0.1dB/cm, 0.2dB/cm, 0.5dB/cm and 1.0dB/cm for 2cm long cavity.

We also have the applied votage required for 50% on-off ratio vs reflectivity at different loss coefficients;

$$\Delta V = 2\arcsin\sqrt{\frac{[1-r^2\exp(-2\alpha L)]^2}{4r^2\exp(-2\alpha L)}}\ \frac{V_\pi}{\pi} \qquad (5-22)$$

As above, ΔV is still reflectivity and loss coefficient dependent. Fig. 5.5 shows that ΔV becomes smaller as the reflectivity of the cavity increases for different loss coefficient, 0dB/cm, 0.1dB/cm, 0.2dB/cm, 0.5dB/cm and 1.0dB/cm for 2cm long cavity.

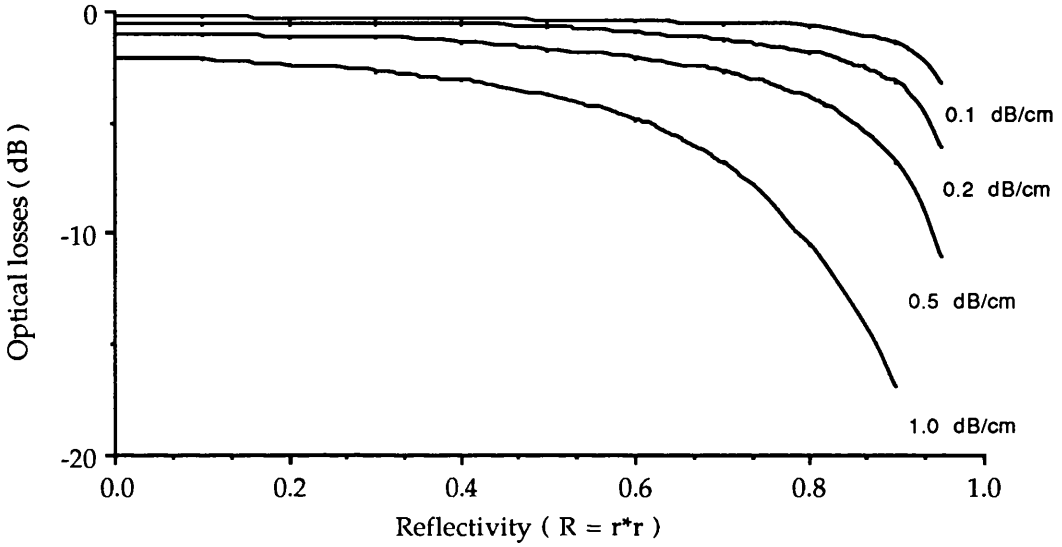

Fig. 5.3 The optical losses of the Fabry-Perot etalon vs relectivity for lossy cavity

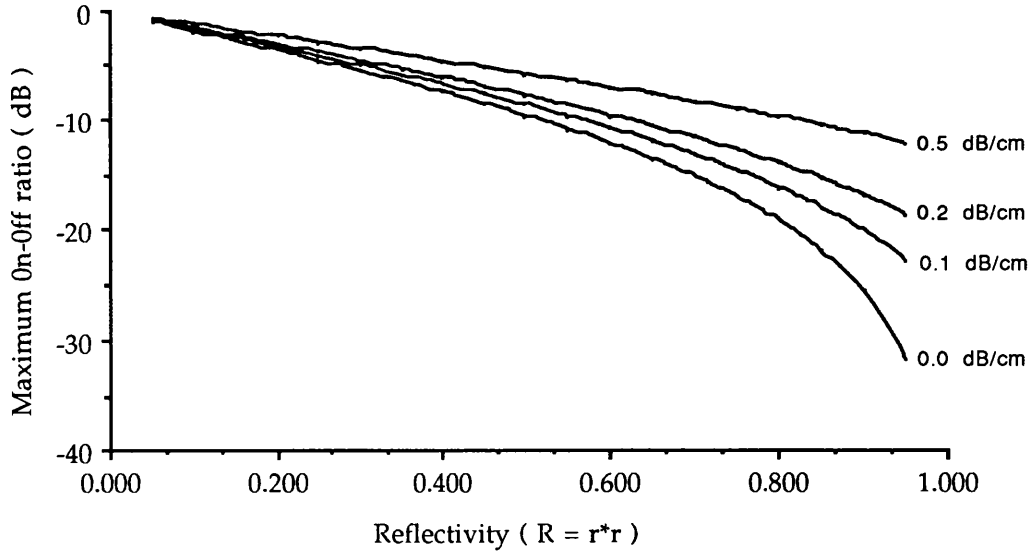

Fig. 5.4 The maximum on-off ratio of Fabry-Perot etalon vs reflectivity for lossy cavity

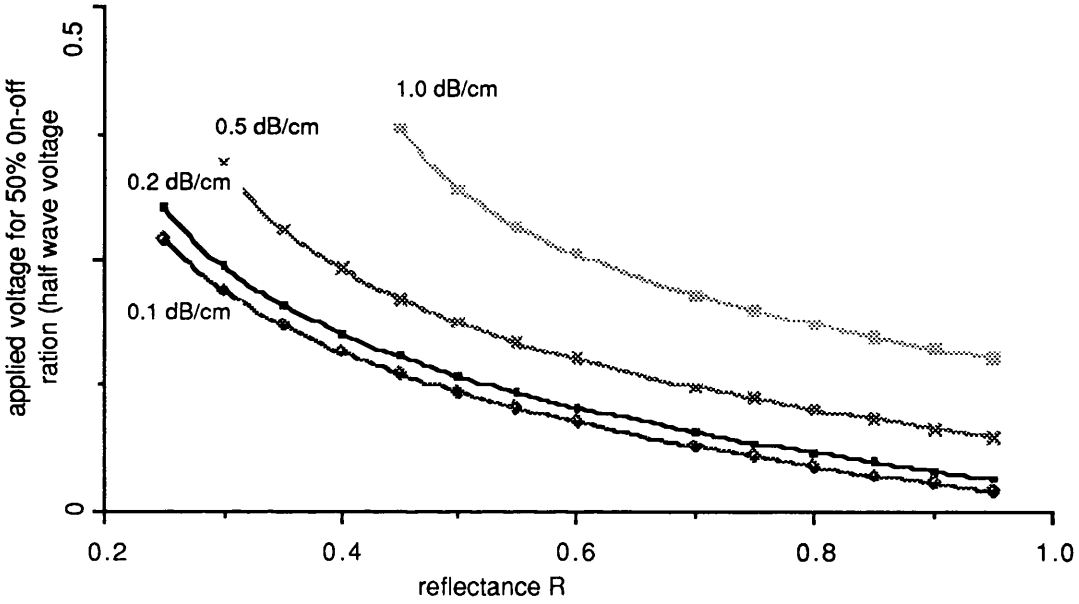

Fig. 5.5 The applied voltage for 50% on-off ratio of Fabry-Perot etalon versus (R = r*r) for different loss coefficients

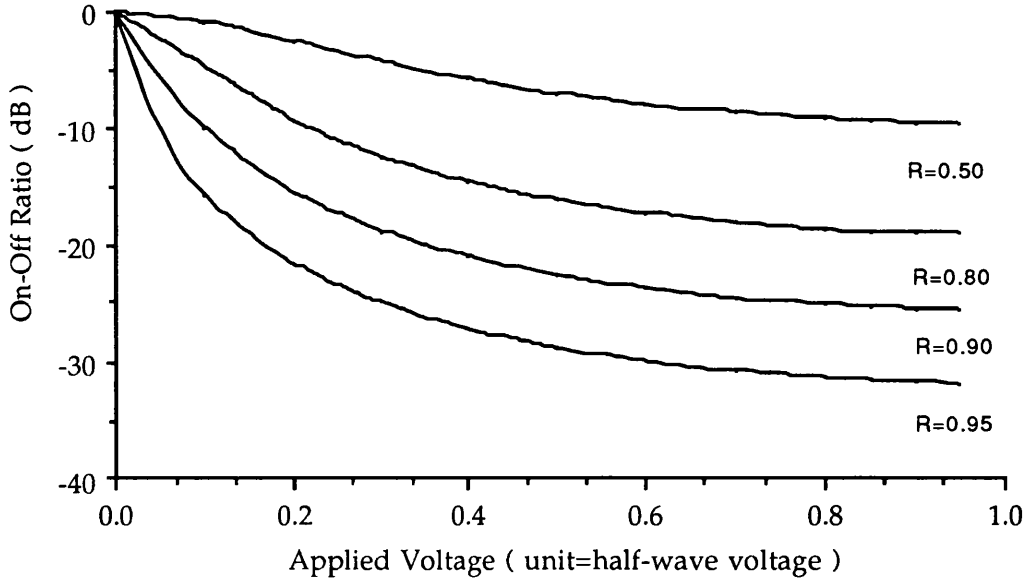

Fig. 5.6 The On-Off ratio of F-P etalon vs applied voltage for different reflectivity

Fig. 5.6 shows the on-off ratio vs applied voltage at different reflectivity. We notice that the on-off ratio increase very fast as we start to apply the voltage and get slow down towards the half-wave voltage.

5.5 The Guiding Properties of The Fabry-Perot Cavity in Optical Waveguide Etalon

The properties of the conventional Fabry-Perot cavity are mainly decided by the reflectivity of the mirrors at the ends of the cavity, the length of the cavity and the loss of the cavity which have been discussed before, moreover, in practical situations, the *wedge angle* θ_w which is defined as the non-normal angle between the normal positioned mirror and actual mirror as shown in Fig. 5.9. In most Fabry-Perot interferometers, the high reflective mirrors of the cavity are adjustable in order to get the good interference by varying the reflecting direction of the mirrors. If the reflecting mirrors are not normal to the transmitting optical beams, we can not get the pure intensity change from the cavity output because it forms the interference fringe on the output spot which degrades the whole Fabry-Perot interference. Moreover, if the wedge angle is large enough, the reflecting beams might run out of the interference area which have no any interference effect.

For the Fabry-Perot cavity fabricated in an optical waveguide, the situation is quite different from the conventional cavity. Firstly, it is impossible to propagate TEM waves in the waveguide by the eigenvalue equation and only approximately TE or TM mode available for single mode waveguide which means that only one mode (wavefront) can travel in the waveguide no matter what the input situation is [6]; Secondly, although it could be a wedge angle at the ends of the cavity, the reflected optical wave is reflected back to the optical waveguide without changing the direction and wavefront if the reflected angle is smaller

than the critical angle, so it cannot cause any interference fringe at the output spot; finally, the wedge angle will cause the extra loss because the mode field profile mismatch before and after the reflection [7] which is discussed as following.

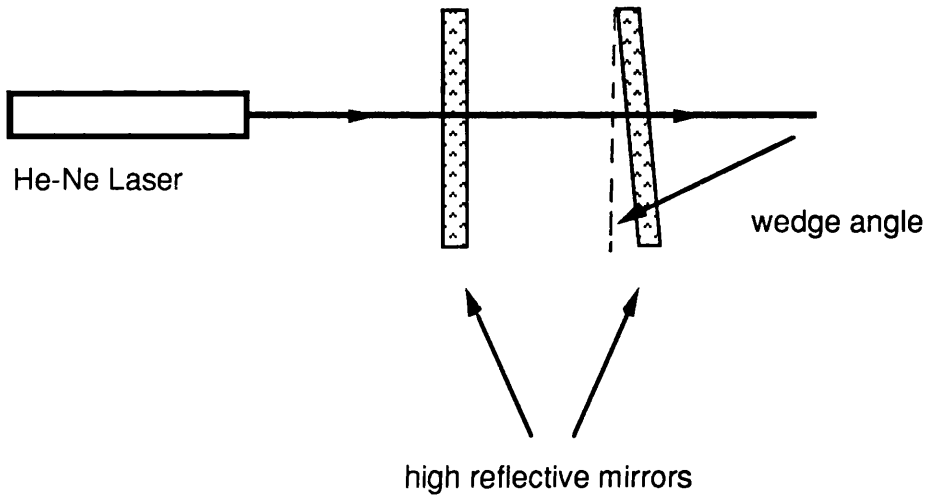

Fig. 5.7 The conventional Fabry-Perot interferometer with a wedge angle

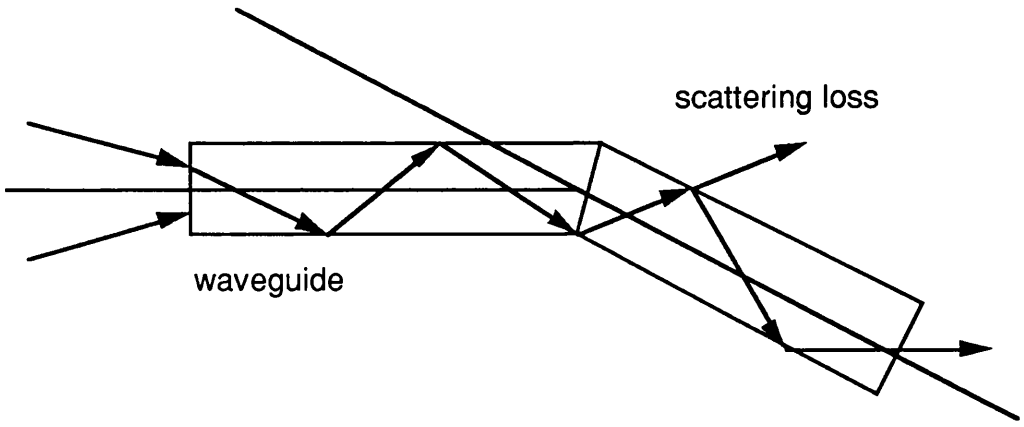

Fig. 5.8 The diagram of unfolded Fabry-Perot cavity as two identical waveguides with wedge angle

In order to investigate the loss property of Fabry-Perot cavity in optical waveguide caused by the wedge angle, we unfold the cavity as two straight waveguides joined together at a certain discrete angle shown as Fig. 5.10, in which case there exists a discontinuity in the direction of the optical waveguide. If the wedge angle is zero, there is no any extra optical loss at all; however, in practice, there is always a wedge angle by the cavity fabrication in the waveguide, e.g. the polishing. Therefore, we can calculate the amplitude transmission coefficient a_0 due to the mode field profile mismatch on the opposite sides of the junction for single-mode optical waveguide [8] as following;

$$a_0 = \int E_{02} \cdot E_{01}^{*} \, dA \qquad (5-23)$$

where E_{01} is the electric mode profile field of the fundamental mode of the first waveguide normalised to unit power and E_{02} is the second, A is the infinite cross-sectional area of the junction between the two waveguides. From Marcuse's result [9], we have the optical power transmission coefficient;

$$a_0^2 = \exp\left(-\beta^2 W_0^2 \sin^2 \theta_w\right) \qquad (5-24)$$

$$\beta = \frac{2\pi n_g}{\lambda} \qquad (5-25)$$

where β is the propagation constant and n_g is the effective index of the waveguide, λ is the propagating wavelength

.

$$W_0 = \frac{(X_{01} X_{02})^2}{X_{01}^2 + X_{02}^2} \qquad (5-26)$$

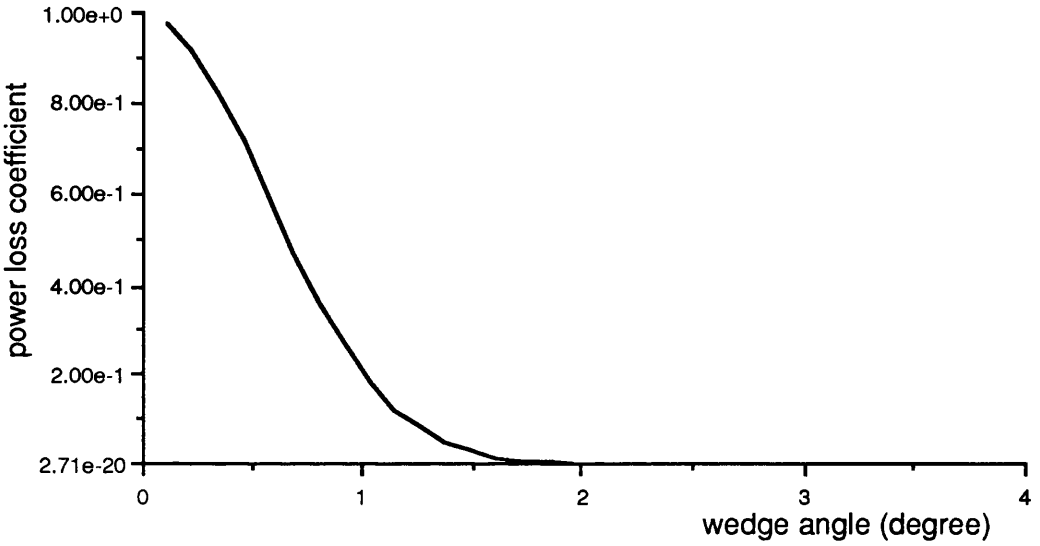

Fig. 5.9 (a) power loss coeff. of Fabry-Perot cavity vs. wedge angle

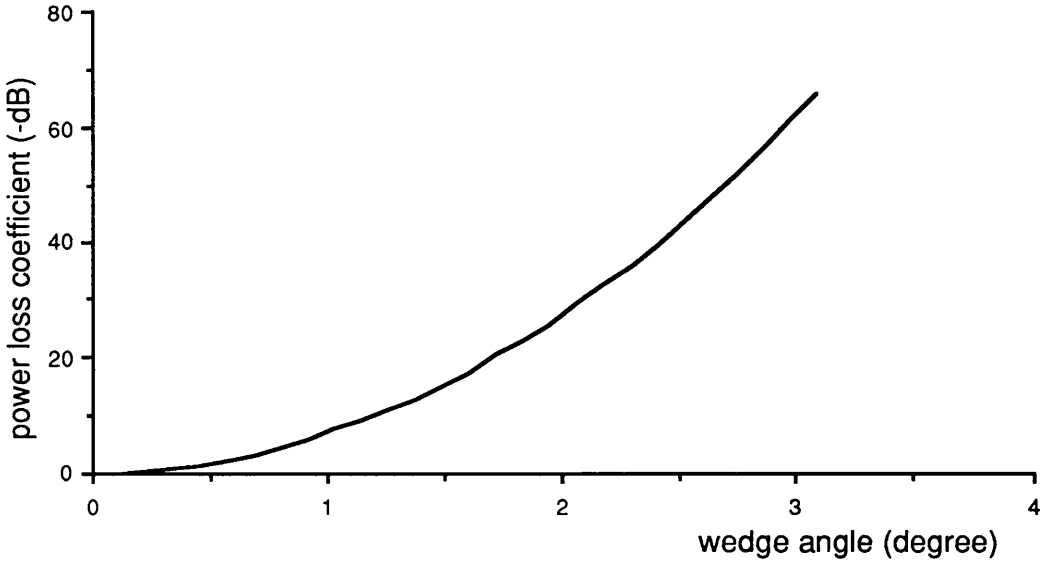

Fig. 5.9 (b) power loss coeff. of Fabry-Perot cavity vs. the wedge angle

where W_0 is the mode size mismatch coefficient and X_{01}, X_{02} are the width of the fundamental mode. For the unfolded model of the Fabry-Perot cavity, we treat it as two identical straight waveguides, therefore, to get the power transmission coefficient a_0^2 vs. the wedge angle given in Fig. 5.8 (a) & (b). We notice that if the optical loss caused by the wedge angle is required less than 1dB, the wedge angle must be less than 0.32^0 and the total effective reflectance is $R = a_0^2 R\exp(-\alpha l)$; if the wedge angle is 1^0 caused by polishing, the optical loss at one side will be -7 dB and -23 dB for 2^0 angle.

5.6 Minimisation of the Wedge Angle

Using the conventional method to fabricate the Fabry-Perot integrated optical modulator in the department, we can not guarantee the wedge angles at the ends of the Fabry-Perot cavity to be less than 1^0. However from the above discussion, we must make sure the wedge angle is less than 0.3^0 if we want that the loss caused by the wedge angle to be less than 1 dB. Therefore, in order to limit the wedge angle as small as possible, we designed a new polishing-jig set and made sure that the central line was as vertical as possible to the polishing plate, so that we could use the central line as the fixed reference line which is given in Fig. 5.9. Furthermore, we aligned the straight optical waveguide as parallel as possible to one side of the substrate which can be used as another reference line. Therefore, we were able to gain a very small wedge angle by this polishing jig, by aligning the two reference lines together.

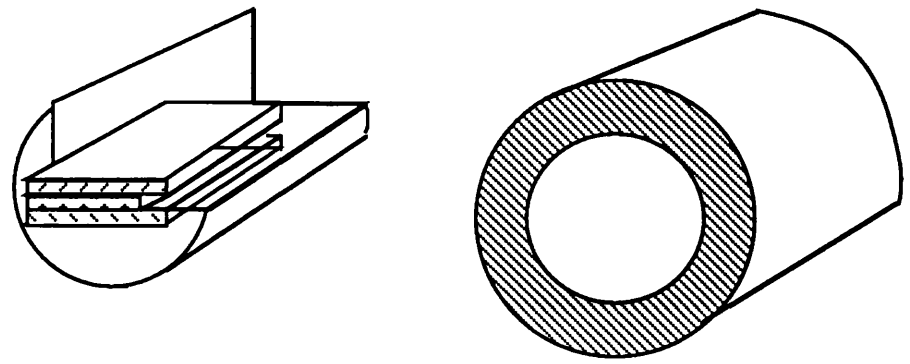

Fig. 5.10 the polishing jig for getting a good wedge angle on Fabry-Perot cavity

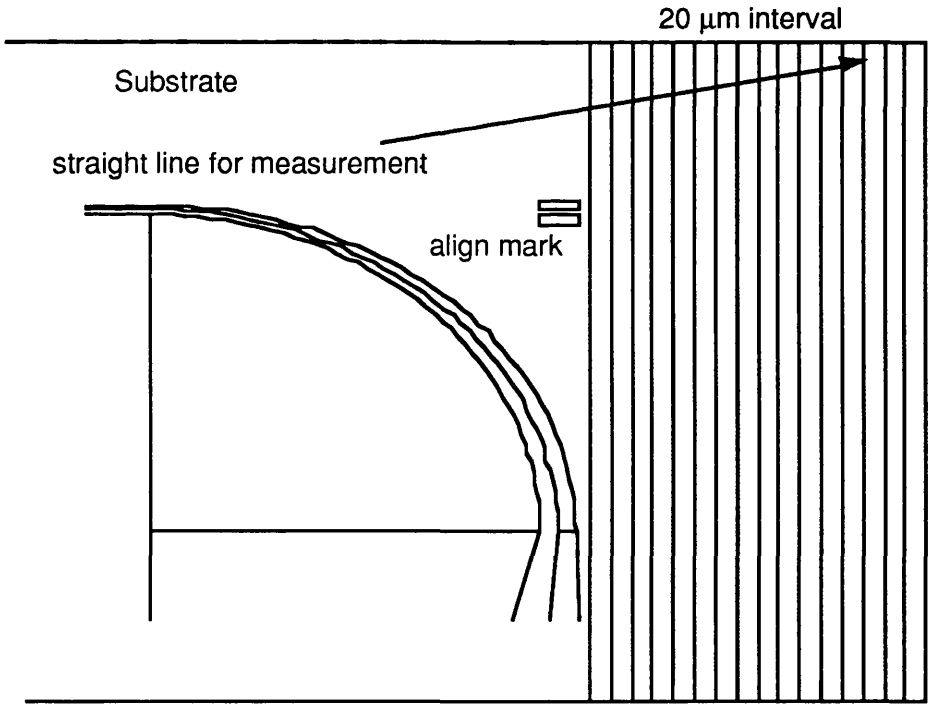

Fig. 5.11 The mask for measuring the wedge angle on Fabry-Perot cavity

In order to test the wedge angle making sure that the wedge angle was small enough, we tried to measure the wedge angle as accurate as possible to make sure the wedge angle is in tolerance. Therefore, we designed some special reference lines on the electrodes masks. The masks had a number of straight strip slightly apart from the electrodes, which is perpendicular to the electrodes aligning to the waveguide as shown in Fig. 5.10. When the electrodes were deposited on the substrate, the reference lines were "printed" at the ends of the waveguide. Therefore, the intersection of the polishing edges of the waveguide and the reference lines can be been seen by a microscope to measure wedge angles. As the the interval and the width of the straight strip were designed to be 20 μm, the measure accuracy for the wedge angles which was roughly 0.05^0 for a 1 cm wide sample is good enough in guiding Fabry-Perot cavity.

5.7 Conclusion

From the above discussion for lossless and lossy cavities, we find that the output characteristics of Fabry-Perot cavities are decided by the reflectivity of the coating, the length of the cavity, the optical wavelength and the loss property of the cavity. We have shown how the optical losses inside the cavity influence the maximum available output, maximum available modulation depth and the halfwidth $\Delta\delta$. In order to obtain reasonably good modulation properties, we must trade-off the maximum available output, maximum available modulation depth and necessary phase shift by varying the cavity parameters of reflectivity and optical losses Moreover, we can use this method to measure the optical losses of the waveguide very accurately by testing the width of the $\Delta\delta$ compared with calculated one[5]. Also, a new improved polishing jig and mask were designed to make the wedge angles as small as possible.

The modulation characteristics of a Fabry-Perot integrated optical modulator is decided not only by the DC characteristics of Fabry-Perot cavity, but also by the multi-transmission properties in the optical waveguide of the cavity of which the wedge angle causes optical loss degrading the Fabry-Perot interference.

5.8 Reference

[1]. M. Born and E. Wolf, " Principle of Optics ", Pergamon Press, London, 1959.

[2]. E. Hecht and A. Zajac, " Optics ", Addison-Wesley Publishing Company, London, 1974.

[3]. A. Yariv, " Optical Electronics ", Holt-Saunders International Editions, 3rd ED, London,1985.

[4]. A. Bruland and W. Sohler, " Reflection mode integrated optical Fabry-Perot modulator ", Proc. of the 4th European Conference on Integrated Optics, ECIO 87, pp-44, Glasgow.

[5]. H. Suche and W. Sohler, " Single frequency pumped doubly resonant integrated optical parametric oscillator of very high efficiency ", Technical Digest Series, Vol. 5, pp-176, 1988.

[6]. M. J. Adams, " An Introduction to Optical Waveguides ", John Wiley & Sons, 1981.

[7]. A. W. Snyder and J. D. Love, " Optical Waveguide Theory ", Part 2, Chapman and Hall, 1983.

[8]. L. D. Hutcheson, ED, " Integrated Optical Circuits and Components: Design and application." Chapter 4, Marcel Dekker, INC., 1987.

[9]. D. Marcuse, " Radiation losses of parabolic index slab and fibres with bent axes, Appl. Optics, Vol. 17, pp-755, 1978.

CHAPTER 6 INVESTIGATION OF TEMPERATURE SENSORING IN FABRY-PEROT CAVITY BY REFLECTION MODE METHOD

6.1 Introduction

Temperature sensing in integrated optics has been investigated by a number of groups; L. M. Jonson and F. J. Leonberger [1], described a multi-unequal-arms Mach-Zehnder interferometer temperature sensor at 0.63 μm, and achieved a half wave temperature of about 40 ^{0}C and an extinction ratio of 50%; M. Haruna, H. Nakajima and H. Nishihara [2] described an optical π-arc waveguide Mach-Zehnder interferometer temperature sensor, and obtained a half wave temperature of 0.3 ^{0}C and an extinction ratio of 50%; M. Izutsu, A. Enokihara and T. Sueta [3] described a reflecting Mach-Zehnder interferometer temperature sensor, and obtained a half wave temperature of 0.32 ^{0}C and an extinction ratio of 30%.

In the Fabry-Perot integrated optical modulator, the temperature sensitivity plays a crucial role in the modulation performance as the temperature change will cause the refractive index variation and the length drift of the optical cavity. This will change the DC bias of the modulator, which is the optimal working point of the optical modulation in any kind of interferometer modulator. Therefore, the temperature change in the Fabry-Perot integrated optical modulator will degrade the performance of the modulation, and even make the integrated optical Fabry-Perot modulator unsuitable for use in practice. Therefore, the temperature control becomes the additional key factor in the use of an integrated optical Fabry-Perot modulator.

In order to control the temperature change in an integrated optical Fabry-Perot modulator on a lithium niobate substrate, the temperature sensitivity of the modulator is investigated in this chapter. Here, a different way of temperature sensitivity measurement is presented. As it can be used as a temperature sensor in some case as well, we can call it as the " Reflecting Mode Integrated Optical Temperature Sensor". It is based on a single straight waveguide with a reflecting mirror at the rear end of the waveguide which is shown in Fig. 6.1, and it has a similar structure as the Fabry-Perot cavity.

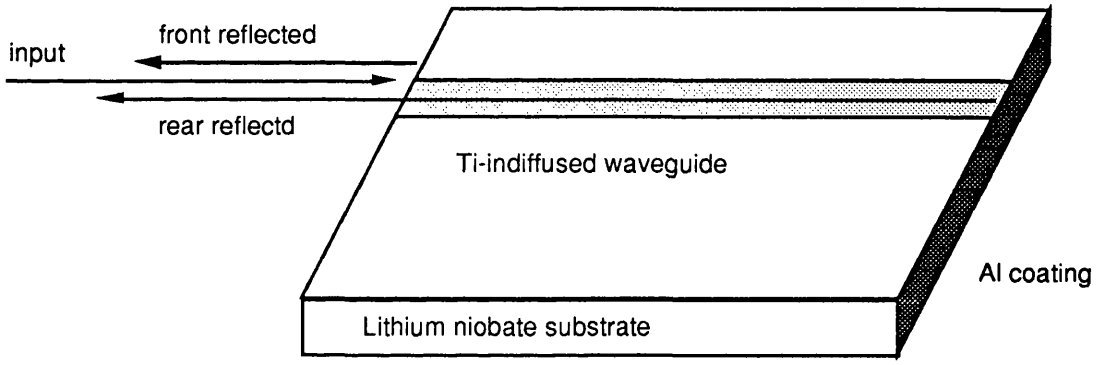

Fig. 6.1, The strctrure of reflecting mode temperature sensor

The experimental device was fabricated by standard Ti-indiffusion technology which is described in Chapter 2. First, a straight Ti strip of 6 μm wide was formed by a lifting-off photolithographical technique using 80 nm thick of evaporated Ti on Z-cut lithium niobate substrate. Then, the substrate with the titanium strip was put in the furnace for diffusion at 1050 ^{0}C for 10 hours with flowing dry oxygen at rate of 0.5 lit./min. The optical properties of the waveguide was measured, at the wavelength of 1.15 μm; it supported a single mode, and at 0.63 μm, it supported three modes for both TE and TM. It was seen that there is slight outdiffusion at

0.63 μm for TM mode. The integrated optical temperature sensor was formed by depositing a thin layer of 20 nm aluminum coating at the rear end of the waveguide. The mirror creates about 85% reflection and 2% transmission which is useful for monitoring the input light using a TV camera.

6.2. The Principle of the Integrated Optical Temperature Sensing

The basic principle behind this device is the interference between the Fresnal reflection beam from the front end of the waveguide and the optical beam reflected from the rear end by the mirror.

The amplitude of the optical beam reflected from the front end E_1 is as follows;

$$E_1 = E_i r_1 \qquad (6-1)$$

The amplitude of the optical beam reflected from the rear end E_2 is as following;

$$E_2 = E_i t_1 r_m t_1' \alpha \qquad (6-2)$$

where E_i is the input amplitude, r_1 is the Fresnel reflection coefficient at the front end of the waveguide and r_m is the reflection coefficient at the rear end mirror, α is the coupling coefficient of the waveguide, t and t' are the transmission coefficients of input and output at the front end.

the optical output intensity of the temperature sensor $I_{out}(T)$ is;

$$I_{out}(T) = E_1^2 + E_2^2 + 2E_1E_2\cos\{\Phi + \Delta\Phi(T)\} \qquad (6-3)$$

$\Delta\Phi(T)$ is the phase shift caused by the temperature change in the waveguide, which is contributed to both refractive index change and length drift in the optical waveguide.

The refractive index change caused by the temperature change had been investigated by two groups, G. D. Boyd, W. I. Bond and H. L. Carter [4]; as well as H. Iwasaki, H. Toyoda and N. Niizeki [5]. for different wavelength. It can be expressed as a three-term polynomial;

From the dispersion equation (Cauchy's formula) [6];

$$n^{o,e} = p^{o,e} + q^{o,e}\lambda^{-2} + r^{o,e}\lambda^{-4} \qquad (6-4)$$

where $n^{o,e}$ is the refractive index for ordinary and extraordinary modes of lithium niobate substrate, $p^{o,e}$, $q^{o,e}$ and $r^{o,e}$ are characteristic constant of the formula, λ is the optical wavelength. So, we have the refractive index change versus temperature variation as following;

$$\Delta n^{o,e}(T) = \frac{dp^{o,e}}{dT} + \frac{dq^{o,e}}{dT}\lambda^{-2} + \frac{dr^{o,e}}{dT}\lambda^{-4} \qquad (6-5)$$

the data of $dp^{o,e}/dT$, $dq^{o,e}/dT$ and $dr^{o,e}/dT$ temperature coefficients which can be found from Ref. [4]

Therefore, the contribution to the phase shift by the refractive index change caused by temperature variation is expressed as below;

$$\Delta\Phi' = \frac{2\pi}{\lambda} \Delta n^{o,e} L \Delta T \qquad (6-6)$$

The length change of the optical waveguide caused by the temperature variation had been investigated by Y. S. Kim & R. T. Smith [7], as well as V. V. Zhdanova, V. P. Klyuev, V. V. Lemanov, I. A. Smirnov and V. V. Tikhonov [8]. The contribution to the phase shift resulted in the length change can be expressed as following;

$$\Delta\Phi'' = \frac{2\pi}{\lambda} n_{eff}^{o,e} L \beta^{o,e} \Delta T \qquad (6-7)$$

where n_{eff} is the effective index of the optical waveguide, L is the length of the waveguide and $\beta^{o,e}$ is the thermal expansion coefficient of the material.

The total phase shift given by the temperature variation is given as:

$$\Delta\Phi = \Delta\Phi' + \Delta\Phi'' = \frac{2\pi}{\lambda} L\Delta T \left(\frac{dn^{o,e}}{dT} + n_{eff}^{o,e} \beta^{o,e} \right) \qquad (6-8)$$

From the above derivation, we can calculate the half wave temperature, the temperature change required by a π phase shift, at the wavelength of 1.15 μm and 0.63 both for TE and TM modes (on Z-cut lithium niobate)

at the wavelength of 1.15 μm for TM mode, the half wave temperature is;

$$\Delta T_{\pi\ (\text{degree})} = \frac{5.1\ ^{\circ}C}{L\ (\text{mm})} \qquad (6-10)$$

at the wavelength of 1.15 μm for TE mode, the half wave temperature is;

$$\Delta T_{\pi\ (\text{degree})} = \frac{7.7\ ^{\circ}C}{L\ (\text{mm})} \qquad (6-11)$$

at the wavelength of 0.63 μm for TM mode, the half wave temperature is;

$$\Delta T_{\pi\ (\text{degree})} = \frac{2.2\ ^{\circ}C}{L\ (\text{mm})} \qquad (6-12)$$

at the wavelength of 0.63 μm for TE mod, the half wave temperature is;

$$\Delta T_{\pi\ (\text{degree})} = \frac{3.4\ ^{\circ}C}{L\ (\text{mm})} \qquad (6-13)$$

6.3 The Experimental Results

In the experiment for testing the temperature sensor, we used the optical set-up shown in Fig. 6.2. It is a multi-function setup used for testing both the intensity variation by measuring the transmitted light, and the phase shift by a bulk Mach-Zehnder interferometer, formed by calibrating the transmitted beam and reference beam reflected by two

extra positioning mirrors to interfere a fringe pattern. The sensor was heated by a Peltier effect heat pump and thermally controlled by a thermistor controlling circuit and read-out by another thermistor as shown in Fig. 6.3.

The resistance variation of a thermistor with the standard resistance of 10 KΩ versus the temperature change around room temperature range has a non-linear response, which is illustrated as Fig. 6.4. By testing the resistance variation of the monitoring thermistor (thermistor 2), we can calculate the temperature change, and the half wave temperature by monitoring the resistance at the turning points for the intensity measurement, or counting the interference fringe movement for the phase shift measurement.

Before depositing the aluminum mirror on the back end of a 15 mm long test sample, we used the the Mach-Zehnder interferometer setup to measure the phase shift variation in the waveguide caused by the temperature change. We tested the interference between the beam transmitted through the device and the reference beam. By counting the fringe movement, the half wave temperature was determined by heating up the device with the heat pump, hence changing the temperature of the sample causing the movement of the interference fringes which were then counted. Therefore, we obtained the tested temperature change vs phase variation at the wavelength of 1.15 μm and 0.63 μm both for TM and TE mode, of which the experimental results are charted in Fig. 6.5.

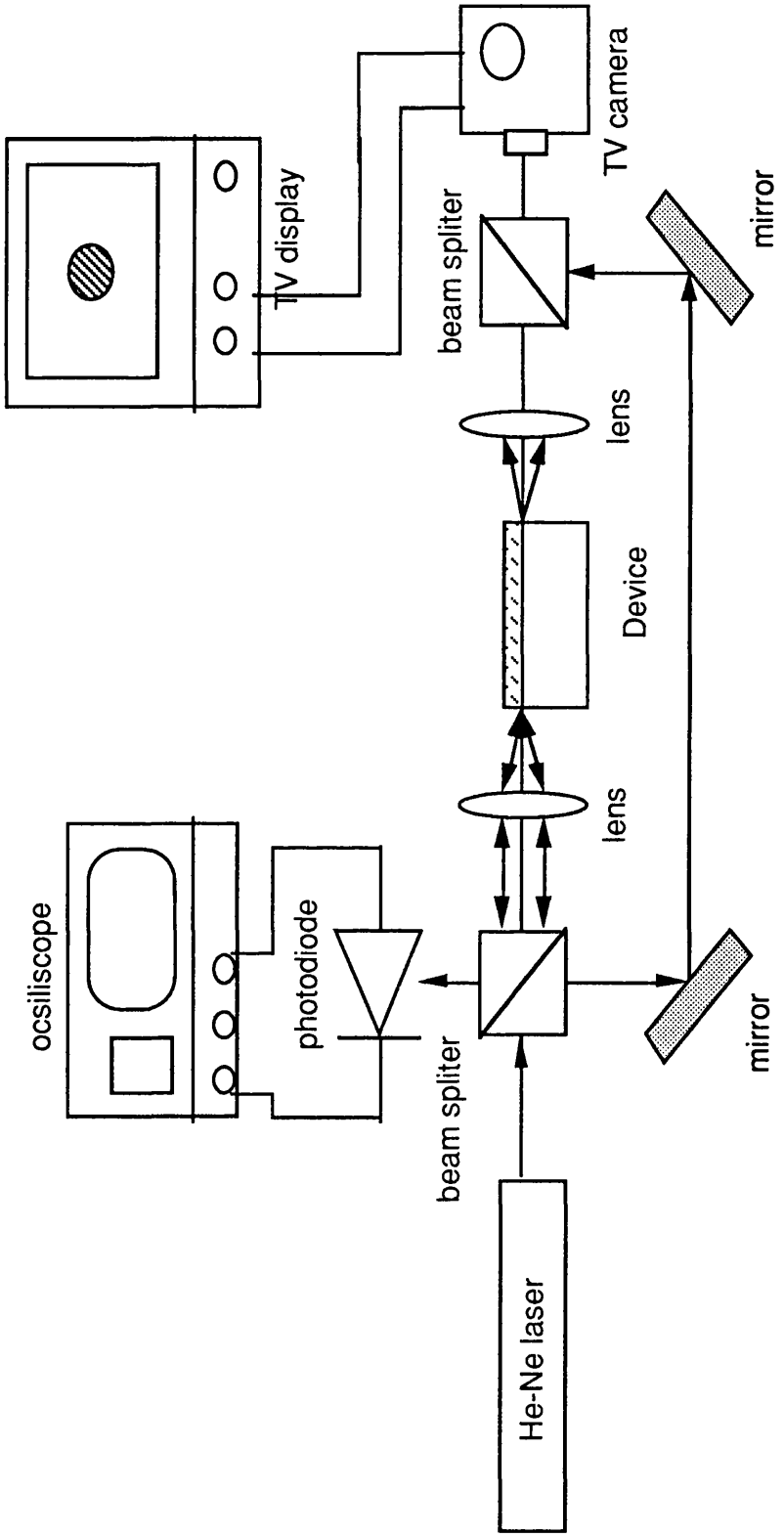

Fig. 6.2 diagram of the optical set-up for integrated optical temperature sensor

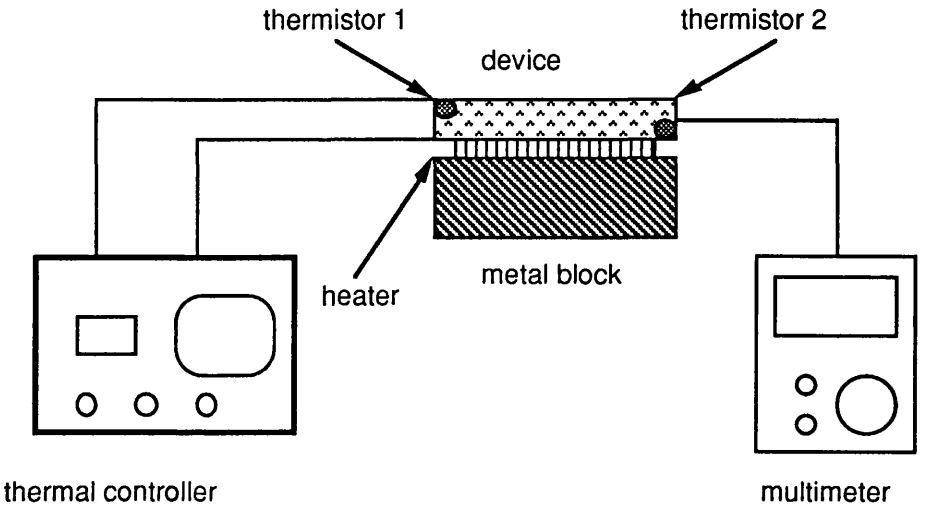

Fig. 6.3 diagram of thermal sensing measurement system

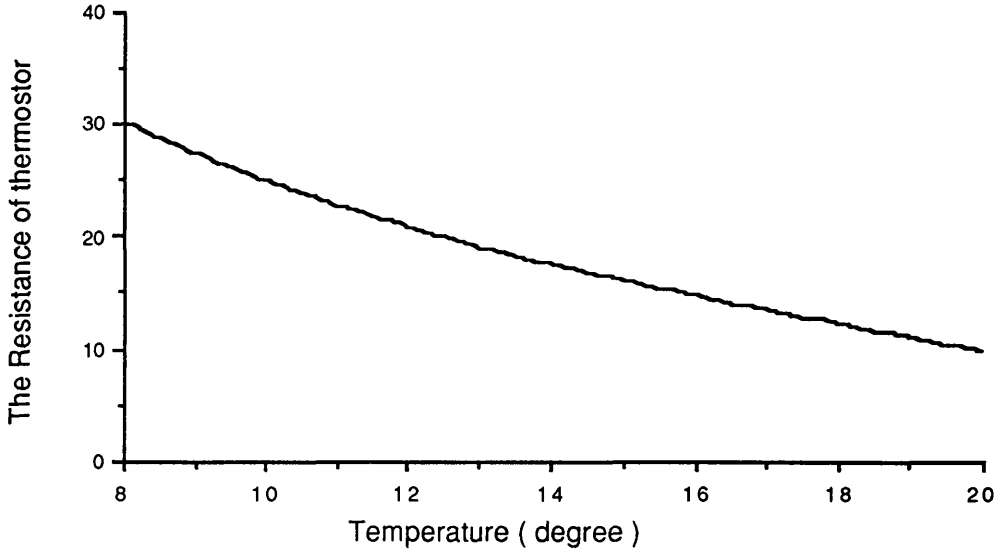

Fig. 6.4 The resistance of thermistor vs temperature

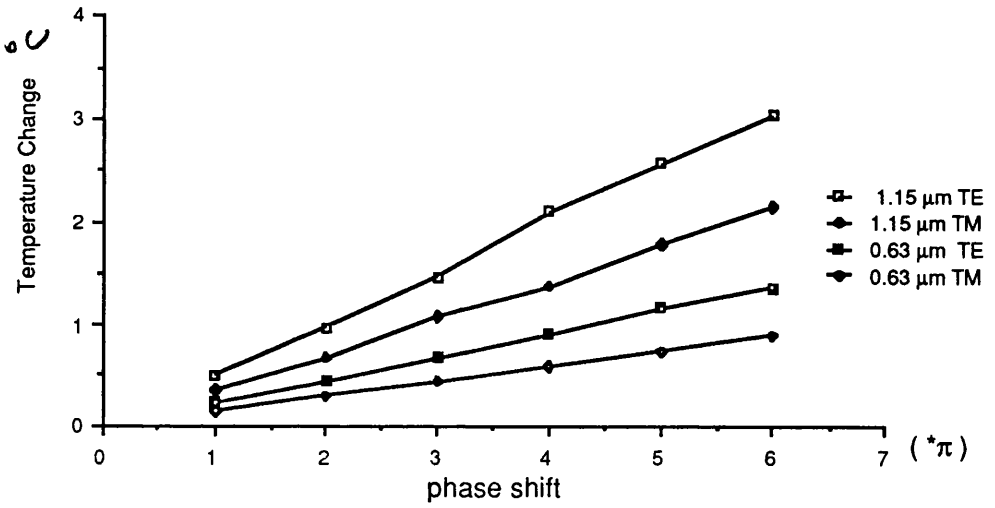

Fig. 6.5 the temperature change ve phase shift for TE and TM mode at 1.15μm & 0.63μm for TE & TM by Mach-Zehnder interferometer

Therefore, we have the half wave temperature of the device as follows;

For TM mode at the wavelength of 1.15 μm, the half wave temperature is 0.42 ^{0}C;

For TE mode at the wavelength of 1.15 μm, the half wave temperature is 1.00 ^{0}C;

For TM mode at the wavelength of 0.63 μm, the half wave temperature is 0.26 ^{0}C;

For TE mode at the wavelength of 0.63 μm, the half wave temperature is 0.40 ^{0}C;.

Subsequently, a 20 nm thin layer of aluminum coating was deposited at the back end on the above sample to form the "Reflecting Mode Integrated Optical Temperature Sensor". By testing the intensity variation of the interference between the Fresnel reflection light from the front end and the mirror reflection from the rear end of the device versus the temperature change, we obtained the half wave temperature of the sensor both for TM and TE modes at wavelength of 1.15 μm and 0.63. The experimental results are as following;

At the wavelength of 1.15 μm for TM mode, the half wave temperature is 0.225^0C. The extinction ratio is 0.76.

At the wavelength of 1.15 μm for TE mode, the half wave temperature is 0.425 ^{0}C. The extinction ratio is 0.66.

At the wavelength of 0.63 μm for TM mode, the half wave temperature is 0.14 ^{0}C. The extinction ratio is 0.51.

At the wavelength of 0.63 μm for TE mode, the half wave temperature is 0.225^0·C. The extinction ratio is 0.36.

Furthermore, Figs 6.6 and 6.7 show the calculated and experimental results of the intensity output vs the temperature change for both TM and TE modes at the wavelength of 1.15 μm. From these results, it can be seen that there is some difference between the theoretical calculations and experimental results. The slight difference of the extinction ratio at the wavelength of 1.15 μm is thought due to the mode mismatch between the wavefront reflected at the front end of the waveguide, which has a Gaussian distribution, and the wavefront reflected from the rear mirror through the optical waveguide which has

a Gaussian & Hermite-Gaussian distribution, as well as the contribution from the size difference of the two modes.

The Figs 6.8 and 6.9 show the calculated and experimental results at the wavelength of 0.63 μm. It can be noticed that the tested extinction ratio is much smaller than the calculated ratio as well. This is mainly decided by the serious mode mismatch between the Gaussian distribution wavefront reflected from the front end and the complex distribution of three modes reflected from the rear end through the waveguide.

It can also also be seen that there is a large difference between the calculated half wave temperature and the experimental result for TM mode at the wave length of 1.15 μm. The similar phenomenon was seen in the bulk Mach-Zehnder measurement as well, although the half wave temperature measured by the reflecting mode method is almost as half as the Mach-Zehnder one, as it passes the waveguide twice in reflecting mode sensor due to the reflection. The reason for the difference is unknown yet, and it is possibly caused by the Ti indiffusion, or by the compositional changing of $LiNbO_3$ as a slight out-diffusion was observed at the wavelength of 0.63 μm, or caused by the non-uniform heat-up of the specimen.

On the whole, the results were summerised in Table 6.1, which listed the calculated and tested half wave temperature, and the extinction ratio at wavelength of 1.15 μm and 0.63 μm both for TE and TM modes. It can also be noticed that the temperature sensitivity for the extraordinary mode is much more pronounced than for the ordinary mode in lithium niobate waveguide, and it is much more sensitive for short wavelength than long wavelength.

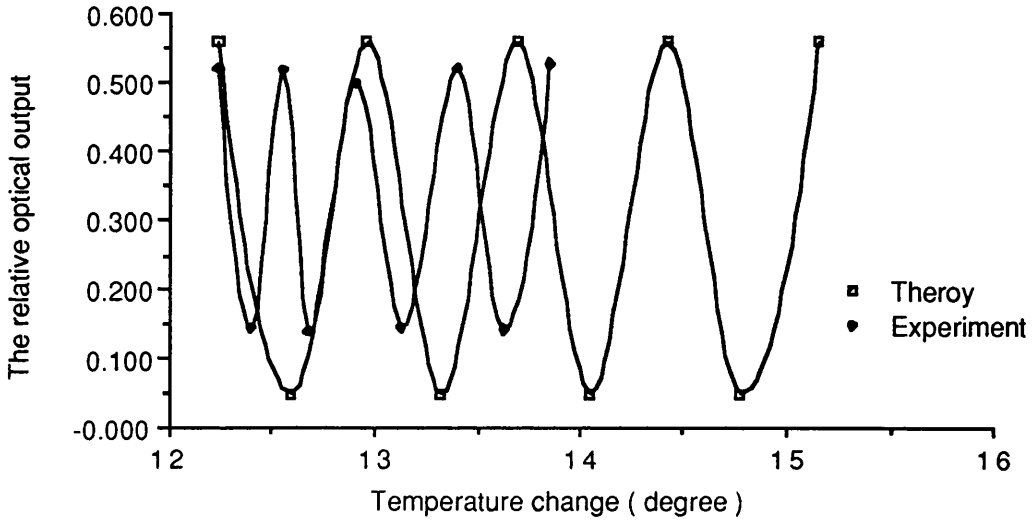

Fig. 6.6 The relative optical output vs temperature change for TM at 1.15μm

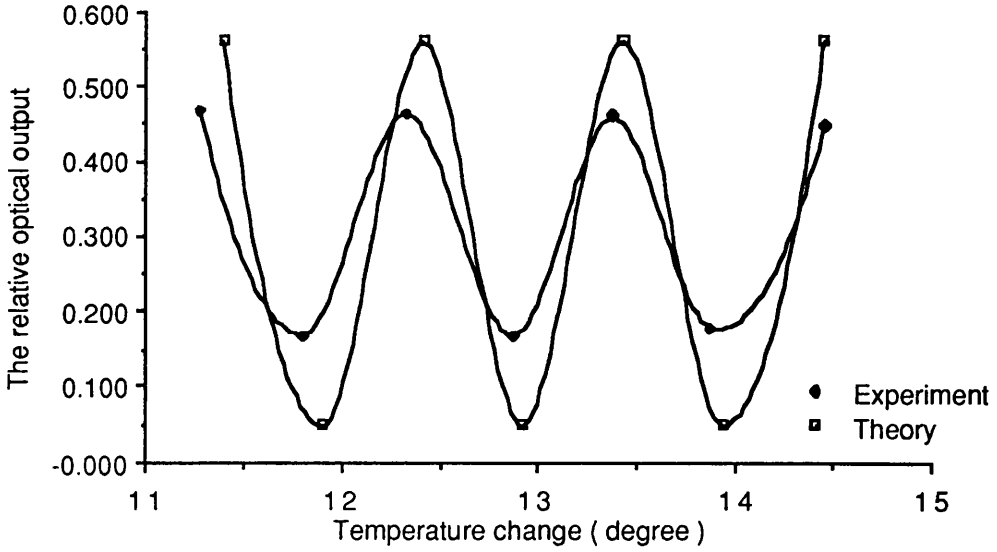

Fig. 6.7 The relative optical output vs temperature change for TE at 1.15μm

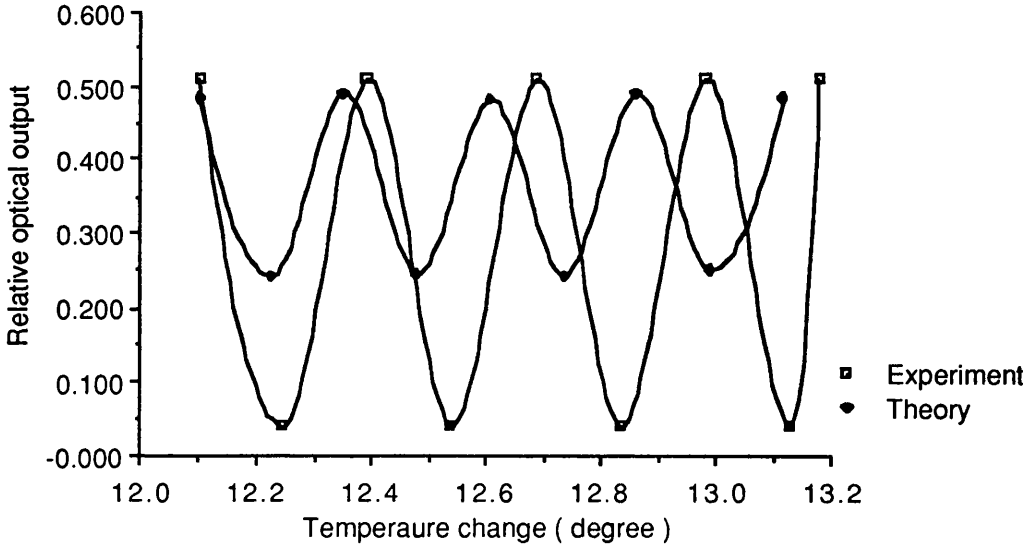

Fig. 6.8 The relative optical output vs temperature change for TM at 0.63μm

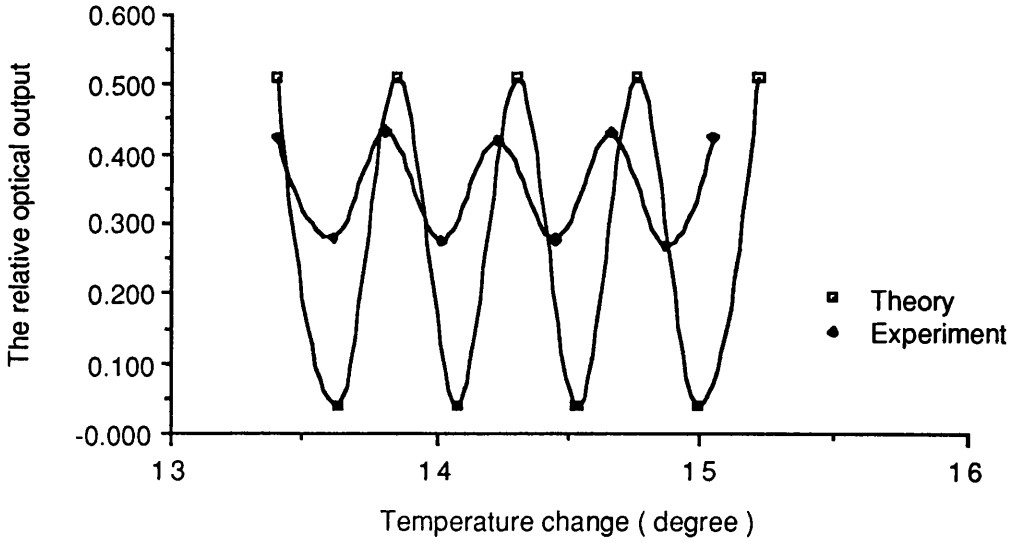

Fig. 6.9 The relative optical output vs temperature change for TE at 0.63μm

Table 6.1

The comparison between the different temperature sensing results

results / group	structure	wavelength	half-wave voltage	on-off ratio
L. M. Johnson et al	multi-unequal arm M-Z Interferometer	0.63 μm	40 C	50 %
M. Haruna et al	π-arc M-Z interferometer	0.63 μm	0.3 C	50 %
M. Izutsu et al	reflecting M-Z interferometer	0.82 μm	0.32 C	30 %
J. Y. Liang et al [1]	reflecting mode	1.15 μm	0.225 C	76 %
J. Y. Liang et al [2]	reflecting mode	0.63 μm	0.140 C	51 %

Furthermore, the slight difference between the calculated and tested half wave temperatures is possibly due to the indiffusion of titanium into the lithium niobate substrate to form the optical waveguide, or the inaccuracy of the measurement.

6.4 Conclusion

In this chapter, we have investigated the temperature sensitivity of a single straight waveguide in a lithium niobate substrate, while treating

it as a temperature sensor, called as the "reflecting mode integrated optical temperature sensor ". As a temperature sensor, it has a simple structure, small heat capacity, high sensitive and good extinction ratio compared with other Mach-Zehnder integrated optical temperature sensors. Moreover, it could be made in a very small volume for very sensitive measurements on the temperature distribution, as the thermal capacity of the sensor is very small.

Nevertheless, the sensitivity to the temperature variation will degrade the performance of optical modulation when we use the similar structure for a modulator, e.g. the Fabry-Perot integrated optical modulator, and even make it unsuitable to use in practice, so that the temperature controlling is the key point in Fabry-Perot modulation.

From the experimental results in this chapter, the product of the half wave temperature and the length of the waveguide is 0.338 ^{0}C×cm for TM mode and 0.638 ^{0}C×cm for TE mode at the wavelength of 1.15 μm on Z-cut $LiNbO_3$. Obviously, the temperature sensitivity on extraordinary mode is much more sensitive than ordinary mode, while we use the extraordinary mode in a optical modulator on lithium niobate material in order to get the maximum available modulation efficiency. In this experiment, we found that the temperature of the testing sample can be kept in range of 0.01 ^{0}C without difficulty, by a Peltier effect heat pump controlled by a thermistor circuit, so we can use it to control the temperature variation of the Fabry-Perot integrated optical modulator.

6.5 Reference

[1] L. M. Johnson and F. J. Leonberger, "Intergrated Optical Temperature Sensor", Appl. Phys. Lett. Vol. 41, No. 2, July,1982.

[2] M. . Haruna, H. Nakajima and H. Nishihara, " Optical π-Arc Waveguide interferometer In Proton-Exchange $LiNbO_3$ for temperature sensing ", Applied Optics, Vol. 24, No. 16, August, 1985.

[3] M. Izutsu, A. Enokihara and T. Sueta, " Integrated Optic Temperature And Humidity Sensors ", J. Lightwave Tech., Vol. LT-4, No. 7, July, 1986.

[4] G. D. Boyd, W. L. Bond and H. E. Carter, " Refractive Index as a Function of Temperature in $LiNbO_3$ ", J. Applied Physics, Vol. 38, No. 4, March, 1967.

[5] H. Iwasaki, H. Toyoda and N. Niizeki, " Dispersion of The Refractive Indices of $LiNbO_3$ Crystal Between 20 and 900 C^0 ", Japanise J. of Applied Physics, Vol.6, No. 9, Sept. 1967.

[6] R. S. Longhurst, " Geometrical and Physical Optics ", Longman Group Limited, Third Edition, London, 1973.

[7] Y. S. Kim and R. T. Smith, " Thermal Expansion of and Lithium Tantalate Lithium Niobate Single Crystals ", J. Applied Physics, Vol. 40, No. 11, Oct. 1969.

[8] V. V. Zhdanova, V. P. Klyuev, V. V. Lemanov, I. A. Smirnov and V. V Tikhonov, " Thermal Properties of Lithium Niobate Crystals ", Vol. 10, No. 6, Dec. 1968.

CHAPTER 7 THE MULTIPLE TRANSMISSION PROPERTIES OF FABRY-PEROT OPTICAL MODULATOR

7.1 Introduction

For a Fabry-Perot optical modulator, the complicated modulation properties are decided by the multiple transmission of the Fabry-Perot cavity, as well as the optical beam is modulated both forward and backward by the electrodes. When the optical beams multi-pass in the cavity, the frequency response of a Fabry-Perot modulation is a periodic function of the self resonant frequency of the cavity and its bandwidth is decided by the reflectivity of the mirror and the length of the cavity[1]. Meanwhile, the velocity mismatches between the electrical signal and optical wave for both forward and backward are taking into account, and they are n_0-n_m for forward transmission and $n_0 + n_m$ for backward transmission (n_0 and n_m are the optical index and microwave index). The cut-off frequency of the Fabry-Perot modulation will be limited by the electrode structure[2]. Therefore, there are complicated relations between the modulation bandwidth, the driving power and the optical losses of the modulator which are decided by the length of the optical cavity, the length of the electrodes, the reflectivity of the ~~of the~~ cavity, the conducting loss on the electrodes and the optical losses in the waveguide. Among all the parameters of the modulator, the reflectivity of the cavity plays a dominant role to the modulator, the higher the reflectivity, the lower the driving power, the narrower the modulation bandwidth, the greater the maximum available modulation depth and the more lossy the optical output. Meanwhile, other parameters also have a lot of influence on Fabry-Perot modulation properties, which will be discussing in this chapter as well.

To make the analysis simple, we consider the two factors separately,

one is the double transit which consists of a forward transmission and a backward one, the other is the multiple transmission which is the superposition of the every single transit loop. We find that the cut-off modulation frequency of a Fabry-Perot modulator is mainly decided by the single loop of both the forward and backward transmission properties and the modulation frequency response is decided by the multiple transmission properties which is a periodic function of the self resonant frequency of the Fabry-Perot cavity. Therefore, we can calculated the whole modulation characteristics of the Fabry-Perot modulator by combining the two factors together, and find that the reflectivity of the cavity plays the dominant role among the all the parameters of the modulator.

7.2 The Double Transmission Properties of Fabry-Perot Modulation

For the double transmission of Fabry-Perot modulation, we only consider the forward and backward transmissions in a single loop inside the cavity to work out the modulation cut-off frequency upon the parameter of the modulator.

let

$$P = \frac{\pi \gamma \Gamma n_0^3 V}{\lambda G} \qquad (7-1)$$

where P is called phase shift factor, n_0 is the optical index of the cavity, V is the applied voltage across the electrodes, G the gap of the electrodes, λ the wavelength of the optical wave in the cavity, γ the electro-optical coefficient of the crystal, Γ the over-lap coefficient of the electrical field and the optical wave which was defined in chapter 3.

The phase shift of optical cavity can be divided by two parts due to the multiple transmission properties; one is the forward phase shift when

the optical beam is travelling in the same direction as the modulating microwave signal, the other is the backward phase shift when the optical beam is travelling in the opposite direction to the microwave signal. The whole phase shift which contributes to the Fabry-Perot cavity is the combination of both forward and backward phase shifts.

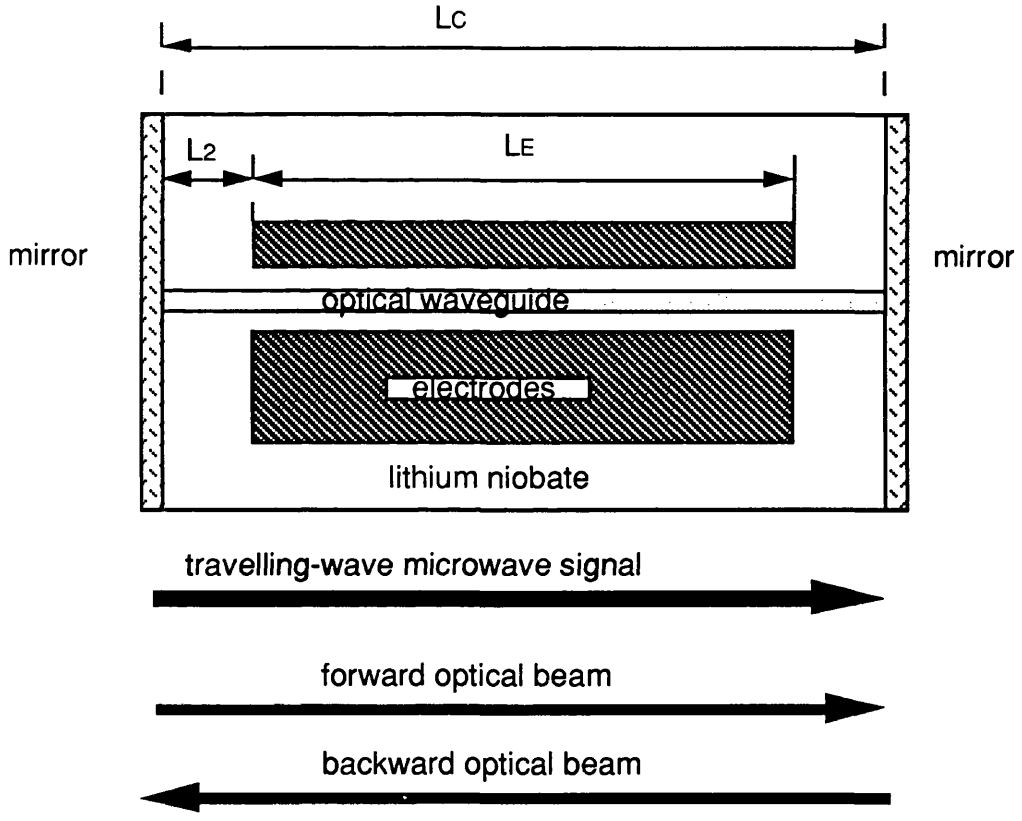

Fig. 6.1 Diagrammatic presentation of a Fabry-Perot Modulator

First, the forward phase shift is defined as;

$$\phi^{*}_{for} = P\int_{L_2}^{L_E+L_2} \exp\{ -\alpha Z + [\omega_m (t - t_1) - K_m Z] j \} dZ$$

(7 - 2)

where $t = Z/ V_0$, $K_m = 2\pi/\lambda_m = \omega_m/V_E$, which V_0 and V_E are the optical wave and microwave velocities in the optical cavity, λ_m and ω_m the microwave wavelength and angular frequency, K_m the space vector of the microwave. L_E is the length of the electrodes and L_2 is the distance between the start of the optical cavity to the start of the electrodes as shown in Fig. 6.1.

let

$$\Delta^{-} = \frac{1}{V_E} - \frac{1}{V_O} = \frac{n_m - n_o}{C}$$

(7 - 3)

where C is the speed of light, and n_0 and n_m are the optical and microwave index

$$\Phi_{for} = \int_{L_2}^{L_E+L_2} \exp\{ -\alpha z + [\omega_m (t - t_1) - K_m Z] j \} dZ$$

$$= \frac{\exp[-\alpha L_2 - \omega_m (L_2 \Delta^{-} + t_1) j] \times [\exp(-\alpha L_2 - \omega_m L_E \Delta^{-} j) - 1]}{-\alpha - j\omega_m L_E \Delta^{-}}$$

(7 - 4)

as

$$-\alpha - \omega_m \Delta^- j = \sqrt{\alpha^2 + \omega_m^2 (\Delta^-)^2}\ \exp(\theta_1 j) \qquad (7-5)$$

where

$$\theta_1 = \tan^{-1}\frac{\omega_m \Delta^-}{\alpha} + \pi \quad \text{and} \quad \theta_1 = \frac{3\pi}{2} \quad \text{when} \quad \alpha = 0 \qquad (7-6)$$

while

$$\exp(-\alpha L_E - \omega_m \Delta^- L_E j) - 1$$

$$= \sqrt{1 + \exp(-2\alpha L_E) - 2\cos(\omega_m \Delta^- L_E)\exp(-\alpha L_E)}\ \exp(\gamma_1 j) \qquad (7-7)$$

where

$$\gamma_1 = \tan^{-1}\frac{\sin(\omega_m \Delta^- L_E)\exp(-\alpha L_E)}{1 - \cos(\omega_m \Delta^- L_E)\exp(-\alpha L_E)} + \pi \qquad (7-8)$$

which

$$\gamma_1 = \tan^{-1}\frac{\sin(\omega_m \Delta^- L_E)}{1 - \cos(\omega_m \Delta^- L_E)} = -\frac{1}{2}\omega_m \Delta^- L_E + \frac{3\pi}{2} \quad \text{when } \alpha = 0 \qquad (7-9)$$

therefore,

$$\Phi_{for} = \exp(-\alpha L_2)\sqrt{\frac{1+\exp(-2\alpha L_E)-2\exp(-\alpha L_E)\cos(\omega_m \bar{\Delta} L_E)}{\alpha_2 + \omega_m^2(\bar{\Delta})^2}}$$

$$\exp\{[\omega_m(t_1 + \bar{\Delta} L_2) - \gamma_1 + \theta_1]\, j\} \qquad (7-10)$$

In the same way, we have the phase shift of contra-direction travelling,

$$\Phi_{back} = \int_{L_2+L_E}^{L_2} \exp\{-\alpha z + [\omega_m(t - t_2) - K_m Z]\, j\}\, d(-Z) \qquad (7-11a)$$

let

$$\Delta^+ = \frac{1}{V_E} + \frac{1}{V_O} = \frac{n_m + n_o}{C} \qquad (7-12)$$

$$t = \frac{2L_C - Z}{V_0}$$

where L_C is the length the cavity.

$$= \frac{\exp\{-\alpha L_2 - [\omega_m(t_2 + \Delta^+ L_2 - \frac{2L_C}{V_0})j]\}}{-\alpha - \omega_m \Delta^+ j}\,[\exp(-\alpha L_E - \omega_m \Delta^+ L_E) - 1] \qquad (7-11b)$$

So

$$-\alpha - \omega_m \Delta^+ j = \sqrt{\alpha^2 + \omega_m^2 (\Delta^+)^2}\ \exp(\theta_2 j) \qquad (7-13)$$

where

$$\theta_2 = \tan^{-1}\frac{\omega_m \Delta^+}{\alpha} + \pi \quad \text{and} \quad \theta_2 = \frac{3\pi}{2} \ \text{when} \ \alpha = 0 \qquad (7-14)$$

as well,

$$\exp(-\alpha L_E - \omega_m \Delta^+ L_E j) - 1$$

$$= \sqrt{1 + \exp(-2\alpha L_E) - 2\cos(\omega_m \Delta^+ L_E)\exp(-\alpha L_E)}\ \exp(\gamma_2 j) \qquad (7-15)$$

where

$$\gamma_2 = \tan^{-1}\frac{\sin(\omega_m \Delta^+ L_E)\exp(-\alpha L_E)}{1 - \cos(\omega_m \Delta^+ L_E)\exp(-\alpha L_E)} + \pi \qquad (7-16)$$

and

$$\gamma_2 = \tan^{-1}\frac{\sin(\omega_m \Delta^+ L_E)}{1 - \cos(\omega_m \Delta^+ L_E)} = -\frac{1}{2}\omega_m \Delta^+ L_E + \frac{3\pi}{2} \ \text{when} \ \alpha = 0 \qquad (7-17)$$

$$\Phi_{back} = \exp(-\alpha L_2)\sqrt{\frac{1+\exp(-2\alpha L_E) - 2\exp(-\alpha L_E)\cos(\omega_m \Delta^+ L_E)}{\alpha^2 + (\omega_m \Delta^+)^2}}$$

$$\exp\{-[\omega_m(t_1 + \Delta^+ L_2 - \frac{2L_C}{V_0}) - \gamma_2 + \theta_2]\, j\} \qquad (7-18)$$

So, the total phase shift for a double transmission is:

$$\Phi^* = P\Phi_{for} + P\Phi_{back} \qquad (7-19)$$

let

$$\exp(-\alpha L_2)\sqrt{\frac{1+\exp(-2\alpha L_E) - 2\exp(-\alpha L_E)\cos(\omega_m L_E \Delta^-)}{\alpha^2 + (\omega_m \Delta^-)^2}} = A^-$$

$$\exp(-\alpha L_2)\sqrt{\frac{1+\exp(-2\alpha L_E) - 2\exp(-\alpha L_E)\cos(\omega_m L_E \Delta^+)}{\alpha^2 + (\omega_m \Delta^+)^2}} = A^+$$

(7-20 a, b)

and

$$\omega_m \Delta^- L_2 - \gamma_1 + \theta_1 = \Psi_1 \qquad (7-21)$$

$$\omega_m \Delta^+ L_2 - \gamma_2 + \theta_2 + \frac{2L_C}{V_0} = \Psi_2 \qquad (7-22)$$

we get the phase shift coefficient Φ as following;

$$\Phi = \Phi_{for} + \Phi_{back}$$

we get

$$\Phi = [\, A^- \exp(-\Psi_1 j) + A^+ \exp(-\Psi_2 j)\,] \exp(-\omega_m t_1 j) \qquad (7-23)$$

$$\phi = [\, A^- \exp(-\Psi_1 j) + A^+ \exp(-\Psi_2 j)\,]$$

$$= A^- \cos\Psi_1 + A^+ \cos\Psi_2 - j(A^- \sin\Psi_1 + A^+ \sin\Psi_2)$$

$$= \sqrt{(A^-)^2 + (A^+)^2 + 2A^-A^+\cos(\Psi_2 - \Psi_1)}\exp(\Psi' j) \qquad (7-24)$$

where

$$\Psi' = -\arctan\frac{A^-\sin(\psi_1) + A^+\sin(\psi_2)}{A^-\cos(\psi_1) + A^+\cos(\psi_2)} \qquad (7-25)$$

at lossless condition, we have,

$$A_0^- = \frac{\sin(\frac{1}{2}\omega_m\Delta^- L_E)}{\frac{1}{2}\omega_m\Delta^-} = L_E\mathrm{sinc}(\frac{1}{2}\omega_m\Delta^- L_E) \qquad (7-26a)$$

$$A_0^+ = \frac{\sin(\frac{1}{2}\omega_m\Delta^+ L_E)}{\frac{1}{2}\omega_m\Delta^+} = L_E\mathrm{sinc}(\frac{1}{2}\omega_m\Delta^+ L_E) \qquad (7-26b)$$

$$\Delta\psi = \psi_2 - \psi_1 = \frac{2L_C - L_E - 2L_2}{V_0}\omega_m \qquad (7-27)$$

then, the maximum available phase shift for a double transmission in Fabry-Perot cavity, when $\Delta\psi = 2n\pi$, is given as;

$$\Phi_{max} = PL_E\mathrm{sinc}(\frac{1}{2}\omega_m\Delta^- L_E) + PL_E\mathrm{sinc}(\frac{1}{2}\omega_m\Delta^+ L_E) \qquad (7-28)$$

In order to get high frequency modulation for Fabry-Perot modulator, we can set up the modulator structure at the condition of $\Delta\psi=2n\pi$, if we put the electrodes in the middle of the cavity, then we have;

$$f_m = n \frac{V_0}{L_C} \qquad (7-29)$$

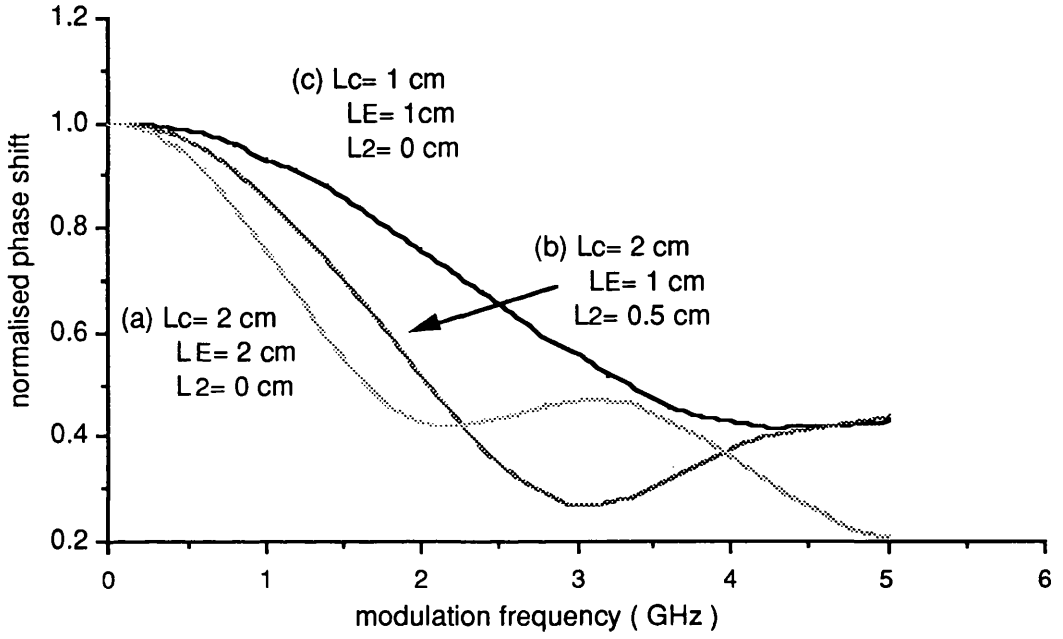

Fig. 7.2 Normalised phase shifts of a double transmission in Fabry-Perot cavity for different constructures versus the modulation frequency

we can realise that to obtain the maximum available phase shift for a double transit, the modulation frequency must be an integer multiple of the resonant frequency of the optical cavity;

$$f_R = m \frac{V_0}{2L_C} \qquad (7-30)$$

However at very high frequency, the modulation efficiency gets

degraded because the velocity mismatch between the optical wave and the electrical signal. Therefore, we must use the special technique to overcome this problem, such as "phase reversal electrodes" [3] and "the artificial transmission lines" [4].

From above results, we can simulate the frequency response for different electrodes and the frequency response on a double transit is illustrated in Fig. 7.2. We noticed that the longer the optical resonator, the the lower the cut-off frequency as the cut-off frequencies are 1.5 GHz for 2cm long cavity with 1 cm long electrodes and 2.2 GHz for 1cm long cavity with 1 cm long electrodes; the longer the electrodes, the lower the cut-off frequency as the cut-off frequencies are 1 GHz for 2 cm long electrodes on a 2 cm long cavity and 1.5 GHz for 1 cm long electrodes on a 2 cm long cavity. For a Fabry-Perot optical modulator of 2 cm long with 1 cm long electrodes, the cut-off frequency limited by the double transit is around 1.5 GHz.

7.2 The modulation bandwidth limited by the multi-transit of the Fabry-Perot cavity

In a Fabry-Perot optical modulator, the modulation frequency response is not only limited by the forward and backward interactions between the electrical signal and optical wave which cause velocity mismatches, but also influenced by the multiple transmission of the optical resonant cavity because the interaction between the electrical signal and individual optical transit beam is not keeping in phase due to the transit time of each transmission beam in the cavity at a high modulation frequency.

In order to simulate the frequency response of the resonant modulation, we have to make some approximations for simplicity; the diagram of the simplified Fabry-Perot resonant cavity assumes that the electrodes in the middle of the cavity are short enough to cause no velocity

mismatch between the electrical signal and optical wave, the transit time through the electrodes is small enough to neglect compared to the resonant transit time, and there is no optical loss in the cavity. We have the expression for each individual transmitted beam;

the first transmitted beam E_1 is;

$$E_1 = t_1 t_2 E_0 \exp\left[-j(A_0 + A_1)\right] \qquad (7-31)$$

where E_0 is the amplitude of incident beam, t_1 and t_2 are the transmission coefficients at the front and rear ends of the cavity, A_0 is the phase shift constant of the cavity and A_1 is the phase shift provided by the electrodes. The individual transmitted beam can be expressed as following;

$$E_2 = t_1 t_2 r_1 r_2 \exp[-j(3A_0 + A_1 + A_2)] \qquad (7-32)$$

$$E_i = E_0 t_1 t_2 (r_1 r_2)^{i-1} \exp\left[-j\{(2i-1)A_0 + \sum_{k=1}^{i} A_k\}\right] \qquad (7-33)$$

$$E_{i+1} = E_0 t_1 t_2 (r_1 r_2)^{i} \exp\left[-j\{2i+1)A_0 + \sum_{k=1}^{i+1} A_k\}\right] \qquad (7-34)$$

which can be simplified as

$$E_{i+1} = E_i r_1 r_2 \exp\left[-j(2A_0 + A_{i+1})\right] \qquad (7-35)$$

where r_1 and r_2 are the reflectivity at the front and rear ends, A_i is the phase shift at the ith pass through the electrodes and it can be expressed as;

$$A_i = P\cos[\omega_m(\tau - \tau_i)] \qquad (7-36)$$

where P is the peak phase shift caused by the electrodes, ω_m is the angular frequency of the electrical signal and τ_i is the resonant transit time of the ith transmitted beam in the cavity which can be expressed as;

$$\tau_i = \frac{2L_c n_{eff} i}{c} \qquad (7-37)$$

From Equ. 7-36, we noticed that the phase shift of each transit beam is a periodic function and its period is the self resonant frequency of the optical cavity given as;

$$f_o = \frac{C}{2L_C n_{eff}} \qquad (7-38)$$

The summary of the each individual transmitted beam is expressed as;

$$E_t = \sum_{i=1}^{\infty} E_i \qquad (7-39)$$

The optical intensity output which is the function of modulation frequency can be expresses as;

$$I_{out}(f, \tau) = E_t \times E_t^* \qquad (7-40)$$

As the intensity output of the Fabry-Perot modulation is the

superimposion of the each individual transit beam, the frequency response of the Fabry-Perot modulation will be a periodic function of the self resonant frequency of the optical cavity as well according Equs (7-37) and (7-38). Because of the complication of the modulation characteristics of the resonant cavity, numerous simulation was used to calculate the frequency response of the Fabry-Perot modulation

Therefore, a small signal method was used to calculate the modulation bandwidth, of which we can plot the output variation $I_{out}(f)$ versus modulation frequency f by a very small phase shift $\Delta\phi$ at a proper bias point.

$$\Delta I_{out}(f) = \frac{\partial I_{out}(f)}{\partial f} \Delta\phi \qquad 7-41$$

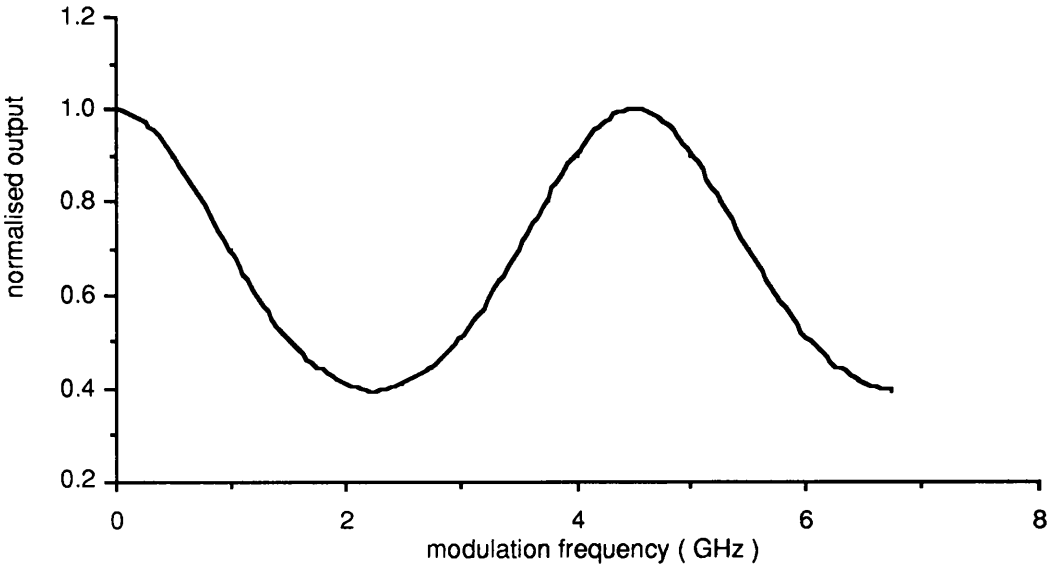

Fig. 7.3 The calculated output vs the modulation frequency for a 1.5 cm long Fabry-Perot modulator with 50% reflectance mirrors

The modulation efficiency versus the modulation frequency was obtained from the above equation for a 1.5 cm long Fabry-Perot modulator with reflectance of 50%, which is shown in Fig.7.3. We notice that the modulation efficiency is exactly a periodical function of the resonant frequency of the optical Fabry-Perot cavity as discussed previously, which is 4.55 GHz for a 1.5 cm long cavity in lithium niobate substrate, and the modulation bandwidth based on the resonant frequency is mainly decided by the reflectivity of the cavity mirrors and the resonant frequency[1]. From the Fig. 7.3, we have the 3-dB modulation bandwidth for the fundamental order which is about 1 GHz while for the high order it is about 2 GHz.

7.4 Conclusion

From above discussion,we have analysed the frequency response of the Fabry-Perot modulation separately. Its cut-off frequency is decided by the velocity mismatching for forward and backward transmission, and 'tuned' by the periodic response due to the multiple transmission beams of the cavity. For a double transit which consists of a forward and backward transmission, the cut-off frequency is decided by the length of the optical cavity, the length of the electrodes and the structure of the electrodes; while for the multiple transmission effect, the frequency response is the function of the optical resonating frequency which depends on the length of the cavity and the bandwidth is decided by the reflectivity of the mirrors and the length of cavity. Therefore, we can work out that the bandwidth of the optical Fabry-Perot modulator is mainly decided by the electrode structure and tuned by the multiple transmission effect. Although the optical losses in the cavity gives some influence to the modulation bandwidth, we can take it into account by the effective reflectivity calculation which will be discussed in next chapter.

7.5 Reference

[1]. E. I. Gordon and J. D Rigden, "The Fabry-Perot Electrooptic Modulator", The Bell Technical Journal, pp. 155 - 179, Jan., 1963.

[2]. M. M. Stallard, D. Erasme and M. G. F. Wilson, "Design consideration and analtsis of Velocity Mismatch Effects in an Electrooptic Fabry-Perot modulator", Optics Communication, Vol. 55, No. 5, pp 316-318, Oct. 1985.

[3]. D. Erasme and M. G. F. Wilson, "Analysis and Optimation of Integrated-optic Travelling-wave Modulator Using Peridic and Non-peridic Phase Reversals", Optical and Quantum Electronics, Vol. 18, pp-203, 1986.

[4]. C. S. Aitchison, "The Use of Micowave Artificial Transmission Line in Optical Modulators and Demodulators", Communication Reprints, July, 1991.

CHAPTER 8 DEVICE FABRICATION & EXPERIMENTAL RESULTS

8.1 Introduction

Integrated optical Fabry-Perot modulators have been investigated by several groups as a novel approach to high speed modulation, because of their simplicity, low driving power and the possibility of very high speed modulation [1]. Stewart *et al* fabricated a symmetrical, electro-optical tunable Ti: $LiNbO_3$ channel waveguide resonator, which allowed modulating a light beam with a extremely low voltage of 320 mV for a modulation depth of 84% at the wavelength of 0.63 μm [2]. Bruland *et al* designed an asymmetric reflection mode integrated optical Fabry-Perot modulator, and achieved a modulation depth of 84% by a driving voltage of 1.7 V only at the wavelength of 1.52 μm [3]. Herrmann developed the asymmetric reflection mode integrated optical Fabry-Perot modulator by reducing the driving voltage of 84% modulation to 0.9 V, and obtained a modulation bandwidth of 270 MHz [4].

In this chapter, we investigate the characteristics of a symmetric integrated optical Fabry-Perot modulator using a slightly low reflection optical resonator to reduce the optical transmission losses and to increase the modulation bandwidth.

8.2 Device Design Consideration

In the previous chapters, the different elements and characteristics of a high speed integrated optical Fabry-Perot modulator have been discussed separately; the optical waveguides were analysed in chapter 2, the travelling-wave electrodes were considered in chapter 3, the high reflective dielectric coating was studied in chapter 4, the DC

characteristics of the Fabry-Perot optical resonator were investigated in chapter 5, the temperature sensitivity of the resonant modulator was demonstrated in chapter 6 and the modulation frequency response due to the multiple transit in the optical resonator was simulated in chapter 7. In this section, the previous results are summarised and considered for the design of an experimental device.

The light source used in the experiment is an HeNe laser emitting at the wavelength of 1.15 μm as the wavelength of 0.63 μm was found undesirable because of the optical damage in the optical waveguides, while other kinds of lasers available for us are not good enough at the optical coherent length which is critical for a Fabry-Perot optical resonator.

In order to fulfill the strong electro-optic coefficient of lithium niobate (r_{33}) in the interaction between the electrodes and optical waveguide, Y-cut crystal must be used to deploy the TE mode guiding so that the optical waveguide can be placed in the middle of the electrodes, because the overlaying of the electrodes on the optical waveguide would cause considerable extra optical losses which degrade the modulation performance seriously.

One of the basic requirements of the resonant modulator is a single-moded optical waveguide: in a multi-moded waveguide, the modulation characteristics are different for each mode because of the difference in the propagation constants and the resonant moding in the cavity. Moreover, the straight waveguide must be extremely perpendicular to the polishing edges on which the mirrors will be deposited, otherwise, a large amount of extra optical loss will be introduced to the optical resonator.

Due to the resonant modulation of the Fabry-Perot optical

modulator, the performance of the modulation is not only decided by the length and structure of the electrodes, like a Mach-Zehnder modulator, but also decided by length of the optical resonator, reflectivity of the mirrors and loss coefficient of the waveguide. Theoretically, the higher the reflectivity of the resonator mirrors, the lower the electrical driving power, but the narrower the modulation bandwidth. Moreover, the optical insertion loss of the modulator will become very significant if there is optical loss in the cavity media; for example, the Bruland et al [3] calculated that the peak transmission of a 4 cm long waveguide resonator with mirrors of 99% reflectivity and waveguide loss of 0.1 dB/cm is only 1%, equivalent to a minimum insertion loss (without coupling losses) of 20 dB. Although Fabry-Perot modulation is a narrow bandwidth which is decided by the reflectivity of the mirrors and the length of the cavity, the response of the modulation frequency is a periodical function of the self-resonant frequency of the Fabry-Perot cavity and limited by the cut-off frequency of the electrodes.

In order to obtain a reasonably good modulation, we have to make a trade-off between the modulation bandwidth, electrical driving power and total insertion losses by selecting the reflectivity of the resonator mirrors, the length of the cavity and the length of the electrodes. For the experimental device, we consider the modulator to have 82% reflectance ($R = r^2$) of the mirrors, cavity length of 1.5 cm and electrode length of 1 cm, meanwhile, to reduce the optical losses of the waveguide as low as possible.

8.3 Device Fabrication

The experimental device was fabricated, as discussed previously, in the Clean Room, U.C.L. by standard photolithography techniques.

First, the lithium niobate substrates were obtained from a Y-cut optical grade wafer, which was cut into required the dimension of 2.2 cm (X) by 1 cm (Z) using a diamond blade.

Then, the optical waveguides were fabricated on the lithium niobate substrates by the modified indiffusion method, in which the titanium strips, 6 μm wide and 75 nm thick, were diffused at a temperature of 1050 ^{o}C for 10 hours. Single mode waveguides without any out-diffusion at 1.15 μm were achieved, and the total insertion losses were less than 4.5 dB for the TE mode. The straight waveguides were aligned parallel to the reference edge of substrate which is essential to form the resonant cavity in late stages. The waveguides which had good propagation characteristics was selected as the final devices.

The next step is the deposition of the travelling-wave electrodes. In order to reduce the optical loss caused by loading electrodes, the gap of the electrodes was chosen to be 8 μm wide, 2 μm wider than the width of the optical waveguide and the width-to-gap ratio of the electrodes was set to 1 (the impedance of the electrodes is around 45 Ω) which gave a 8 μm wide conducting electrode to reduce the electrical losses of the electrodes. At the ends of the electrodes, some reference lines was set-up as well, which helped to monitor the wedge angle of the resonator. Subsequently, the device was treated as a phase modulator and tested by the experimental set-up shown in Fig. 8.2. By counting the fringe movement, the halfwave voltage was achieved with 5.5 V only.

The following is the end-face preparation for the optical cavity. For end-fire coupling into the waveguide, carefully polished end faces are essential to ensure the a low coupling loss. Moreover, the end faces should be very perpendicular to the optical waveguide and parallel to each other to form a good waveguide resonator. By aligning the reference edge of the substrate to the reference line of the polishing jig,

the wedge angles of the waveguide resonator was ensured less than 0.1° which was measured by the substrate reference lines. Two small cover plates of lithium niobate were bonded by UV-cured epoxy to the substrate with very small gaps (less than 1 μm), to avoid rounding of the end surfaces, moreover, the coating of the guiding areas of the end faces will not be degraded. After the polishing, the losses of the optical waveguide were tested by the thermal resonator method again, and a single pass loss was 1.47 dB.

Finally, it is the depositing of high reflectivity mirrors. The mirrors were deposited having total 5 layers of Zinc Sulphide and Cryolite in an alternative quarter-wave stack, of which the reflectance (R) is around 80% on lithium niobate substrate. The end faces were pre-cleaned and checked by microscope before the coating, plasma-cleaned during the coating evaperation. The coating was monitored on a glass slide which was tested by a monochromator for reflectivity spectrum to ensure the quality of the mirrors. At last, the device was made ready for measurement as shown in Fig. 8.1

8.4 The Experimental Set-up

The measurement of high frequency modulation with high speed response photo-diode circuit was established by a multi-function set-up, which is illustrated in Fig. 8.2. It was shown to be a convenient method for the measurement of both intensity modulation and phase modulation (with the bulk Mach-Zehnder interferometer) and it includes following elements:

A 1.15 μm HeNe laser as the optical source;

A 0.63 μm HeNe laser for optical alignment, of which output

beam was pre-aligned to the 1.15 μm one by two adjustable mirrors (1 & 2);

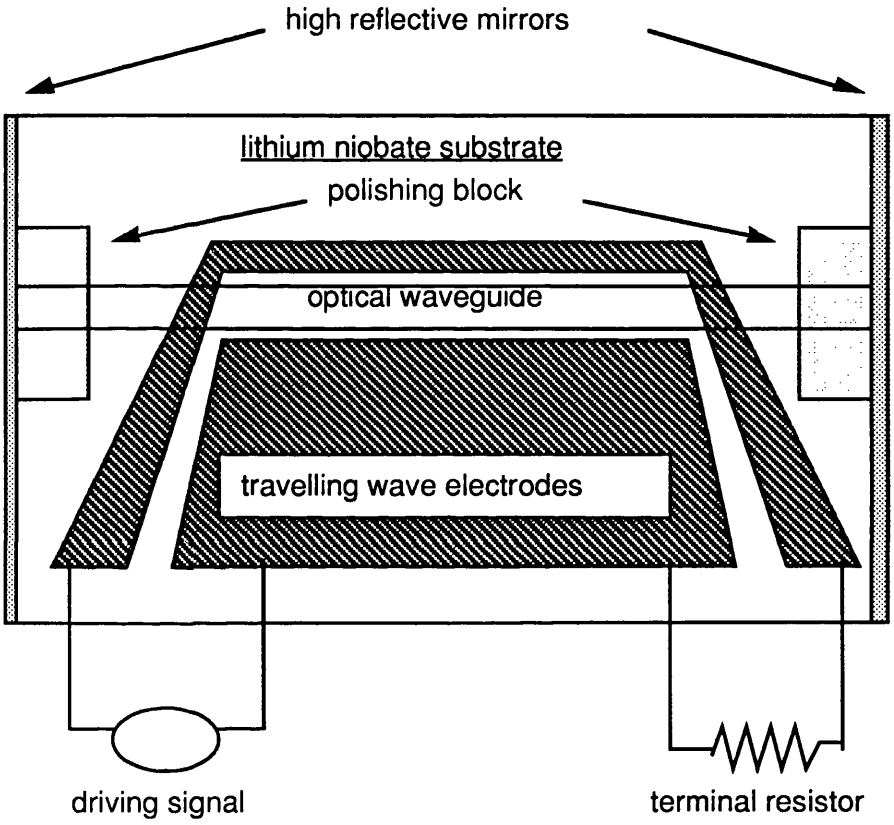

Fig. 8.1 The diagram of integrated optical Fabry-Perot modulator

A beam splitter (1) to divide the optical source for the Mach-Zehnder interferometer which was formed by another two adjustable mirrors to reflect the reference beam back and introduced the alignment beam (0.63 μm).

A X10 input microscope objective mounted on a micropositioner with three dimension of freedom to launch

the optical source in the optical waveguide;

The sample holder mounted on a stage with X-Y transverse translation and a horizontal rotation;

A X10 output microscope objective mounted on another three-dimension micropositioner to image the output;

Another beam splitter to join the reference beam to interference and to divide the output light into two parts for monitoring;

A infra-red TV camera to monitor the output image;

A photo-detecting circuit to decode the modulation and transfer to the display;

The microwave driving circuit is illustrated in Fig. 8.3. The microwave source is a 5 MHz to 1 GHz signal generator with maximum output power of 15 dBm; The output power was measured across the whole frequency before and after the experiments and the stability was found good. The 3-dB attenuator was applied to to reduced the reflection from the electrodes. A DC bias Tee was introduced to apply DC voltage to the modulator and cut-off the voltage to the generator, with the rolling-up frequency less than 1MHz. We used the lumped-electrodes structure for simplicity at the frequency up to at least 1GHz, while the electrodes was treated as a capacitor, because the travelling-wave electrodes would create electrical losses heating up the modulator which will cause excess phase shift to destablised the modulation performance, also the travelling-wave electrodes made the measurement much complicated. The DC blocking circuit was a option for it to be modulated at a high frequency.

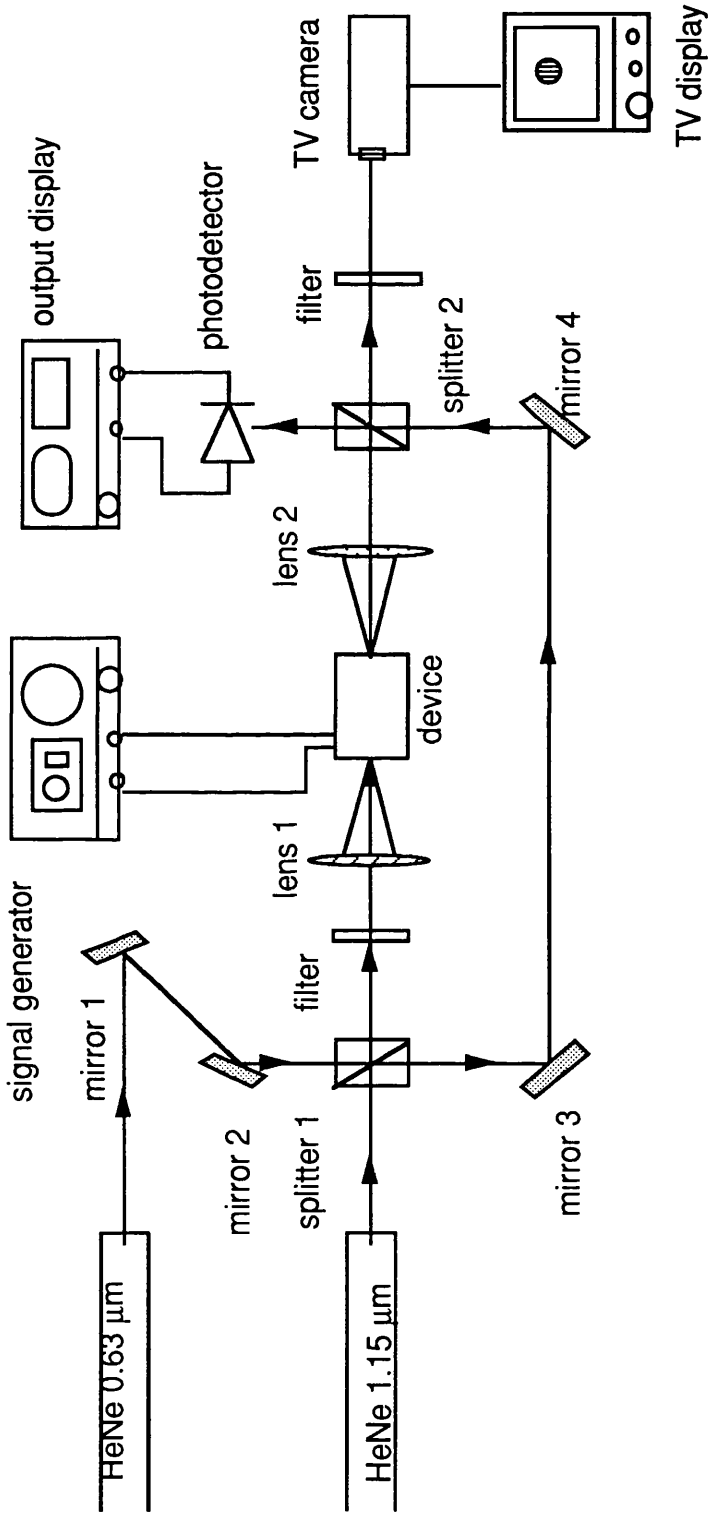

Fig. 8.2 The digram of optical experiment set-up

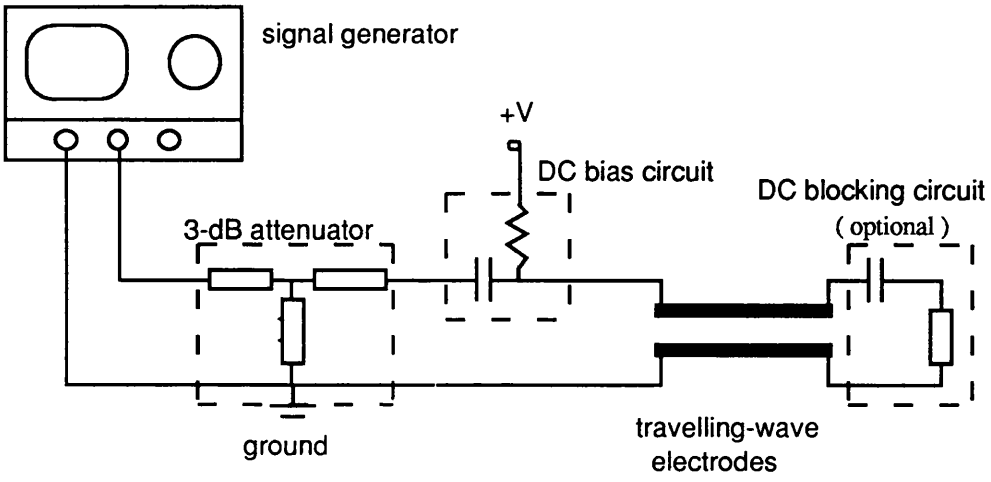

Fig. 8.3 The diagram of microwave driving circuit for Fabr-Perot modulator

The photo-detecting circuit with a 3-dB bandwidth of 1.3 GHz was designed, fabricated and will be discussed in detail in the next section. A spectrum analyser was used to test the frequency response, and a blocking capacitor was put before the rf input terminal to stop any DC off-set which could damage the instrument.

8.5 High Speed Photo-Detecting Circuit

A high speed photo-detecting measurement is the easiest method for directly testing high frequency modulation. When the modulator is driven by a CW microwave signal biased in its linear region, the output of the detector is another CW electrical at the same frequency and whose amplitude is proportional to the excursion of the intensity modulation. Therefore, the normalised frequency response of an intensity modulator (or a phase modulator placed in an interferometer) can be obtained by measuring the ratio of the detecting output amplitude over the excitation amplitude by sweeping the frequency across the range of

interest.

Unfortunately, high speed photo-detecting circuits are not commonly available on market or very expensive. This has led some researcher to find other methods for measuring the frequency response at high speed, such as sweeping frequency method [5] and scanning Fabry-Perot method [6].

In this section, we designed and fabricated a high-speed photo detecting circuit with commercially available elements which only cost less than £200. The photo-detector is a InGaAs Pin diode (SD3/5-075) from SDC Silicon Detector Corp. with good photo responsivity from 800 nm to 1600 nm, and its response time is about 200 ps (equivelant bandwidth of 1700 MHz) for a sensitive area of 0.0044 mm^2 and junction capacitance of 0.9 pf at a reverse voltage of 5 volt. The output from a photodiode is normally very small to be detected by a microwave instrument, so it was amplified by a trans-impedance amplifier which is specially designed for the photodiode and it was supposed to amplify the current signal into 50 Ω matched microwave power. The trans-impedance amplifier was selected as Avantek ITA-06318, which is a low noise, high-performance silicon bipolar Monolithic-Microwave-Integrated Circuit (MMIC) trans-impedance amplifier. It has quite large bandwidth of 1.3 GHz, high trans-impedance gain of 69 dB (for a trans-impedance of 2.8 KΩ), very low nosie of 3.5 pA/√Hz, and is very easy to operate.

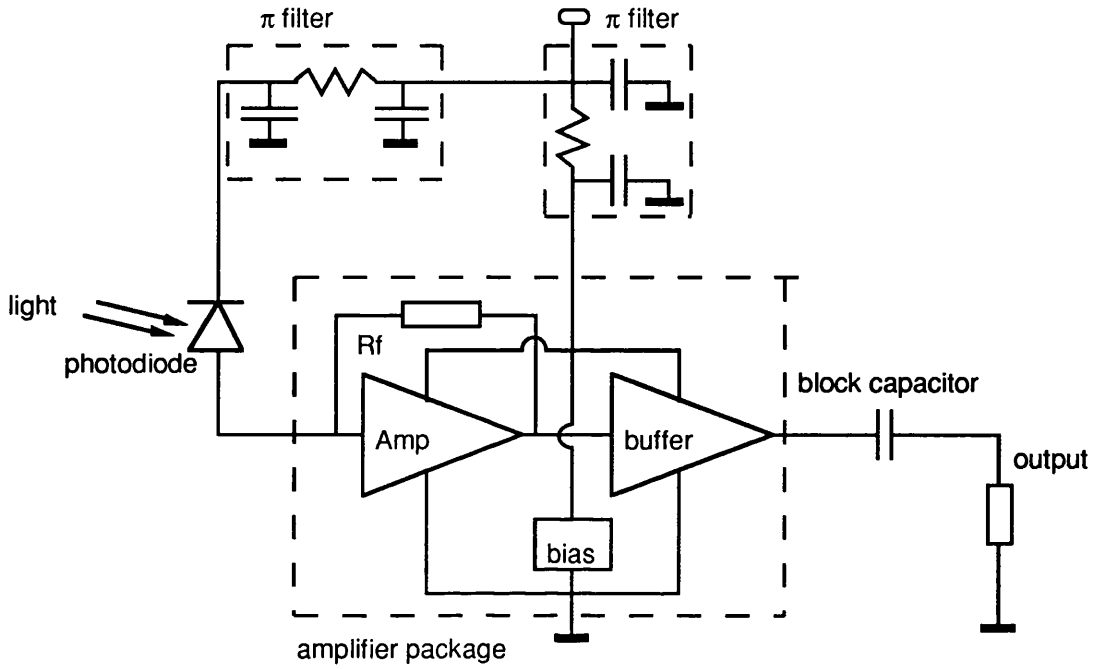

Fig. 8.4 The diagram of high-speed photo-detecting circuit

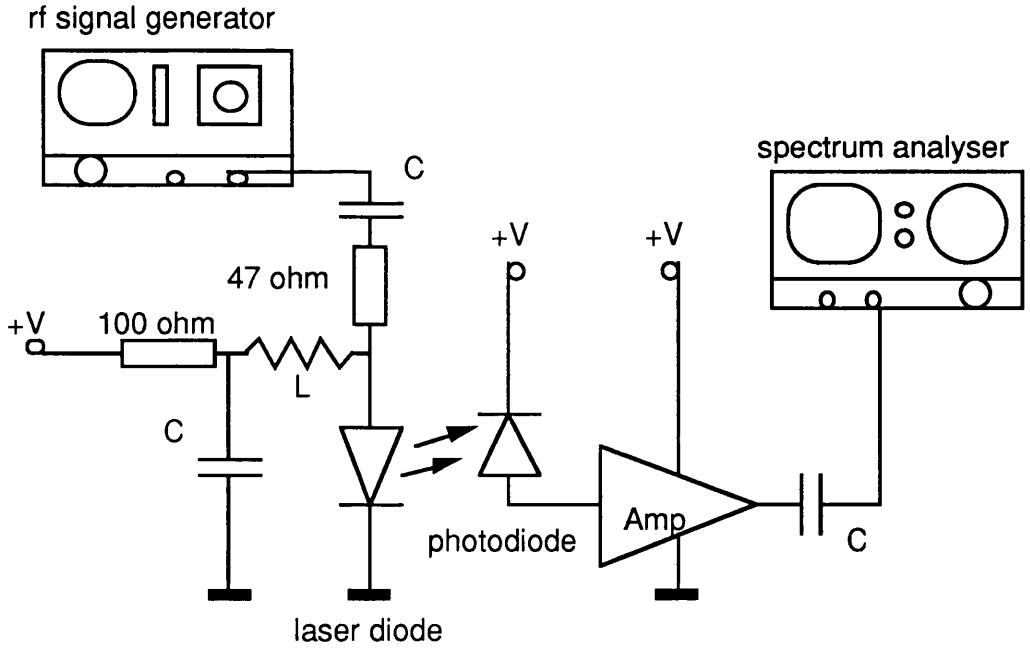

Fig. 8.5 The diagram of the photodetecting circuit testing set-up

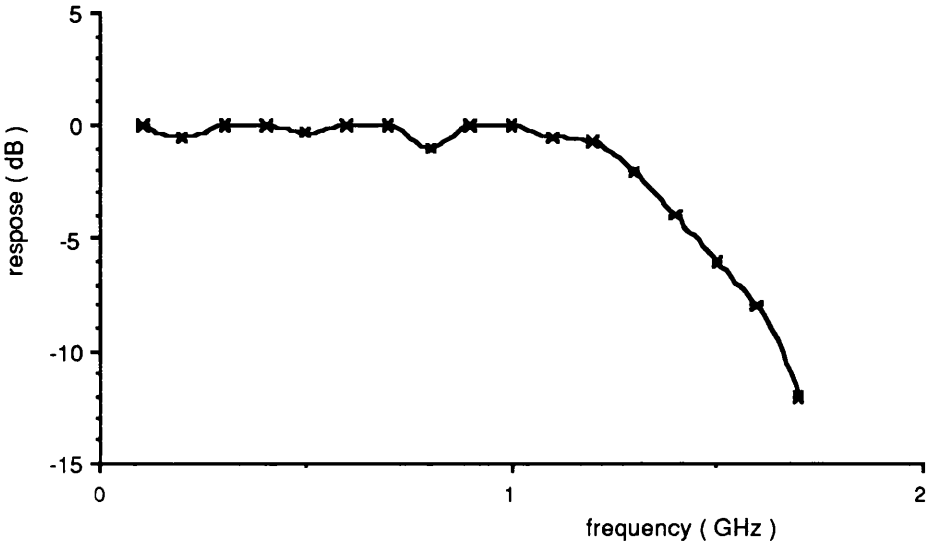

Fig. 8.6 The frequency respose of the photodetecting circuit

The whole photo-detecting circuit is illustrated in Fig. 8.4. A +5.5 volt DC power was supplied both for the bias of the photodiode and the amplifier. The anode of the photodiode was directly connected to the input terminal of the amplifier while the cathode was biased by π filter which stopped the interference from outside and cut-off the detected signal to escape to the output of the amplifier causing oscillation. The other π filter was applied to the DC supply of the amplifier functioning the same. The whole circuit was mounted on a double-sided alumina/E10^2 substrate on which the 50 transmission lines were etched by a width to height ratio of 0.95. A block capacitor was placed at the output terminal to stop any DC off-set. The ground side of the amplifier was stuck to the bottom of the die-case by electrically conductive paint (from RS) to obtain the best grounding.

The performance of the photo-detecting circuit was tested by a sweep generator, spectrum analyser system. The optical source was a direct modulated laser diode and the measurement diagram was shown in Fig. 8.5. The circuit was tested successfully with 3- dB bandwidth of 1.5 GHz and the noise output level was less than -30 dBm at the condition without optical input. The frequency response of the circuit was shown in Fig. 8.6.

8.6 Optical Losses Measured in Low-Finesse Waveguide Resonator

The optical losses play a crucial role in the waveguide Fabry-Perot cavity as we discussed early. A accurate method was proposed by R. Regener and W. Sohler using a low-finesse optical waveguide resonator[6]. The basic principle is based on Fabry-Perot interference of which output was tuned by temperature variation using the thermally controlled set-up described in chapter 6. The transmitted optical intensity I_t of a symmetric mono-mode Fabry-Perot waveguide resonator is given by the standard formula;

$$I_t = \frac{T^2 \exp(-\alpha L)}{(1 - R_{eff})^2 + 4R_{eff}\sin^2(\frac{\phi}{2})} I_0 \eta \qquad 8-1$$

where I_0 is the laser beam intensity in front of the waveguide, η the coupling coefficient to the (fundamental) waveguide mode, T the end-face mode transmission coefficient, and $\phi=2\beta L$ the internal phase shift of the cavity with the propagation constant β of the guiding mode in the etalon length of L. The effective reflectance R_{eff} = Rexp(-αL) is determined by analysing the waveguide resonance as discussed below. R

is the mirror reflectance of the cavity and α the attenuation coefficient of the optical waveguide.

As described in chapter 5 and 6, the transmitted intensity varies periodically with the cavity phase shift which can be tuned by temperature variation or applied electric field. The attenuation coefficient can be evaluated by measuring the absolute values of the maximum and minimum transmission.

$$K = \frac{I_{max} - I_{min}}{I_{max} + I_{min}} \qquad 8-2$$

where K is independent of I_0 and η, and it is only a function of R_{eff} along, i,e.;

$$R_{eff} = \frac{1}{K} \left(1 - \sqrt{1 - K^2} \right) \qquad 8-3$$

For the simplicity, we measured the waveguide losses without high reflective coatings on the resonator. The end-face reflectivity is caused by the Fresnal reflection of the waveguide material which can be approximated as the substrate one for a weakly guiding structures, such as Ti: $LiNbO_3$ waveguides. Therefore, the optical losses of the waceguide can be expressed as;

$$\text{Optical Losses (dB)} = 4.34[\ln(1-\sqrt{1-K^2}) - \ln K - \ln R] \qquad 8-4$$

Fig. 8.7 plotted the optical losses of waveguides versus the K values based on above equation, and the optical loss coefficients of the

waveguides (optical losses divided by the length of the waveguides) can be obtained by the measured K values with the accuracy of 0.01 dB/cm [6].

The single-pass loss of the experimental device was tested thermally by the set-up described in chapter 6 before the coating was put on. The K value of 0.21 was obtained from the ratio of maximum and minimum output corresponding to the temperature variation. The single-pass loss of 1.47 dB was calculated from the K value, which include the optical loss of the waveguide, the electrode-loading loss and the mode-mismatching loss of the wedge angle.

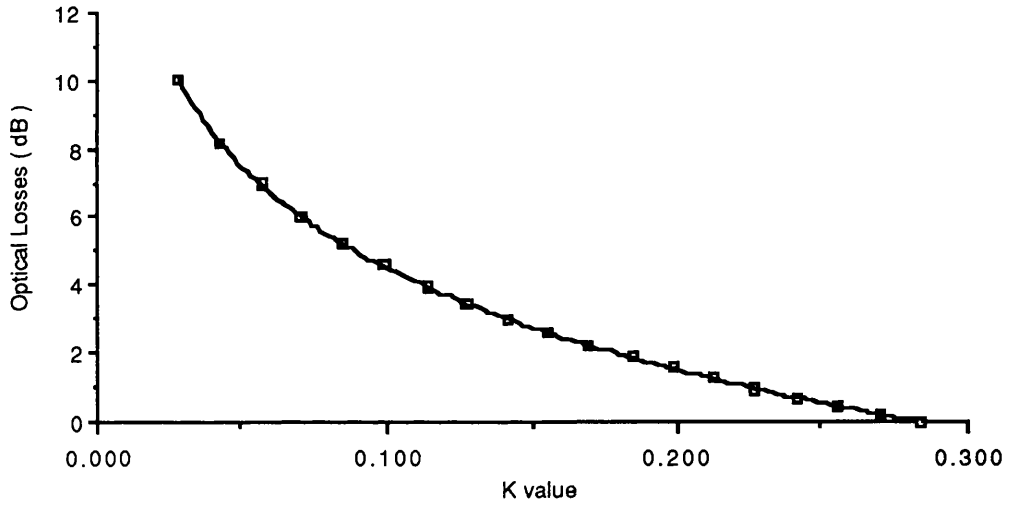

Fig 8.7 Optical waveguide attenuation versus the contrast K value

8.7 The Experimental Results of The Modulator

In this section, the experimental results are presented. The integrated optical Fabry-Perot modulator was fabricated as described previously, which is 1.5 cm long with the reflecting mirrors of around

80% (the effective reflectance is only about 50% because the optical losses of the waveguide resonator is nearly 1.5 dB); the interaction length of the electrodes is 1.0 cm long with a width of 8 μm and a gap of 8 μm as well. The experimental device was packed in a compact mount with a SMA connecting the driving cable and the whole package of the device is shown in Fig. 8.8.

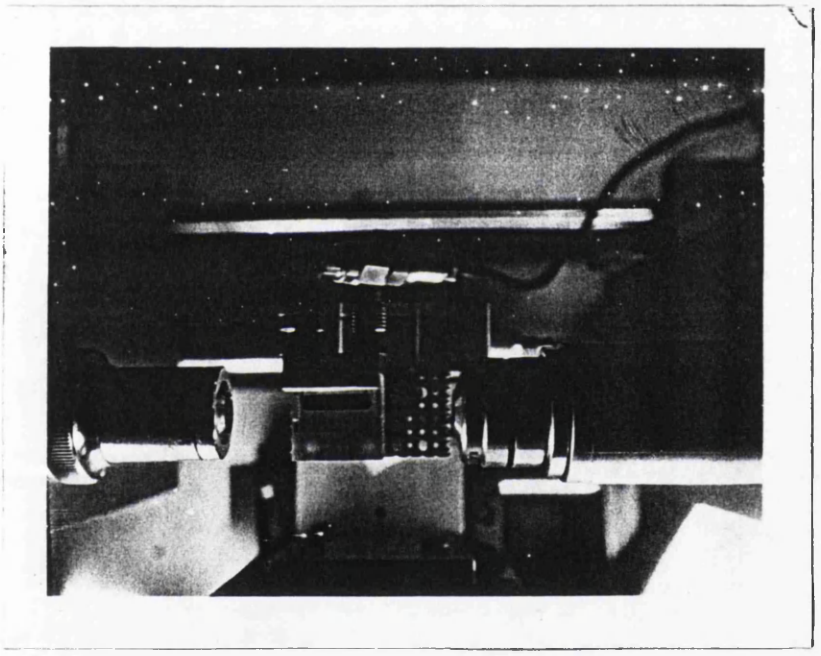

Fig. 8.8 The experimental device and set-up

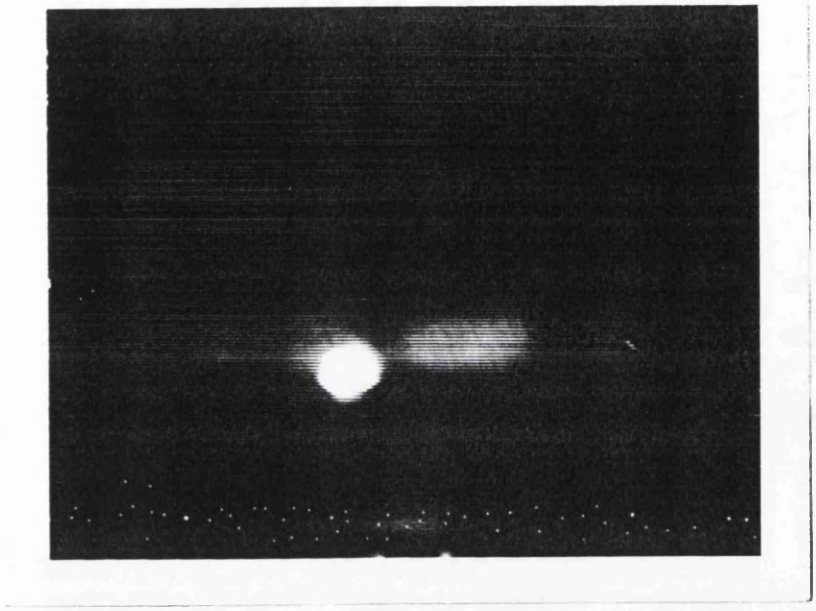

Fig. 8.9 The single-moded output profile of the optical resonator

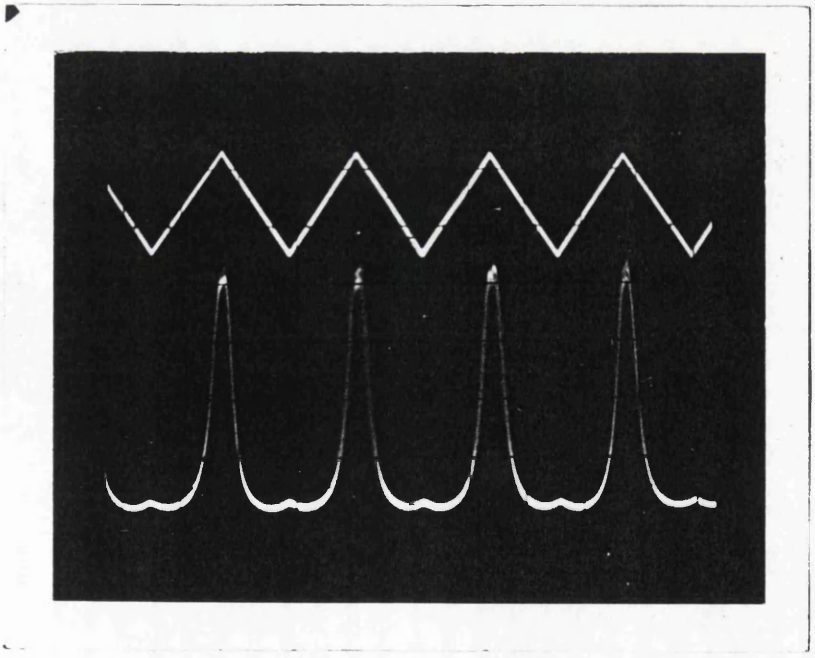

Fig. 8. 10 The Airy function output of the Fabry-Perot modulator driven by a ramp signal (above)

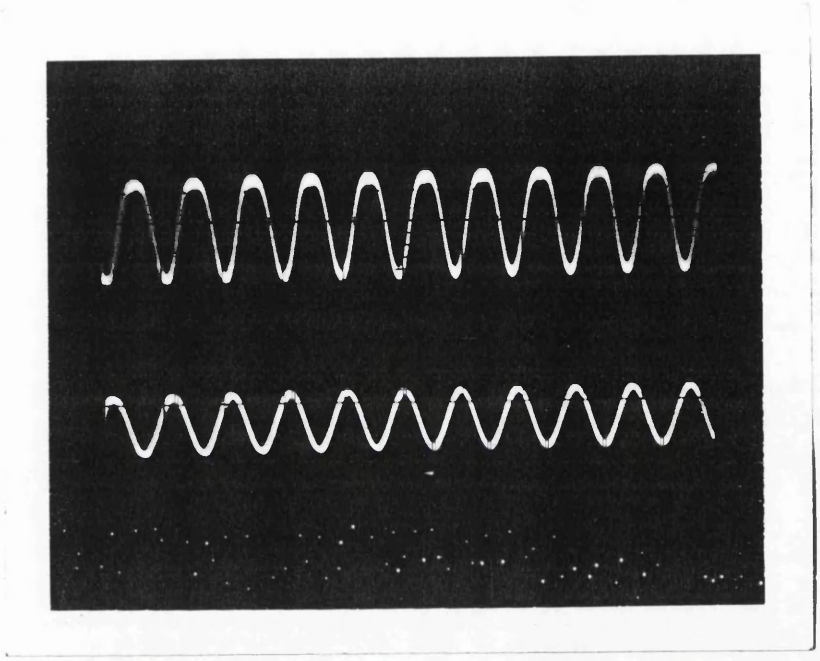

Fig. 8.11 The output of the Fabry-Perot modulation (above) driven by a sine signal (below) at a low frequency by a proper biasing

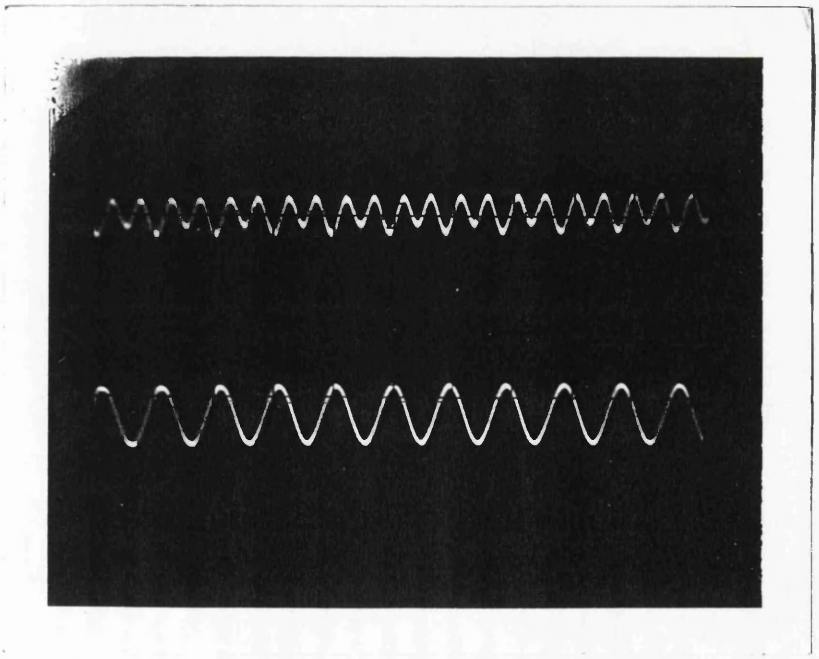

Fig. 8 12 The double frequency output (above) of the Fabry-Perot modulation biasing at the top point of the Airy function

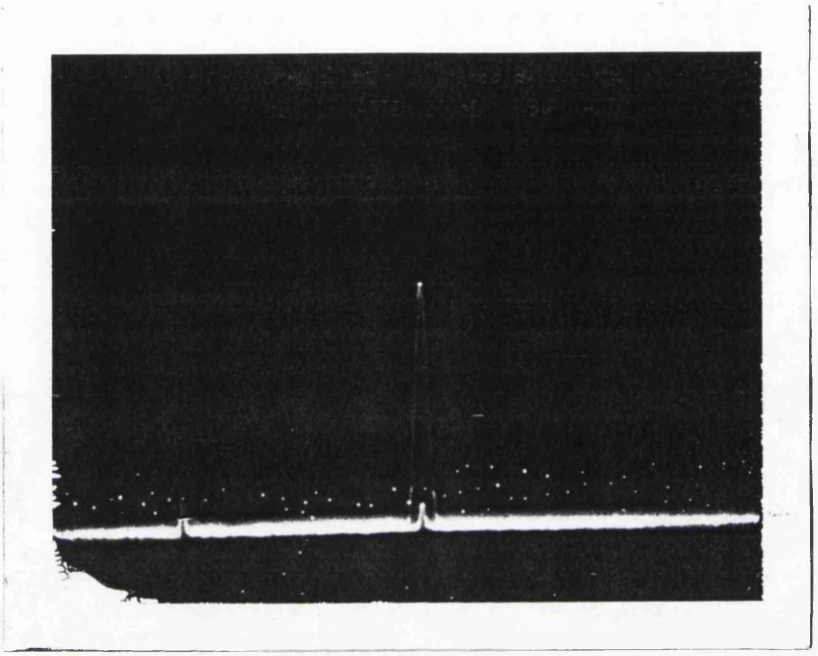

Fig. 8.13 The profiles of a single frequency modulation output and the electrical pick-up on a spectrum analyser

The above package was put on the experimental set-up shown in Fig. 8.2 and driven by the rf feeding circuit shown in Fig 8.3, which have been discussed in section 8.4.

Firstly, the laser beam of 1.15 μm was launched into the waveguide with the assistance of the visible laser beam of 0.63 μm, and a optimal single-mode output was obtained by the TV camera monitoring, of which the single-mode profile is shown in Fig. 8.9.

Secondly, the DC characteristics of the Fabry-Perot modulator were investigated by detecting the optical output variation by a low-speed, DC sensitive photodiode circuit connecting to a oscilloscope using the beam

divided by a beam splitter, while the output profile was monitoring by a TV camera using the another beam. A typical Airy function of a Fabry-Perot output was achieved by a ramp signal, which is shown in Fig. 8.10. Therefore, we worked out the half-wave voltage of the Fabry-Perot modulator is about 5.5 V and the voltage for a 84% modulation is only around 1.5 V. Although the reflecting mirror deposited on the waveguide resonator is about 80%, the profile of the output Airy function indicated that the effective reflectance is only about 50%. This is due to the optical losses of the waveguide resonator which is work out roughly 1.5 dB similar to that measured by the K value and the total insertion of the device less than 10 dB was realised. When it was modulated by a sine-wave signal at a low frequency, a sin-alike-wave output of the same frequency was observed if it was biased at a proper point which is shown in Fig. 8.11; while a sine-alike wave output of the double frequency was obtained if the bias point is at the top of the Airy function, which is shown in Fig. 8.12.

Finally, the high frequency modulation was measured by connecting the device to the microwave network which has been discussed in section 8.4. The high speed modulation characteristics was measured by a high speed photo-detecting circuit and displayed by a microwave spectrum analyser, and it was tested point by point from 50 MHz to 1000 MHz on a 50 MHz interval, and the DC bias was optimalised for each testing frequency due to the shift of the output envelope at different frequencies. A microwave driving power of 12 dBm was obtained by a microwave generator and about 9 dBm reached the modulator because a 3-dB attenuator was introduced to reduce the reflection from the electrodes to the microwave source. A output display of a single frequency on the spectrum analyser is shown in Fig. 8.13 and the electrical pick up was measured at least 30 dB less than the output signal tested by blocking the optical output, which is the small spur inside the output envelope in Fig. 8.13. The second harmonic was observed even at

the optimal bias point which is 20 dB less than the fundamental output and it varied with DC bias shift; while it disappeared when the optical output was blocked. It also been noticed that the output was quite sensitive to the environmental temperature change and the stability of the optical table. The modulation property (output vs the modulation frequency) is plotted in Fig. 8.14, which indicated that the 3-dB modulation bandwidth is at least 1GHz; while due to the limitation of the equipment, we only tested up to 1GHz.

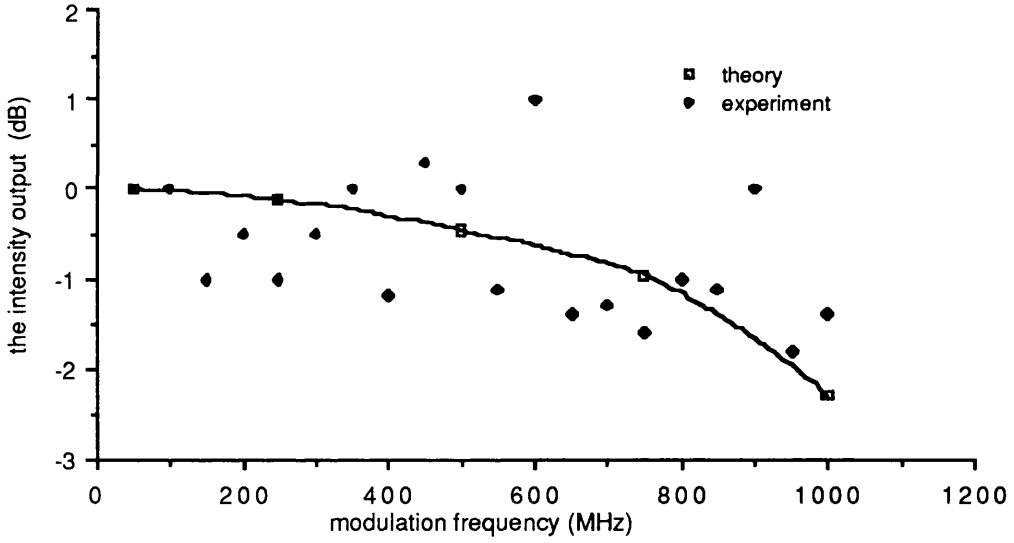

Fig. 8.14 The frequency response of the integrate optical Fabry-Perot modulator

8.8 Conclusion

In this chapter, the experimental results were presented and discussed. The whole consideration of the device fabrication was taken into account according the previous discussion at the different chapters; the fabrication was optimalised and traded off by the requirement of the

modulation characteristics; the experimental set-up was established for the multi-function measurements; a high-speed response photo-detecting circuit was designed and tested for the high frequency mesurement; a microwave network was introduced to measure the high-speed Fabry-Perot modulation; finally, the high-speed integrated optical Fabry-Perot modulator was tested both at low frequency and at high frequency, and a modulation bandwidth of at least 1 GHz was achieved.

8.9 Reference

[1] E. L. Gordon and J. D. Rigden, " The Fabry-Perot electrooptic modulator ", The Bell System Technical Journal, pp 155 - 179, Jan. 1963.

[2] W. J. Stewart, I. Bennion and M. J. Goodwin, " Resonant modulation ", Proc. of the 10th Europe conf. optical commun., Stuttgart, Germany, pp 37 - 41, 1984.

[3] A. Bruland and W. sohler, " Reflection mode integrated optical Fabry-Perot modulator ", Proc. of the 4th Europe Conf. on Integrated Optics, (SETG, Glasgow) pp 44 - 47, 1987.

[4] H. Herrmann, F. Kappe, R. Rickon and W. Sohler, " Dynamic properties of reflection mododе integrated optical Fabry-Perot modulators",

[5] S. Uehara, "Calibration of optical modulator frequency response with application to signal level control ", Applied Optics, Vol. 17, N0. 1, pp 68 - 71, Jan. 1978.

[6] R. Regener and W. Sohler, " Loss in low-finesse Ti: $LiNbO_3$ optical waveguide resonators ", Applied Phys. B. Vol. 36, pp 143-147, 1985.

[7] D. Bonaccini and R. N. Smartt, " Lithium niobate double channel Fabry-Perot interferometer for Solar conona uses ", Applied Optics, Vol. 27, No. 24, pp 5095 - 5102, Dec. 1988.

[8] P. Urquhart, " Transversely coupled fibre Fabry-Perot resonator: Theory ", Applied Optics, Vol. 26, No. 3, pp 455 - 463, Feb. 1987.

CHAPTER 9 CONCLUSION

In this thesis, we have discussed and concerned with the conception, analysis and fabrication of an integrated optical Fabry-Perot modulator. Our work has been concentrated with the waveguide fabrication on lithium niobate, travelling-wave electrode design and deposition, the highly reflecting mirrors of dielectric coating, the DC characteristics of a waveguide resonator, the temperature influence on the Fabry-Perot cavity and its application, the theoretical analysis of high frequency Fabry-Perot modulation, the experimental results of high frequency integrated optical Fabry-Perot modulator.

(a) The basic principle of the waveguide diffusion in lithium niobate was discussed; the waveguide characteristics like the dependence of index change on titanium concentration and operating wavelength, optical waveguide losses, effect of the crystal stoichiometry, light-induced refractive index change (optical damage), outdiffusion and its depression were concerned; the influence of fabricating parameters such as diffusion temperature, diffusion time, diffusion atmosphere (the rate of flowing dry or wet oxygen), width and thickness of the titanium strips were investigated; different waveguides was fabricated at different conditions and a modified diffusion set-up was established for the low optical losses, out-diffusion waveguide for Y-cut lithium niobate at the wavelength of 1.15 μm, which is crucial to the Fabry-Perot modulator.

(b) Different electrode structures have discussed and investigated; a co-planar asymmetric travelling-wave

electrodes were selected for high frequency integrated optical modulators; the impedance of the electrodes was calculated by Schwarz-Christoffl transformation; the velocity mismatch between the optical and microwave signals in the crystal which decided the modulation bandwidth was analysed; electrical conducting losses was taken into account; a new depositing method was presented which is called " Etched-Lift-Off " for a deeply diffused optical waveguide modulator.

(c) The highly reflective multi-layer dielectric coating was concerned theoretically; the reflecting properties were investigated for different structures on different substrates; the principles of monitoring were analysed and a new monitoring system was set up with the available equipment in the department; the designed coatings of 3-, 5-, 7-, 9-layers consisted of Zinc Sulphide and Cryolite were fabricated, and tested by a monochrometer for the high reflecting zone.

(d) The DC characteristics of the integrated optical Fabry-Perot modulator was investigated: the maximum and minimum available optical output, maximum available modulation index as well as half-wave phase shift were calculated; the influence on the performance by the mirrors reflectivity and the optical losses of the waveguide were analysed; the effect of the wedge angles causing by the mode mismatching due to the mirror reflection was taken into account for the waveguide resonator; a polishing jig was carefully designed to achieve the minimum wedge angle.

(e) The temperature sensitivity of waveguide resonator play a crucial part in Fabry-Perot modulation as it shifts the DC bias point: the refractive index variation and waveguide length

shift causing by a temperature change were discussed and summarised; the half wave temperatures (temperature change for π phase shift) were calculated for both TM and TE modes at the wavelengths of 1.15 μm and 0.63 μm, and was measured by both by intensity variation (reflecting mode method) and phase shift monitoring (bulk Mech-Zehnder interferometer); the possibility to be used as a temperature sensor was also concerned.

(f) The modulation bandwidth of a Fabry-Perot modulator was calculated and both velocity mismatch between the electrical & optical signals and multiple modulation were taken into account: the modulation cut-off frequency limited by the forward and backward transmission beams was analysed, while the influence of the length of the electrodes and cavity was concerned as well; the bandwidth limited by multiple modulation was simulated by computer and a bandwidth of 1GHz for the first order and 2GHz for higher order were achieved for a waveguide Fabry-Perot modulator of 1.5 cm long with 50% reflecting mirrors.

(g) The experimental device was fabricated using the technique and procedure discussed previously: first, the device was considered using the optimal elements; the experimental set-up was established for multiple function measurements; a rf testing network was presented for high frequency modulation; a high speed response photo-detecting circuit of a 3-dB bandwidth of 1.5 GHz was designed and tested for monitoring the modulation bandwidth; the total optical losses of the waveguide for the resonator was measured by the Low-Finesse waveguide resonating method for only 1.47 dB.

Finally, an integrated optical Fabry-Perot modulator was obtained by depositing the 80% reflecting mirror at the ends of experimental device of 1.5 cm long. The effective reflectance is only about 50% by both calculation and measurement. A half wave voltage of 5.5 V was achieved by monitoring both the intensity variation by a photo-diode circuit and the phase shift by a bulk Mech-Zehnder interferometer. The modulation bandwidth was tested by the microwave network and a 3-dB bandwidth of at least 1 GHz was obtained.

Future Work:

Following these results, a short term development of this work would be to make a integrated optical Fabry-Perot modulator working at very high frequency with a reasonable narrow bandwidth which is decided by the integral number of the resonating frequency of the Fabry-Perot cavity. The merit of the modulation will depend on the electrodes structures which can make the very high frequency modulation available such as the phase-reversal electrodes, or other velocity matching technologies. The microwave driving power is mainly the function of the reflecting mirrors of the cavity affected by the optical losses in the waveguide. Therefore, the microwave driving power can be reduced to a very low level by trading of the modulation bandwidth and also the total optical insertion losses can be kept relatively low if the optical waveguide losses is extremely small which is reduced to around 0.01 dB/cm at present.

This modulator can be used in a fibre optical system if the device is pigtailed with optical fibres which has been investigated and demonstrated already. Microwave connection to the modulator was realised using curved and tapered trans-impedance line and a K connector linking the electrodes to the driving source can work up to 40

GHz.

From above discussion, very high speed modulation can be available for a integrated optical Fabry-Perot modulator. It may have many application for high speed optical modulation and optical signal processing in the area of limited working space and very small driving power